# Mirror Dark Matter Cosmology and Structure Formation

**Jean-Samuel Roux**

Supervised by James M. Cline

Department of Physics

McGill University, Montreal

April 2020

A thesis submitted to McGill University in partial fulfillment

of the requirements of the degree of Masters of Science

# Contents

# List of Tables

# List of Figures

# Acknowledgements

This thesis would not have come to fruition without the unfailing support of many people close to me. Special thanks to my supervisor, Jim Cline, for his invaluable insight and his assistance toward the completion of this project. I also thank my friend and colleague M. Puel for the many enlightening discussions we had. I look forward to working with them both again.

Je remercie également mes amis et ma famille qui continuent de me soutenir et de m'encourager inconditionnellement. Enfin, merci à ma compagne de vie, Alice, qui est toujours là pour moi et à qui je dédie ce mémoire.

This work has been funded in part by the Fonds de recherche du Québec – Nature et technologies (FRQNT).

# Contribution of the author

This integrity of thesis was written by the author, Jean-Samuel Roux (J.-S. R.).

Chapters 3 to 5 contain a rewritten and expanded version of the material that was covered in reference [19], a paper that J.-S. R. wrote in collaboration with his supervisor, J. Cline. Most of the ideas explored in that publication came from the present author and every result was obtained by him.

Every figure in this document was created by the author, unless explicitly stated. The calculations were all made by him, including modifications to the open-source programs presented in refs. [130, 131], [134–140] and [150] which were respectively used to numerically study primordial nucleosynthesis (section 3.3) and recombination (section 3.4) in the mirror sector as well as the impact of mirror particles on the matter power spectrum (section 4.1).

Where the author has consulted or quoted the work of others, the source is always given. With the exception of such quotations, this thesis entirely reflects the own work of the author.

# Abstract

Mirror matter is a dark matter candidate that consists of an exact copy of the Standard Model gauge group. Assuming the $Z_2$ mirror symmetry between ordinary and mirror matter is unbroken, the chemical and nuclear processes of each sector have the same rates, which makes the model fully predictive given the temperature and density of mirror matter. In this thesis, we study the cosmology of mirror matter, focusing on structure formation, in order to constrain the parameters of this theory. We first give a review of the evidence for dark matter and the tensions within the cold dark matter paradigm. We then go over the main events of standard cosmology in both the visible and mirror sectors in order to highlight their differences. Next, we present a semi-analytical model of galaxy formation that allows us to simulate the formation of mirror structures. After presenting the results of our analysis, we constrain the model using astronomical observations.

# Résumé

La matière miroir, candidate à la matière sombre, consiste en une copie exacte du groupe de jauge du modèle standard. Si la symétrie miroir $Z_2$ entre la matière ordinaire et la matière miroir est préservée, les taux de réactions chimiques et nucléaires seront les mêmes dans les deux secteurs, rendant ce modèle parfaitement prédictif à une température et une densité de matière miroir données. Dans ce mémoire, nous étudions la cosmologie de la matière miroir, mettant l'accent sur la formation des structures, afin de circonscrire les paramètres de cette théorie. D'abord, nous rappelons les preuves de l'existence de la matière sombre et les problèmes entourant le paradigme de la matière sombre froide. Puis, nous passons en revue les principaux événements de la cosmologie standard, tant pour la matière visible que pour la matière miroir, afin de souligner leurs différences. Nous présentons ensuite un modèle semi-analytique de formation des galaxies, lequel nous permet de simuler la formation des structures miroir. Après avoir présenté les résultats de notre étude, nous les comparons à des observations astronomiques afin de borner les paramètres de ce modèle.

# Chapter 1

# Introduction

This decade will mark the 100th anniversary of "dark matter" [1], a term first coined by Jacobus Kapteyn in 1922 as he studied the structure and the internal motion of the Milky Way (MW) [2]. In his modestly called "first attempt," he suggested that one could use stellar dynamics to infer the abundance of non-luminous matter in the galaxy. The same year, James Jeans found that according to Kapteyn's galactic model of ellipsoid shells, there should be 2 or 3 "dark stars" for every bright star in the MW [3]. Thus the idea that most of the matter in our galaxy is dark already seemed plausible. Although Kapteyn's understanding of our galaxy was incorrect, his work paved the way for a century's worth of research in astrophysics, cosmology and particle physics that aims to understand the origin of matter in the universe.

The first observational evidence for dark matter (DM) came about a decade later, as Fritz Zwicky realized that the stability of the Coma galaxy cluster required more mass than what visible stars could account for [4]. But DM did not receive much attention before the 1970s. At the time of Zwicky's observations, the mass-to-light ratio of galaxies and galaxy clusters could only be extrapolated from much smaller systems, leading to significant uncertainties in the mass estimates of objects as large as the Andromeda Galaxy (M31) or the Coma Cluster. Furthermore, astronomers did not know how luminosity absorption in the interstellar medium and viscous interactions between stars impacted their results, an issue Zwicky addressed himself in 1937 [5]. Because of this, discrepancies between optical and dynamical measurements of galactic masses were often swept under the rug.

It was only with the development of radioastronomy and spectroscopy around the mid-century that the idea of "missing matter" became inescapable. Vera Rubin and her collaborators realized that rotation curves of spiral galaxies were flatter than expected, indicating the presence of a large amount of DM that extended much further than the visible disks [6–9]. A similar observation had been made 30 years earlier by Horace Babcock [10].

From this point on, the pieces of evidence for DM began to multiply, not only because of the ever-increasing collection of astronomical data, but also due to theoretical progress in cosmology. In particular, Jim Peebles soon pointed out that the growth of cosmological perturbations after matter-radiation decoupling was insufficient to form large-scale structures like galaxy clusters [11]. Not only must there be roughly five times more matter than what we observe inside stars, but this additional component cannot interact with light like ordinary matter does. This picture differs drastically from the beliefs of Peebles' predecessors: DM is not made of "cool and cold stars, macroscopic and microscopic solid bodies, and gases," as Zwicky put it [5]; it is instead *fundamentally different* from baryonic matter.

Cold dark matter (CDM) has since then become the leading paradigm in cosmology and astrophysics. Both fields have met with huge success by treating DM as weakly interacting massive particles (WIMPs). But even today, it is unclear how these particles fit into the bigger picture of the Standard Model (SM) and a possible "theory of everything." Moreover, CDM simulations on small scales have been discrepant with observations over the last decades [12, 13]. This encouraged theorists to consider other DM models.

A popular alternative to CDM is the idea that DM might form a "hidden" (or "dark") sector, that is, a collection of particles that interact via new mediators and that are weakly coupled to the SM. Hidden sectors are generally viewed as a possible solution to the small-scale problems of CDM because of their self-interactions [14, 15].

Among the vast number of dark sector proposals, mirror matter stands out because its convoluted network of chemical and nuclear reactions does not come at the cost of having too many parameters and losing predictive power. This model assumes that DM (or a fraction of it) is part of a gauge group identical to the SM and forms a “mirror sector” (MƧ). If the two sectors are decoupled, their evolutions can differ significantly depending on their respective initial conditions: whereas ordinary matter condenses into galaxies and develops life forms, it need not be the case for mirror matter.

Cosmological observations like the cosmic microwave background (CMB) or the matter power spectrum put strong constraints on mirror matter and similar DM models [16–18]. However, these limits can generally be evaded if the MƧ temperature is sufficiently low. The goal of this thesis is to constrain the parameters of mirror matter — namely its abundance and its temperature — by instead comparing astronomical data with the MW mirror matter distribution predicted by our structure formation simulation. As we will show, for a significant region of the parameter space mirror matter would lead to the formation of dark galactic structures analogous to the MW disk and bulge. The presence of these dark structures would impact stellar dynamics on various levels, which allows us to set bounds on the MƧ parameters. Unlike most models of strongly self-interacting DM that assume a single dark galactic component, mirror matter provides a self-consistent way of populating different components and constraining them, which is why we chose this approach. The results of our study have been released in ref. [19], but this thesis significantly expands upon the material covered in that paper.

In chapter 2, we will review the evidence for DM, describe the small-scale problems of CDM and introduce a few well-known DM candidates. We will present the mirror matter model and describe how its cosmological evolution parallels that of ordinary matter in chapter 3. In particular, we will establish the abundance of light nuclei and the ionization fraction of the MƧ at the onset of structure formation, which will set the initial conditions for the galaxy formation simulation. In chapter 4, we will introduce the theoretical concepts of structure formation and the methodology of our simulation, including a discussion on the self-consistency of our assumptions regarding the matter power spectrum and the merger history of the MW halo. We will present the results of our analysis and the constraints derived from them in chapter 5 before concluding in chapter 6.

Throughout this thesis we will use the following cosmological parameters [20]: $h = 0.678$, $T_0 = 2.7255$ K, $\Omega_m = 0.308$, $\Omega_b = 0.0484$, $\Omega_\Lambda = 0.692$, $n_s = 0.968$ and $\sigma_8 = 0.815$. Although most of these values were obtained assuming a $\Lambda$CDM cosmology, our conclusions would not change significantly if we used slightly different parameters.

# Chapter 2

# Dark matter

## 2.1 Evidence for dark matter

### 2.1.1 Astronomical observations

The discovery of dark matter is often credited to Zwicky who estimated the mass of the Coma Cluster using the virial theorem in 1933 [4] and refined his calculations in 1937 [5]. The virial theorem relates the average kinetic energy $K$ and potential energy $U$ of a stable system:

$$2\left\langle K\right\rangle_t = -\left\langle U\right\rangle_t\,, \tag{2.1}$$

where $\langle x\rangle_t$ is the average value of $x$ over time.

The average kinetic energy in the Coma Cluster can be written as

$$\left\langle K\right\rangle_t = \frac{1}{2}\sum_i M_i\left\langle v_i^2\right\rangle_t = \frac{1}{2}\mathcal{M}\left\langle v^2\right\rangle_{t,M}\,, \tag{2.2}$$

where $M_i$ and $v_i^2$ are the mass and velocity dispersion of each galaxy, $\mathcal{M}$ is the total mass of the cluster and $\langle x\rangle_{t,M}$ indicates a double average over time and galaxy mass. The potential energy of a self-gravitating system is

$$\langle U \rangle_t = -C\frac{G\mathcal{M}^2}{R}, \tag{2.3}$$

where $G = 6.67 \times 10^{-11}$ m$^3$ kg$^{-1}$ s$^{-2}$ is Newton's gravitational constant, $R$ is the radius of the system and $C$ is a constant that depends on the matter distribution (for a homogeneous sphere $C = 3/5$). To obtain a conservative bound on $\mathcal{M}$, Zwicky took the following limit:

$$2\langle K \rangle_t = -\langle U \rangle_t < 5\frac{G\mathcal{M}^2}{R} \Rightarrow \mathcal{M} > \frac{R\langle v^2 \rangle_{t,M}}{5G}. \tag{2.4}$$

He estimated the radius of the cluster at $R \approx 615$ kpc and the velocity dispersion at $\langle v^2 \rangle_{t,M} \approx (1225\ \text{km/s})^2$, yielding a lower bound $\mathcal{M} \gtrsim 4.5 \times 10^{13}\ M_\odot$. Observing about a thousand galaxies in the Coma cluster, Zwicky found that their average mass therefore had to satisfy $\langle M \rangle \gtrsim 4.5 \times 10^{10}\ M_\odot$. Assuming an average luminosity of $\langle L \rangle = 8.7 \times 10^7\ L_\odot$ per galaxy, he obtained a surprisingly high lower bound for their mass-to-light ratio[1]:

$$\frac{\langle M \rangle}{\langle L \rangle} \gtrsim 500\ \frac{M_\odot}{L_\odot}. \tag{2.5}$$

One generally expects $M/L \sim 1$–$30\ M_\odot/L_\odot$ in main-sequence stars [21]. The result 2.5 therefore implies that the Coma Cluster contains much more matter than what visible stars can account for.

The next big piece of evidence for DM came from rotation curves of spiral galaxies obtained by Rubin and her collaborators [6–9]. Assuming stars have a circular orbit, their tangential velocity at a given distance $r$ from the galactic nuclei is

$$v(r) = \sqrt{\frac{GM_r}{r}}. \tag{2.6}$$

[1]To determine the velocity dispersion, Zwicky seemingly used Hubble's estimation of $H_0$, which is one order of magnitude higher than the currently accepted value. Even if we rescale the mass-to-light ratio with the right value of $H_0$ we find that it still points to the existence of DM [1].

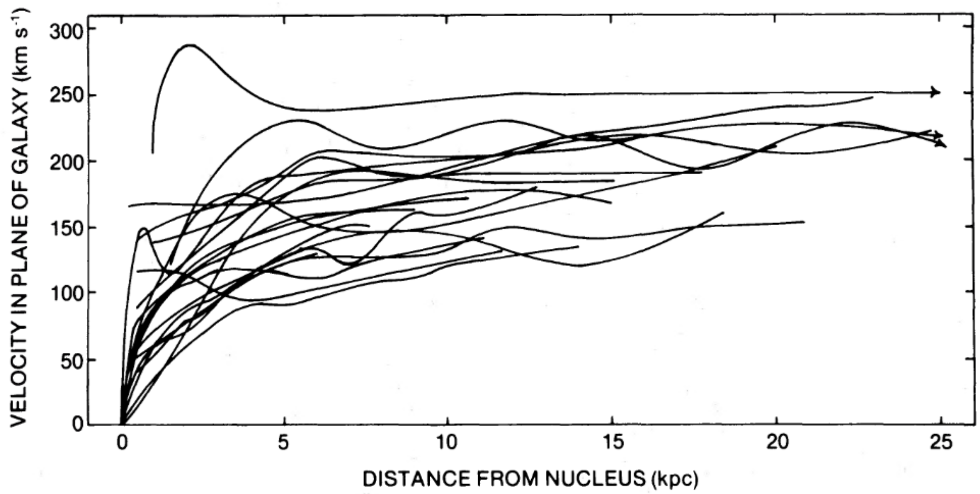


Figure 2.1: Examples of galactic rotation curves. Figure taken from [9].

Here $M_r$ is the total mass inside a sphere of radius $r$.

Far beyond the edge of the galactic disk ($r \gg R_{\text{disk}}$), one would expect $M_r \approx$ const. and $v \propto r^{-1/2}$. However, rotation curves like the ones illustrated in fig. 2.1 indicate that $v \approx$ const. at large radius. This signals the presence of an extra matter component that extends further than the visible disk and possesses a density profile $\rho(r) \propto r^{-2}$ (assuming a spherically symmetric distribution). Moreover, this extra component dominates over the stellar mass of the galaxy, thus reinforcing Zwicky's claim that galaxies have a mass-to-light ratio much higher than ordinary stars.

Gravitational lensing provides another way of measuring the mass of a galaxy cluster. General relativity predicts that massive objects curve spacetime and the path of photons in their vicinity. This phenomenon was experimentally confirmed over a century ago by Dyson, Eddington and Davidson who observed the deflection of starlight by the Sun during a total solar eclipse [22]. Zwicky suggested that this effect could also apply to much larger objects, like galaxy clusters [5]. In this case gravity is so strong that the foreground cluster acts as a lens and distorts the image of background galaxies into an Einstein ring or arclet. The half-angle made by this ring on the celestial sphere is given by [23]

$$\theta_E = \sqrt{\frac{4GM}{c^2}\frac{D_{sl}}{D_s D_l}}, \tag{2.7}$$

where $M$ is the mass of the lens, and $D_l$, $D_s$ and $D_{sl}$ are the distances to the lens, to the source and between the lens and the source respectively. By virtue of eq. (2.7), one can estimate the total mass of the lens by measuring its Einstein angle $\theta_E$. For instance, gravitational lensing by the galaxy clusters Abell 370 and CL 2244–02 indicates that their mass-to-light ratio is roughly $10^2$–$10^3$ $M_\odot/L_\odot$, yet another hint at a dominant DM abundance [24].

More recently, the discovery of the Bullet Cluster not only confirmed the existence of DM, it also put limits on its scattering cross section [25–28]. The Bullet Cluster consists of two colliding galaxy clusters. During the encounter, galaxies passed through each other almost unimpeded, but the hot intergalactic gas of baryons slowed down significantly due viscous interactions. The latter represents the largest fraction of *baryonic* mass in the clusters, but gravitational lensing showed that most of the *total* mass followed the collisionless trajectory of galaxies.

Figure 2.2 shows the X-rays produced by the shock-heated baryons and the matter distribution inferred from gravitational lensing. The gas clearly lags behind the bulk of the clusters. Therefore DM is dominant and its cross section is limited to

$$\frac{\sigma}{m} \lesssim 1\ \text{cm}^2\ \text{g}^{-1} = 1.76\ \text{barn GeV}^{-1}. \tag{2.8}$$

While fairly large, this bound is lower than the typical cross section for nucleon-nucleon scattering, $\sigma/m \sim 20$ barn GeV$^{-1}$ [29]. Thus DM cannot have arbitrarily strong self-interactions and it must be weakly coupled to baryons (if at all), which hints at its non-baryonic nature. But decades before the discovery of the Bullet Cluster, cosmological evidence already suggested that DM could not simply be made of non-luminous ordinary matter.

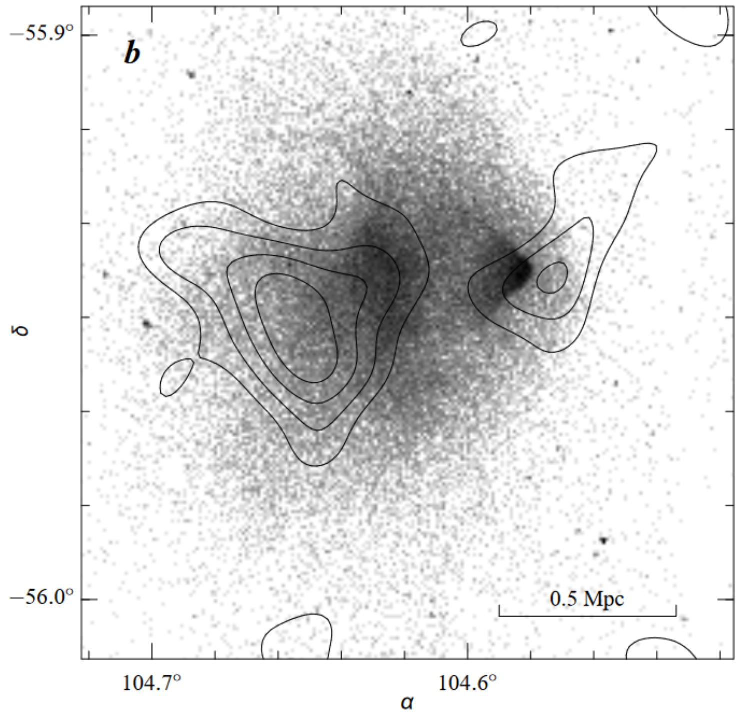


Figure 2.2: Overlay of the lensing mass contours (solid curves) on the X-ray image of the Bullet Cluster. The offset between the X-ray source (hot baryons) and the gravitational lens (DM and galaxies) is obvious. Figure taken from [25].

### 2.1.2 Cosmological evidence

Pioneers like Peebles [30], Silk and Wilson [31] realized in the 1980s that baryons alone could not form the largest structures we observe today. We will briefly outline the issue here and we will review the theory of structure formation in more detail in chapter 4. Galaxies formed from primeval density fluctuations $\delta = \delta\rho_m/\overline{\rho_m}$ that grew with the expanding universe until they gravitationally collapsed. Data from the CMB suggests that primordial baryonic perturbations were of order $\sim 10^{-5}$ [32–34], but gravitational collapse occurs when $\delta \sim 1$ [35].

Prior to recombination, baryons were strongly coupled to photons and the radiative pressure prevented baryon overdensities from growing. Therefore, in a universe without DM, primordial fluctuations could only increase by a factor $\sim (1+z_{\rm rec}) \sim 10^3$ which is insufficient for structure formation. Peebles suggested that if matter was dominated by a pressureless component (*i.e.*, that does not couple to radiation, a *dark* component), matter perturbations

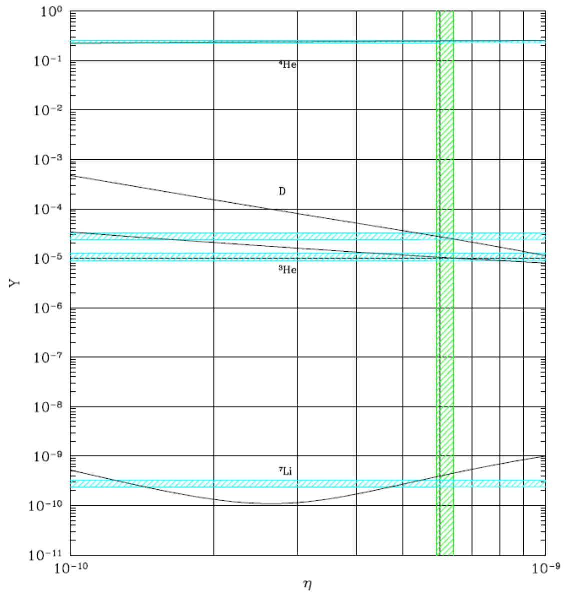


Figure 2.3: Relic mass fraction $Y_i = \rho_i/\rho_{\text{tot}}$ of light elements (from top to bottom, $^4$He, D, $^3$He and $^7$Li) after BBN as a function of $\eta_b$. Horizontal cyan bars indicate the observed abundance (with uncertainties) and the vertical green bar is the best-fit value of $\eta_b$. Figure taken from [40].

could grow as early as matter-radiation equality. In this scenario baryon overdensities would grow by a factor $\sim (1 + z_{\text{eq}})/\Omega_b \sim 10^5$ [36], allowing for structure formation.

The abundances of light nuclei after Big Bang nucleosynthesis (BBN) are another probe of the DM density. Numerical analyses have shown that the outcome of BBN is highly sensitive to the baryon-to-photon ratio, $\eta_b = n_b/n_\gamma$, and hence to the baryon abundance [37,38]. More specifically, as we will show in section 3.3, $\eta_b$ determines the temperature at which nuclear species like deuterium (D) form in thermodynamic equilibrium. Deuterium is of particular interest because of its binding energy: it is so low that it does not form efficiently in stars; it burns immediately [36, 39]. Therefore the deuterium we observe today must have formed during BBN, its relic density is not affected by stellar nucleosynthesis like helium or lithium.

Fig. 2.3 illustrates the dependence of the nuclear abundances on $\eta_b$. The relic densities agree with a baryon-to-photon ratio of roughly $\eta_b \approx 6.1 \times 10^{-10}$ [20]. Rewriting $n_b = \overline{m_N}\Omega_b\rho_{\text{crit},0}$, where $\overline{m_N} \approx 1.1$ GeV is the mean mass per nucleus, and using $\rho_{\text{crit},0} \approx 4.8 \times 10^{-6}$ GeV cm$^{-3}$ and $n_\gamma \approx 410$ cm$^3$ as suggested by the CMB [20, 41], we find $\Omega_b \approx 0.05$,

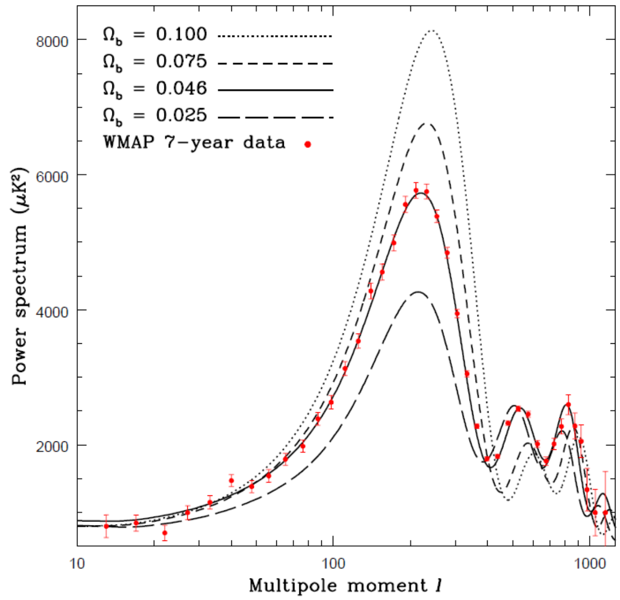


Figure 2.4: CMB anisotropy spectrum with varying baryon abundance (fixing $\Omega_m = 0.3$) and comparison with data from WMAP. Figure taken from [40].

roughly one sixth of the total matter density $\Omega_{\mathrm{m}} \approx 0.3$. This observation was another strong evidence that DM is non-baryonic, *i.e.*, it is not made of cold gas and faint stars as it was originally thought.

Detailed analysis of the CMB power spectrum also supports the existence of DM. On small scales, temperature anisotropies arise from baryon acoustic oscillations (BAO) in the photon-baryon fluid: baryons tend to condense in gravity wells, which in turn increases the radiative pressure and makes the fluid expand. DM is not subject to these oscillations; it attracts baryons inside the gravity wells and therefore limits the amplitude of the BAO [34, 40, 42–44]. This effect is illustrated in fig. 2.4: an increase in $\Omega_b$ changes the amplitude of the CMB anisotropies and shifts the position of the peaks. Data from the Wilkinson Microwave Anisotropy Probe (WMAP) [45] and more recently from the Planck collaboration [41] both indicate $\Omega_b \approx 0.05$ and strengthen the case for non-baryonic DM.

Finally, the matter power spectrum $\mathcal{P}(k)$ (which we will introduce formally in chapter 4) also favors the existence of DM. $\mathcal{P}(k)$ is proportional to the matter distribution on a comoving scale $\lambda \sim k^{-1}$. Without DM, the power spectrum would be highly suppressed

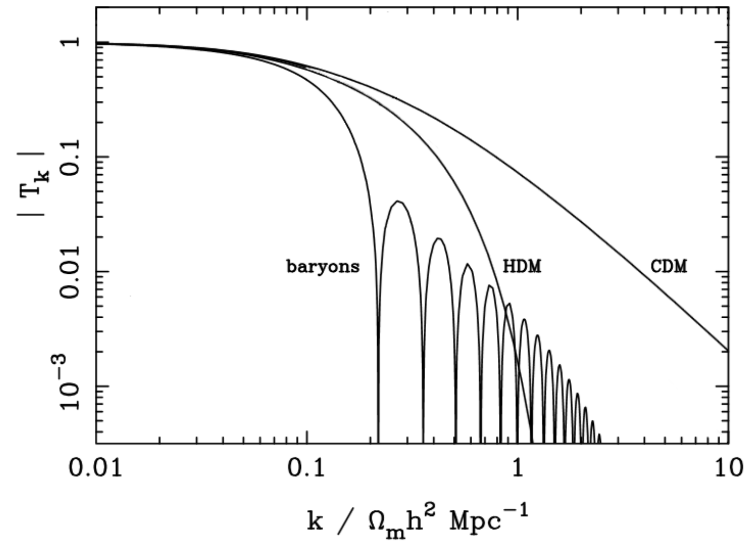


Figure 2.5: Transfer function $T_k \propto \mathcal{P}(k)^{1/2}$ in a universe dominated by cold dark matter (CDM), hot dark matter (HDM) and baryons. Figure adapted from [49].

by Silk damping at large $k$ (*cf.* section 4.2) and would oscillate due to the BAO described above [40, 46–48]. This is illustrated in fig. 2.5 where we plotted the transfer function $T_k$, which is proportional to square root of the matter power spectrum.

The power spectrum is also sensitive to the nature of DM. "Hot" dark matter (HDM) consists of particles that were relativistic when they decoupled from the thermal bath, like neutrinos. Like baryons, HDM would lead to a suppressed power spectrum at large $k$ due to free-streaming, an effect similar to Silk damping. In short, the high velocities of hot particles would allow them to escape small-scale overdensities, effectively washing them out [50]. By contrast, "cold" dark matter (CDM) particles were nonrelativistic when they decoupled from radiation. Other variations exist, like "warm" dark matter (WDM; see section 2.3.1). Fig. 2.5 also illustrates the transfer function in HDM and CDM models. Comparison of N-body simulations and galactic surveys like the Sloan Digital Sky Survey (SDSS) [51] and the 2-degree Field Galaxy Redshift Survey [52] rule out HDM scenarios in favor of CDM. This suggests that galaxies formed following a "bottom-up" hierarchy where small matter halos merged into large structure. In contrast, HDM would imply a "top-down" evolution in which massive halos fragmented into smaller objects. The distribution of galaxies in this scenario would be very different from what we observe [36, 53].

These are the main observations that led to the current ΛCDM paradigm in cosmology: non-baryonic dark matter exists[2] and makes up about 85 % of the matter budget of the universe. It is also cold and it interacts weakly, both with itself and with ordinary matter.

## 2.2 Problems of cold dark matter

No particles of the SM fit the description of DM, but many models beyond it like supersymmetry (SUSY) or string theory naturally provide a suitable candidate, usually in the form of weakly interacting massive particles (WIMPs).[3] Expectations were high after the realization that WIMPs at the weak scale would naturally yield the right relic density and could soon be detected in laboratory, a finding often referred to as the "WIMP miracle." However, in the last decades, collider experiments and high-resolution N-body simulations encouraged consideration of alternatives to the WIMP hypothesis. We will review these developments below.

### 2.2.1 Missing "WIMP miracle"

In SUSY models, a popular DM candidate is the lightest stable superpartner, like the neutralino or gravitino. Models of extra dimensions also include Kaluza-Klein particles, which are momentum excitations along the extra spatial dimensions. These are both examples of WIMPs as they are expected to interact weakly and have a mass in the range 10–1000 GeV [56–59].

[2] A competing theory, although much less popular than DM, is that all observations described in section 2.1.1 (with the exception of the Bullet Cluster) come from our erroneous assumption of Newtonian gravity. Models of MOdified Newtonian Dynamics (MOND) or its relativistic equivalent of Tensor-Vector-Scalar gravity (TeVeS) are generally successful in explaining galactic dynamics, but they don't address the cosmological evidence of section 2.1.2. They also seem inconsistent with galactic surveys [54] and the recent detection of gravitational waves [55].

[3] Because ΛCDM analyses often consider WIMPs as the default DM candidate, we will use "WIMPs" and "CDM" interchangeably for the remainder of this thesis. Obviously, any consistent candidate must be cold (or warm); "CDM" will only refer to the simplest model possible.

We can easily estimate the relic density of CDM particles if we assume a standard thermal freeze-out scenario [36, 60]. Suppose that DM particle-antiparticle pairs can annihilate into SM particles via a $2 \to 2$ scattering process, $\chi\overline{\chi} \to f\overline{f}$. The rate of this reaction can be expressed as $\Gamma = n_\chi \langle \sigma v \rangle$, where $\langle \sigma v \rangle$ is the thermally averaged cross section. These annihilations will freeze out once $\Gamma \simeq H \sim T^2/m_{\rm pl}$, where $m_{\rm pl} = 1.22 \times 10^{19}$ GeV is the Planck mass (related to Newton's constant $G = m_{\rm pl}^{-2}$). The number density of DM particles at the freeze-out is therefore

$$n_\chi \sim (m_\chi T_f)^{3/2}\, e^{-m_\chi/T_f} \;\sim \frac{T_f^2}{m_{\rm pl}\,\langle \sigma v \rangle}, \tag{2.9}$$

where the first expression is the Maxwell-Boltzmann distribution and $T_f$ is the freeze-out temperature.

It is useful to define the dimensionless quantity $x_f = m_\chi/T_f$. The last equality can then be rewritten as a transcendental equation for $x_f$:

$$x_f \sim \ln\left(m_{\rm pl}\, m_\chi \langle \sigma v \rangle\right) - \frac{1}{2}\ln x_f. \tag{2.10}$$

Solving this equation numerically for reasonable values of $m_\chi$ and $\langle \sigma v \rangle$ yields $x_f \approx 15$–$30$. Note that the dependence on the DM parameters is only logarithmic, so this result is valid for a broad region of the parameter space.

Let us define the comoving abundance $Y_\chi \equiv n_\chi/s$, where $s \propto T^3$ is the entropy density of the universe. This quantity remains constant once DM annihilations stop. In terms of $x_f$ this is approximately

$$Y_\chi \sim \frac{x_f}{m_\chi m_{\rm pl}\,\langle \sigma v \rangle}. \tag{2.11}$$

If $\chi$ particles make up all of DM, their current relic density must satisfy

$$\Omega_\chi = \frac{m_\chi n_{\chi,0}}{\rho_{{\rm crit},0}} = \frac{m_\chi Y_\chi s_0}{\rho_{{\rm crit},0}} \approx \frac{x_f s_0}{m_{\rm pl}\,\langle \sigma v \rangle\, \rho_{{\rm crit},0}} \approx 0.25. \tag{2.12}$$

Quantities with a '0' subscript are evaluated at the present time. Solving for the cross section, we find

$$\langle \sigma v \rangle \approx 4 \times 10^{-9} \ \ \mathrm{GeV}^{-2} \left( \frac{x_f}{20} \right), \tag{2.13}$$

where we used $s_0 = 2981 \ \mathrm{cm}^{-3}$. We see that $\langle \sigma v \rangle \sim 10^{-9} \ \ \mathrm{GeV}^{-2}$ is of the same order as a typical weak scale cross section, $\sigma \sim \alpha G_F$, where $\alpha = e^2/4\pi \approx 1/137$ is the fine structure constant and $G_F = 1.166 \times 10^{-5} \ \mathrm{GeV}^{-2}$ is the Fermi coupling constant.

This coincidence is often referred to as the "WIMP miracle" [61, 62] and led some to believe that the physics of DM would be revealed at the weak scale. This was good news, because the Large Hadron Collider (LHC) would precisely probe energy scales up to $\sim 10$ TeV, which should have been enough to produce DM or observe its loop corrections in the decay of SM particles. Cosmological WIMPs should also be detected, either directly by scattering off nuclei or indirectly by annihilating into observable particles. Unfortunately, no experiment has detected any of the expected WIMP signals,[4] and faith in the "miracle" started to fade.

### 2.2.2 Small-scale discrepancies

The non-detection of WIMPs does not rule out the CDM paradigm: their mass could simply be at a scale currently out of reach, or their cross section might be weaker than originally thought. But a series of discrepancies between CDM N-body simulations and galactic surveys strengthened the tensions within the model. We briefly present these issues below based on the reviews of refs. [12, 13].

**Cusp/core problem.** CDM-only N-body simulations of structure formation suggest that the density profile of small DM halos scales as $\rho \propto r^{-\gamma}$ in the central region, where $\gamma \sim 0.8$–$1.4$. This is steeper than what is observed in most dwarf galaxies, which suggest $\gamma \sim 0$–$0.5$ instead [70, 71]. This is illustrated in fig. 2.6: the measured circular velocity (eq. (2.6))

[4] Some direct-detection experiments like DAMA/NaI, DAMA/LIBRA or CoGeNT [63–65] claimed to have observed a periodic signal attributed to DM, but those detections are controversial as no other collaboration could confirm their results [66–69].

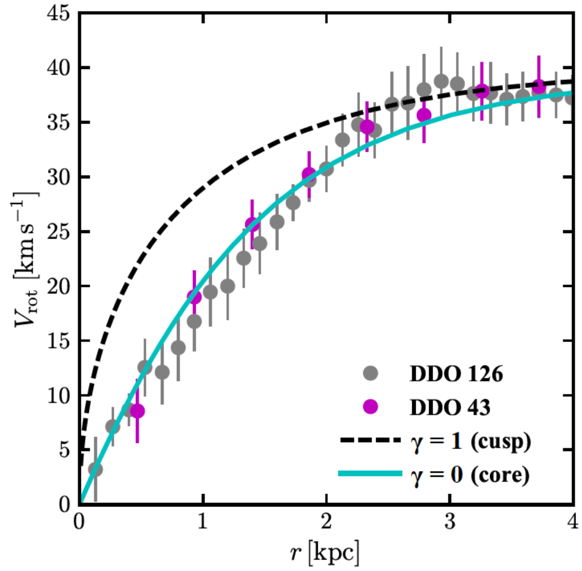


Figure 2.6: Rotation curves of a $10^{10}\ M_\odot$ DM halo with a cuspy ($\gamma \sim 1$, dashed) or a cored ($\gamma \sim 0$, solid) density profile. Data points show the rotation curves measured in two dwarf galaxies of similar mass. Figure adapted from [13].

rises much less abruptly than predicted by simulations, which hints at a cored profile rather than a "cuspy" one. Similarly, the central abundance of DM predicted by simulations is higher than what we observe. While these issues are different, they are likely to be solved simultaneously.

**Missing satellites.** Structure formation simulations further predicted a large number of subhalos orbiting the MW [72, 73]. Although their exact number depends on the resolution scale of the simulation, most studies agree that there should be $\sim 1000$ satellite subhalos with a mass $M_{\rm sub} \approx 10^7\ M_\odot$ or larger. This is much larger than the $\sim 50$ satellite galaxies we have discovered so far. But this 'missing satellites' puzzle is likely to be solved without changing the paradigm. This is because our galactic surveys are incomplete: only a fraction of the total area of the sky has been surveyed (about 1/3 in the case of the SDSS [74]) and ultra-faint dwarf galaxies (UFDG), which form inside halos of mass $M_{\rm sub} \lesssim 10^{10}\ M_\odot$, can only be detected within $\sim 100$ kpc of the Earth due to their faintness [13]. More importantly, star formation is inefficient in subhalos smaller than $M_{\rm sub} \lesssim 10^8$–$10^9\ M_\odot$: baryons can't reach a

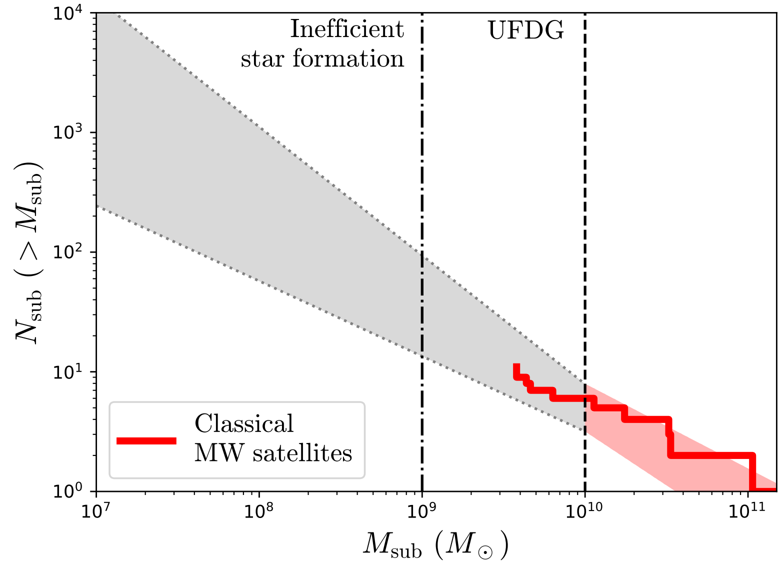


Figure 2.7: Possible solution to the missing satellites problem within the CDM paradigm. The red line shows the cumulative count of the MW classical satellites, which agrees with the range predicted by CDM simulations in the large-mass regime (red area). The grey-shaded region is the extrapolation of this expected range to the UFDG scale (left of the dashed line), where current surveys are incomplete. Halos left of the dot-dashed line are likely to be completely dark due to their inefficiency at forming stars. Figure adapted from [13].

virial temperature high enough to allow gas clouds to cool an collapse (*cf.* section 4.3) [75] and/or cloud collapse is impeded by background radiation after reionization [76]. Low-mass halos could be as abundant as predicted by simulations, but completely dark, making their detection challenging.

Fig. 2.7 illustrates the situation more quantitatively. The red curve shows the cumulative count of MW subhalos for the 11 'classical' (brightest) satellite galaxies. The red-shaded region shows the 68 % range predicted by CDM-only simulations for large halos, and the grey-shaded area is the same range extrapolated to the regime of UFDG [77]. The range widens because it depends on the shape of the faint-end stellar mass function $dn/dM_* \sim M_*^{-\alpha}$, which is not accurately measured (recent estimates indicate $1.32 < \alpha < 1.62$ [13, 78]). If we extrapolate this range all the way down to $10^7\ M_\odot$ subhalos, we see that the cumulative count is consistent with the $\sim 1000$ subhalos predicted by simulations, although most of them would be inefficient at forming stars and thus appear completely dark. This solution

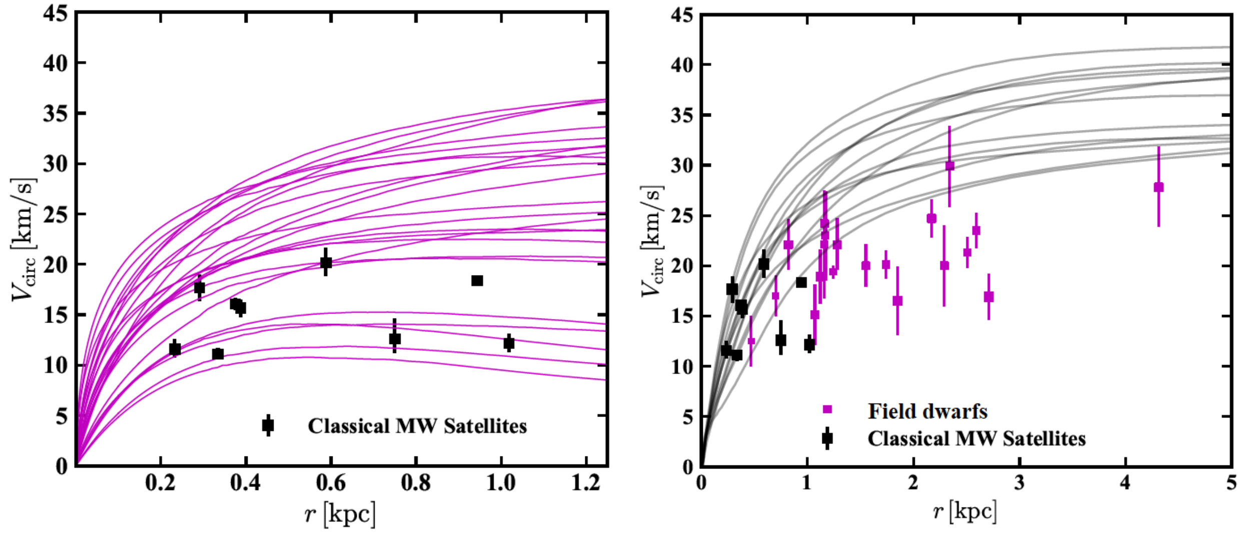


Figure 2.8: Comparison of central rotation curves of massive subhalos in CDM simulations (solid curves) and of dwarf galaxies (data points), for both MW satellites (left) and field dwarfs (right). Figure adapted from [13].

is for the moment purely speculative as these low-mass halos have not been discovered yet. It is also possible that the CDM hypothesis used in numerical studies is wrong.

**Too-big-to-fail subhalos.** The above solution to the missing satellites problem implicitly assigns the brightest MW satellites to the biggest subhalos in CDM simulations (*cf.* the red area in fig. 2.7). However this creates another issue, because the central density of these subhalos is higher than what we measured in our satellite galaxies. The left-hand side panel of fig. 2.8 shows the central rotation curves of the 24 biggest subhalos in a CDM simulation and the circular velocity in the 9 brightest MW satellites [79]. None of the data points are among the top $\sim 50\,\%$ velocities, which suggests that the central density of galaxies is systematically lower than predicted in simulations. Unlike the low-mass halos of the missing satellites problem, these large subhalos should be very efficient at forming stars; they are too big to have failed and cannot be completely dark.

A solution proposed early on was that interactions between the MW and its satellites (mainly through stellar feedback) stripped matter from the subhalos, an effect that could not be reproduced in CDM-only simulations [80, 81]. However, a similar issue was observed in 'field' dwarf galaxies, that is, isolated galaxies that are not satellites [82]. The right panel of fig. 2.8 illustrates the 'too-big-to-fail' problem in field dwarfs. The data points are also lower than predicted in CDM simulations, but in their case it cannot be explained by interactions with a host galaxy. Solutions to this issue would either have to explain why the most massive halos are counter-intuitively inefficient at forming stars or why their central densities are lower than predicted by CDM simulations.

**Modern small-scale problems.** The issues presented above are the three classic problems of the CDM paradigm and have been extensively studied ever since the first structure formation simulations, a little more than two decades ago [83, 84]. More recently, other discrepancies have surfaced which may eventually help constrain the nature of DM.

The MW satellites appear to lie in a plane, which is not a configuration commonly obtained in CDM simulations (although that claim is disputed) [85]. A similar planar distribution was observed in the satellites of M31, which suggests that this arrangement might not be a simple statistical fluctuation [86].

The Baryonic Tully-Fisher Relation (BTFR) is an empirical law that relates the baryonic mass $M_b$ of a DM halo to the circular velocity $V_f$ on the flat end of the rotation curves (*cf.* fig. 2.1): $M_b \propto V_f^4$ [87]. A reasonable explanation for this relation would be to assume some proportionality between the dynamical properties of galaxies and their host halos, specifically between their masses and circular velocities. However, the BTFR is extremely tight while the dynamics of galactic systems scatter significantly between halos with similar characteristics [88]. How a precise correlation such as the BTFR could arise from a disparate set such as the observed galaxies is poorly understood.

To various extents, the inclusion of baryons in numerical simulations has alleviated most of the aforementioned issues. The main baryonic effect is stellar feedback: dying stars produce supernovae that eject matter from the halo's center, leader to a shallower gravitational potential, a lower central density and a cored matter distribution. The shocks that result from a supernova and tidal interactions can also strip matter from satellite galaxies [80, 81]. However, star formation is inhibited in low-mass halos and dwarf galaxies in the field also suffer from the 'too-big-to-fail' problem. Therefore stellar feedback is not a valid solution on all mass scales. Elastic scattering of hot baryons can lead to a cored profile even in the absence of stars, but there is no consensus as to whether this effect is sufficient. Because of this, and since WIMPs remain undiscovered, alternatives to CDM have gained popularity in the last decades. We present a few examples below.

## 2.3 Alternatives to cold dark matter

### 2.3.1 Warm dark matter

Although structure formation rules out hot dark matter, warm dark matter (WDM) is still a possible scenario. In the standard picture, WDM decouples from radiation while it is relativistic but at a much earlier time than HDM, such that it is not heated during the QCD phase transition and is therefore colder than light neutrinos [50]. It also becomes nonrelativistic long before matter-radiation equality and thus shares many properties with CDM.

The leading candidate for WDM is a keV-scale sterile neutrino. Its main feature is its free-streaming which suppresses the matter power spectrum $\mathcal{P}(k)$: because WDM is collisionless, it easily escapes overdense regions, effectively washing out matter perturbations. The free-streaming length is simply the comoving distance travelled by the sterile neutrinos before matter-radiation equality, and is roughly given by [36, 89]

$$\lambda_{\rm fs} = \int_0^{t_{\rm eq}} \frac{v}{a(t)} dt \approx 0.1 \text{ Mpc } \left(\frac{\text{keV}}{m}\right), \tag{2.14}$$

up to a $\mathcal{O}(1)$ constant that depends on the production mechanism of WDM. This quantity can be misleading since scales above $\lambda_{\rm fs}$ are also significantly affected by free-streaming. The damping of the matter power spectrum is better described by the half-mode scale $\lambda_{\rm hm} \sim 10\lambda_{\rm fs}$ at which the transfer function is suppressed by 50 % relative to ΛCDM cosmology. The corresponding mass scale is

$$M_{\rm hm} = \frac{4\pi\rho_{m,0}}{3}\left(\frac{\lambda_{\rm hm}}{2}\right)^3 \approx 2\times 10^{10}\ M_\odot \left(\frac{\rm keV}{m}\right)^3. \tag{2.15}$$

One can easily see from the last expression that free-streaming by WDM only affects small halos and leaves the success of CDM on larger scales unchanged. The suppression of the matter power spectrum reduces the number of halos smaller than $M_{\rm hm}$ and delays their formation, which leads to a lower central density[5] [90]. WDM could therefore explain why satellite galaxies are missing and alleviate the too-big-to-fail problem, but simulations have shown that the density profiles are still too cuspy compared to observations. Furthermore, recent analyses of the Lyman-$\alpha$ forest constrain $m \gtrsim 5$ keV [91]. This limits the impact of free-streaming to halos smaller than $\sim 10^8\ M_\odot$, which is only a fraction of the mass range where CDM and observations are discrepant.

### 2.3.2 Axions

Axions are ultralight pseudoscalar particles that were initially proposed as a solution to the strong CP problem [92–94]. QCD admits the following CP-violating gauge interaction

$$\mathcal{L} \supset \frac{g_s^2\theta}{64\pi^2}\epsilon^{\mu\nu\rho\sigma}G^\alpha_{\mu\nu}G^\alpha_{\rho\sigma}, \tag{2.16}$$

where $g_s$ is the strong coupling constant, $\theta$ is an angle that parametrizes the QCD vacuum and $G^\alpha_{\mu\nu}$ is the field strength tensor. This term should give rise to a neutron electric dipole moment, which has not been observed yet. The current bound $d_n \lesssim 10^{-26}$ $e$ cm implies $\theta \lesssim 10^{-10}$ [95]. However, that angle could *a piori* take any value between 0 and $2\pi$, which

[5]The central density of a halo scales with the background matter density $\rho_m \propto a(t)^{-3}$ at the time of its formation.

indicates some degree of fine-tuning. To explain the minuscule value of $\theta$, a popular solution is to replace it with a dynamical field, $\theta \to a/f_a$ where $a$ is the axion and $f_a$ is its decay constant, that naturally settles to zero (usually due to a tilt in its potential). Solving the strong CP problem typically requires a $\mu$eV-scale axion.

Since the QCD axion was first proposed, it was discovered that similar ultralight pseudoscalars are ubiquitous in string theory and are theoretically well motivated DM candidates [96, 97]. In view of the CDM problems of section 2.2.2, axions have attracted some attention due to their naturally large de Broglie wavelength $\lambda_{dB} \approx 1/mv$, a consequence of their small mass and nonrelativistic velocity. Below this scale, axions form a Bose-Einstein condensate that would smear out matter overdensities, preventing structure formation. This model is often referred to as "fuzzy dark matter" [98].

We can understand the impact of axions on galaxy formation analytically using a standard Jeans analysis. Treating the axion condensate as a classical field, it should evolve as $\sim e^{\gamma t}$, where $\gamma^2 = 4\pi G\rho - (k^2/2m)^2$ [98]. On small scales (large $k$), $\gamma$ becomes imaginary and the field oscillates with constant amplitude; whereas on large scales (small $k$), it grows rapidly. The Jeans wavenumber $k_J$ separates these two regimes and corresponds to a wavelength

$$\lambda_J^2 \sim \frac{1}{k_J^2} \sim \frac{1}{m(G\rho)^{1/2}} \sim \frac{\lambda_J^{3/2}}{m^{3/2}G^{1/2}} \Rightarrow \lambda_J \sim \frac{1}{m}\left(\frac{\lambda_J}{mG}\right)^{1/2} \sim \frac{1}{mv} \sim \lambda_{dB}. \tag{2.17}$$

Therefore the Jeans wavelength is associated with the de Broglie wavelength and the uncertainty principle is what prevents axions from aggregating: confining the particles inside a smaller region would require an increase in momentum, which would allow them to escape the potential well of DM halos.

By suppressing the formation of small halos and smearing out their central cusp, axions could likely solve the three classic problems of CDM at once if $\lambda_J \approx 1$ kpc, or $m \approx 10^{-22}$ eV [99]. This is much lighter than the QCD axion, so that a single species cannot simultaneously solve the strong CP problem and explain the discrepancies of CDM.

Moreover, recent studies of the Lyman-$\alpha$ forest [100] and stellar streams [101] are in tension with $m \lesssim 10^{-21}$ eV. Fuzzy dark matter might therefore soon be ruled out as a solution to the small-scale crisis.

### 2.3.3 Self-interacting dark matter and hidden sectors

Self-interacting dark matter (SIDM) refers to a wide class of scenarios in which DM self-interactions have a significant impact on their phenomenology. This idea was proposed at the beginning of the small-scale crisis of CDM as a simple alternative to WIMPs [102]. In the minimal model, DM particles can scatter off each other with a velocity-independent (or 'hard sphere') cross section that allows hot particles in the outskirts of the halo to exchange energy with the cold matter in the central region. This heat transfer leads to the dynamical relaxation of the cusp, which expands into a low-density core. Subhalos would also be less concentrated and therefore more prone to disruption by tidal interactions with the host galaxy or ram pressure inside the main halo. Thus, this simple picture could resolve the three main problems of CDM [14, 15].

Numerical simulations have shown that a cross section of order $\sigma/m \approx 0.5$–$5$ cm$^2$ g$^{-1}$ is necessary to solve the small-scale crisis [25], which is partly in tension with the Bullet Cluster bound (2.8). For a time, SIDM seemed almost ruled out as an alternative to CDM because it favors isotropic matter distributions instead of the observed triaxial profiles. The upper bounds initially derived from the ellipticity of halos were about 50 times lower than eq. (2.8) [103], but many have argued that these limits were exaggerated [15, 104, 105].

The first SIDM proposals were quickly followed by scenarios with velocity-dependent cross sections, usually resulting from additional gauge interactions specific to DM, *i.e.*, "dark forces." The idea that DM could constitute a "hidden sector" with its own set of particles and interactions gained a lot of attention due to the wide range of possible phenomenological implications. Indeed, species in the hidden sector are often naturally stabilized by gauge symmetries; they can alleviate the tensions in CDM models (usually through a combination of the effects described above) while avoiding some of the WIMP constraints; and they might address other mysteries in cosmology, astronomy or particle physics.

For instance, if DM is charged under a $U(1)$ gauge group and possesses a massless mediator it can interact via Rutherford scattering, whose cross section is enhanced at low velocities, like in dwarf galaxies, and suppressed in high-energy systems like the Bullet Cluster [106]. Any relativistic species in the hidden sector will damp the power spectrum on small scales, either via free-streaming or Silk damping [107]. Some hidden sectors also favor the early formation of supermassive black holes, whose origin is difficult to explain in standard cosmology [108–110]. Finally, more complex dark sectors like the Twin Higgs model have also been suggested to alleviate the hierarchy problem and other puzzles in the SM [111, 112].

The versatility of hidden sectors is also their shortcoming: given the plethora of possible scenarios, it very difficult to constrain the properties of dark matter in general, since any bound can be avoided by tweaking the models. For instance, the Bullet Cluster limit (2.8) can be totally circumvented if the hidden sector, whose cross section can be arbitrarily large, represents only a fraction of DM ($\lesssim 10$ %) and the rest is non-interacting. Constraints in hidden sectors are model-dependent and therefore have a limited range of applications. The model-building freedom also often comes at the cost of losing predictive power, since those models require the examination of more parameters simultaneously.

Mirror matter is a hidden sector proposal that stands out because, as we will see in chapter 3, its complex evolution is determined by two parameters only, making the model fully predictive. In principle, self-interactions and the mirror baryonic feedback could help explain the CDM discrepancies, but these considerations are beyond the scope of this thesis. Instead, we aim to set bounds on the abundance and temperature of mirror baryons by comparing various astronomical observations with the mirror matter distribution predicted by our structure formation simulation. Future studies might then examine the impact of mirror matter on small-scale structures by focusing on the parameter space that we haven't ruled out.

# Chapter 3

# Mirror cosmology

## 3.1 Mirror matter

The mirror matter hypothesis has first been proposed in the 1960s shortly after the discovery of $CP$ violation in the decays of neutral $K$ mesons [113]. Nishijima and Saffouri suggested that a "shadow" universe identical to our world except for weak interactions could explain the experimental results while maintaining the $CP$ invariance of the theory [114]. Although their model was ruled out by neutrino experiments, it illustrated the ties between spacetime symmetries and a mirror sector (MƧ). Since then, many authors showed that a mirror universe could help solve puzzles in astroparticle physics [17, 109, 110, 115–120] and that this theory could be naturally realized in an $E_8 \otimes E_8$ anomaly-free superstring theory [121].

The idea behind mirror matter models is that a copy of SM particles and interactions exist in a hidden sector. The theory possesses a discrete symmetry that interchanges ordinary particles with their mirror counterparts. Unless that symmetry is spontaneously broken, this implies that visible and mirror species are degenerate and that their respective gauge interactions have equal strength. There are several variations of this model in the literature depending on which particles and interactions are duplicated and how strictly the mirror symmetry is maintained. For instance, the Higgs Parity model is a proposal in which only the $SU(2) \times U(1)$ gauge group has a mirror copy [122], whereas in the original Twin Higgs scenario the SM is fully replicated but the mirror electroweak scale is different [111, 112].

In this thesis, we will focus on the case where the MƧ is identical to the SM; it contains the same species with the same masses and couplings as the visible world (although possibly with different chiralities, see below) and the vacuum structures of the two sectors are the same. More precisely, we can write the Lagrangian of the theory as

$$\mathcal{L} \supset \mathcal{L}_{\mathrm{SM}}(e, u, d, \gamma, W, Z, \ldots) + \mathcal{L}_{\mathrm{SM}}\left(e', u', d', \gamma', W', Z', \ldots\right) + \mathcal{L}_{\mathrm{mix}}, \tag{3.1}$$

where $\mathcal{L}_{\mathrm{SM}}$ is the Standard Model Lagrangian, $\mathcal{L}_{\mathrm{mix}}$ contains portal interactions between the MƧ and the SM, and mirror species are designated by a prime [17, 123].

The $Z_2$ mirror symmetry is made explicit by eq. (3.1): $e \leftrightarrow e'$, $u \leftrightarrow u'$, $\gamma \leftrightarrow \gamma'$, etc. But to understand the original motivation behind the mirror matter proposal, one must take chirality into account. If one assumes that, unlike in the SM, *right*-handed mirror fermions couple to the charged current of the (mirror) weak interaction, then the $Z_2$ transformation actually maps $e_L \leftrightarrow e'_R$. Flipping the chirality also requires the inversion of spatial coordinates for the theory to be invariant, $(t, \vec{x}) \to (t, -\vec{x})$. In other words, the mirror symmetry can be interpreted as a non-standard parity transformation $\mathcal{P}$. In this case, a non-standard time reversal operation $\mathcal{T}$ can be defined such that $\mathcal{P}\mathcal{T} = CPT$, ensuring that $\mathcal{T}$ is also a symmetry and thus making the model invariant under the full Poincaré group. Therefore, mirror matter could restore the left-right symmetry of the universe if the chirality of the MƧ is flipped with respect to the visible world [123]. However, we will not make any assumptions regarding the chirality of mirror fermions since it does not impact the phenomenology of structure formation.

Beside increasing the symmetry of Nature, the main appeal of the MƧ is that it contains the same stable particles as the SM (electrons, protons and nuclei) which could *a priori* constitute all of DM. Its self-interactions also make it a potential alternative to CDM like other hidden sectors, but these considerations fall beyond the scope of this thesis. Since we take the $Z_2$ symmetry to be unbroken, mirror matter comprises the same chemical and nuclear species as ordinary matter and their processes have the same rates. This assumption makes the model fully predictive and allows for a detailed study of seemingly convoluted cosmological events like galaxy formation. We should also remark that, unlike most scenarios of dark galactic structures, mirror matter provides a self-consistent way of populating different galactic structures (*e.g.* a disk or a bulge) and constraining them using astronomical data.

The mirror symmetry allows two renormalizable portal interactions between the SM and the MƧ, namely a gauge kinetic mixing and a Higgs portal coupling:

$$\mathcal{L}_{\text{mix}} = -\frac{\epsilon}{2} F^{\mu\nu} F'_{\mu\nu} - \lambda' \, |h|^2 |h'|^2. \tag{3.2}$$

These are strongly constrained by laboratory experiments [124] and cosmological observations [17, 125]. For simplicity, we will assume that the portal couplings are sufficiently small as to have negligible impact on early cosmology and structure formation. Hence SM particles interact with their mirror counterparts only gravitationally. We should remark that including these two terms in the potential could have a significant impact on the phenomenology of the model: the former would provide mirror particles with a millicharge $\epsilon e$ and the latter would produce two distinct mass eigenstates for the Higgs fields with a degeneracy $\Delta m_h \sim \lambda' v$, where $v \approx 246$ GeV [17].

Under the assumption of unbroken mirror symmetry and negligible portal couplings, the model only has two parameters. As we will show in section 3.2, ordinary and mirror particles cannot be in thermal equilibrium at late times in order to satisfy constraints set by Big Bang nucleosynthesis (BBN) and the cosmic microwave background (CMB). Therefore, we take

$$x \equiv \left(\frac{s'}{s}\right)^{1/3} = \left(\frac{g'_{*,s}(T')}{g_{*,s}(T)}\right)^{1/3} \frac{T'}{T} \tag{3.3}$$

as a free parameter, where $s$ ($s'$) is the entropy density in the SM (MƧ) and the number of effective degrees of freedom in each sector is defined as

$$g_{*,s}(T) = \sum_{i=\text{bosons}} g_i \left(\frac{T_i}{T}\right)^3 + \frac{7}{8} \sum_{i=\text{fermions}} g_i \left(\frac{T_i}{T}\right)^3 . \tag{3.4}$$

In this expression, $g_i = 2S_i + 1$ is the number of internal degrees of freedom for a given species with spin $S_i$ and $T_i$ is its temperature (which can differ from the photon temperature $T$ if it is decoupled from the thermal bath). The two sums in eq. (3.4) run over relativistic species only ($m_i \ll T_i$).

Because we neglected portal interactions between the MƧ and the SM, the entropy of each sector is independently conserved and $x$ is constant. At late times (after ordinary BBN), the only relativistic species in each sector are photons and neutrinos, so that $(g'_{*,s}/g_{*,s})^{1/3} \approx 1$. We can therefore approximate $x \approx T'/T$ at the epoch of interest for structure formation.

Although the relic baryon densities $\Omega_b$ and $\Omega_{b'}$ most likely originate from the same baryogenesis mechanism, their values need not be equal due to the temperature hierarchy between the two sectors. We accordingly take

$$\beta \equiv \frac{\Omega_{b'}}{\Omega_b} \tag{3.5}$$

as a second free parameter. Since the mirror matter density is not fixed, it might represent only a fraction of the total DM content of the universe. This model therefore requires an additional matter component in the form of standard CDM that is assumed to be decoupled from the baryonic sectors. The total matter density in the universe is then

$$\Omega_m = \Omega_c + \Omega_b + \Omega_{b'}, \tag{3.6}$$

where $\Omega_c$ is the CDM fraction.

We should remark that our study is one of the few that let $x$ and $\beta$ vary; most authors fix $x$ to its maximum value allowed by BBN and the CMB and $\beta \approx 1$ or 5, assuming mirror baryons should be as abundant as visible ones or that they constitute all of DM.

However, papers focusing on very early mirror cosmology have argued that these values are not theoretically motivated and that $x$ and $\beta$ could in principle take a wide range of values [16, 121, 126]. We also found that mirror matter distribution in the galactic halo depends strongly on these two parameters. We can thus set meaningful constraints on the model by examining $x$ and $\beta$ only, which will coincidentally limit its possible realizations in the early universe.

Recall that we want to simulate structure formation in the MƧ since mirror particle self-interactions lead to non trivial halo dynamics and matter distribution. First, we must determine the initial conditions of this simulation, *i.e.*, the relative abundance of each chemical species at the beginning of galaxy formation. This will set the rate at which mirror baryons cool down and collapse into galactic structures. The remainder of this chapter is therefore dedicated to the early cosmology of the MƧ, with a focus on BBN and recombination since those events determine the abundances of light nuclei, free electrons and molecular hydrogen. These species all play a major role in galaxy formation as we will see in chapter 4.

## 3.2 Expansion rate of the universe

The expansion rate of the universe is determined by the Friedmann equation,

$$H^2 \equiv \left(\frac{\dot{a}}{a}\right)^2 = \frac{8\pi}{3m_{\rm pl}^2}\sum_i \rho_i, \tag{3.7}$$

where $\rho_i$ represents each individual contribution to the total energy density of the universe. This subsection will focus on the radiation-dominated era of the universe, during which the scale factor evolves as $a(t) \sim t^{1/2}$. A common parametrization of the total relativistic energy density is

$$\rho_{\rm rad}(T) = \frac{\pi^2}{30} g_*(T)\, T^4, \tag{3.8}$$

where the number of effective relativistic degrees of freedom for energy density is defined analogously to eq. (3.4),

$$g_*(T) = \sum_{i=\text{bosons}} g_i \left(\frac{T_i}{T}\right)^4 + \frac{7}{8} \sum_{i=\text{fermions}} g_i \left(\frac{T_i}{T}\right)^4 . \tag{3.9}$$

Mirror matter also contributes to $\rho_{\text{rad}}$ and $H$. We can parametrize the mirror radiative energy density similarly to eq. (3.8):

$$\rho'_{\text{rad}}(T') = \frac{\pi^2}{30} g'_*(T')\, T'^4, \tag{3.10}$$

where $T' = xT$ is the mirror photon background temperature and $g'_*(T')$ is the number of effective degrees of freedom in the MƧ. Combining eqs. (3.7, 3.8, 3.10) gives an expression for the expansion rate of the universe in the presence of mirror particles,

$$H \simeq 1.66 \left(1 + \frac{g'_*(T')}{g_*(T)} x^4\right)^{1/2} \sqrt{g_*(T)}\, \frac{T^2}{m_{\text{pl}}}. \tag{3.11}$$

Like in eq. (3.3), $g'_*(T')/g_*(T) \approx 1$ after ordinary BBN, but this ratio is often lower in the early universe if the two sectors have unequal numbers of relativistic species.

At late times ($T < 0.5$ MeV), another common parametrization for $\rho_{\text{rad}}$ is the following:

$$\rho_{\text{rad}} = \left[1 + \frac{7}{8}\left(\frac{T_\nu}{T}\right)^4 N_{\text{eff}}\right] \rho_\gamma, \tag{3.12}$$

where $N_{\text{eff}}$ is the effective number of neutrino species. Standard cosmology predicts $N_{\text{eff}} = 3.046$ (3 neutrino species plus QED corrections [127]) and $T_\nu/T = (4/11)^{1/3}$ after $e^\pm$ annihilations. The radiative energy from the MƧ is equivalent to additional effective neutrino species,

$$\Delta N_{\text{eff}} = \frac{4}{7}\left(\frac{T}{T_\nu}\right)^4 g'_*(T')\, x^4. \tag{3.13}$$

BBN and CMB put strong limits on the expansion rate and $N_{\text{eff}}$. The most recent data from the Planck Collaboration indicates $N_{\text{eff}} = 2.99^{+0.34}_{-0.33}$ with 95 % confidence at the epoch of recombination [41], which gives the $3\sigma$ limit $\Delta N_{\text{eff}}[\text{CMB}] < 0.45$. At that moment, only photons and neutrinos of each sector are relativistic so $g'_*(T') = g_*(T) = 3.38$, leading to the bound

$$x \lesssim 0.5 \quad \text{(CMB)}. \tag{3.14}$$

The limit on $N_{\text{eff}}$ set by BBN is even more stringent: $\Delta N_{\text{eff}}[\text{BBN}] \lesssim 0.3$ [128, 129]. However, at the onset of BBN ($T \sim 1$ MeV), $e^{\pm}$ pairs have not annihilated yet, which means $T_\nu \approx T$ even if neutrinos are decoupled from photons. Assuming $e'^{\pm}$ are still relativistic at that time, then $g'_*(T') \approx 10$ and the bound on $x$ would be

$$x \lesssim 0.48 \quad \text{(BBN)} \tag{3.15}$$

which is essentially the same as the CMB constraint (3.14). Lower values of $g'_*(T')$ would make this limit less restrictive.

Because the contribution of mirror matter to $H$ scales as $\sim x^4 \ll 1$ (see eq. (3.11)), the chronology of standard cosmological events in the SM is negligibly affected by the hidden sector. On the other end, events tied to a specific temperature scale occurring at redshift $z$ in the visible sector will transpire much earlier in the MS, approximately at a redshift $z' = -1 + (1+z)/x$.

This temperature hierarchy has even greater implications for freeze-out events in the MS. These will generally occur even earlier than the estimated $z'$ because the universe expands more rapidly at a higher redshift. This in turn will make the mirror freeze-out temperature higher, leading to different relic densities in the MS and in the SM. In particular, as we will show in section 3.3, the early freeze-out of $p' \leftrightarrow n'$ interactions in the MS leads to the most prominent feature of mirror matter, namely its high He$'$ abundance.

## 3.3 Primordial nucleosynthesis

### 3.3.1 Elements of statistical mechanics

In thermal equilibrium at a temperature $T$, the number density of a nonrelativistic nuclear species ${}^{A}Z$ with mass $m_A$ and charge $Z$ is [36]

$$n_A = g_A \left(\frac{m_A T}{2\pi}\right)^{3/2} \exp\left(\frac{\mu_A - m_A}{T}\right), \tag{3.16}$$

where $\mu_A$ is the chemical potential and $g_A$ is the number of internal degrees of freedom. That formula also applies to single nucleons.

If all reactions that result in the production of ${}^{A}Z$ are in equilibrium, $\mu_A$ is related to the chemical potential of protons and neutrons by

$$\mu_A = Z\mu_p + (A - Z)\mu_n. \tag{3.17}$$

This relation allows eq. (3.16) to be rewritten in terms of the number density of protons and neutrons:

$$n_A = g_A \frac{A^{3/2}}{2^A} \left(\frac{2\pi}{m_p T}\right)^{3(A-1)/2} n_p^Z n_n^{A-Z}\, e^{B_A/T}, \tag{3.18}$$

where $B_A = Zm_p + (A - Z)m_n - m_A$ is the binding energy of ${}^{A}Z$. Here we approximated $m_p \simeq m_n \simeq m_A/A$ in the prefactor. Given a total baryon density $n_b = n_p + n_n + \sum_A (A n_A)$, the mass fraction of a nuclear species in thermodynamic equilibrium is

$$x_A \equiv \frac{A n_A}{n_b} = g_A \zeta(3)^{A-1} \left[\frac{2^{3A-5} A^5}{\pi^{A-1}} \left(\frac{T}{m_p}\right)^{3(A-1)}\right]^{1/2} \eta_b^{A-1} x_p^Z x_n^{A-Z}\, e^{B_A/T}, \tag{3.19}$$

where we introduced the baryon-to-photon ratio,

$$\eta_b = \frac{n_b - n_{\bar{b}}}{n_\gamma} \simeq \frac{n_b}{n_\gamma}, \tag{3.20}$$

and we replaced the photon number density with its value in thermal equilibrium,

$$n_\gamma = \frac{2\zeta(3)}{\pi^2} T^3. \tag{3.21}$$

### 3.3.2 Ordinary $^4$He formation

In the SM, light nuclei and in particular helium-4 ($^4$He) first formed during BBN [36,37,128]. As mentioned in section 3.2, the thermal history of visible matter is unaffected by mirror matter. In what follows we will therefore approximate $x \approx 0$.

In the primordial universe, when $T \gg 1$ MeV, the following weak interactions were in thermodynamic equilibrium:

$$n \quad \longleftrightarrow \quad p + e + \overline{\nu_e}, \tag{3.22}$$

$$\nu_e + n \quad \longleftrightarrow \quad p + e, \tag{3.23}$$

$$\bar{e} + n \quad \longleftrightarrow \quad p + \overline{\nu_e}. \tag{3.24}$$

This implies the following relation between chemical potentials:

$$\mu_n - \mu_p = \mu_e - \mu_{\nu_e}. \tag{3.25}$$

Using eq. 3.16 we can write the equilibrium ratio of $n$ and $p$ as

$$\frac{n_n}{n_p} = \exp\left(-\frac{\Delta m_{np}}{T} + \frac{\mu_e - \mu_{\nu_e}}{T}\right), \tag{3.26}$$

where $\Delta m_{np} = m_n - m_p = 1.293$ MeV.

The chemical potentials of electrons and neutrinos depend on their particle-antiparticle asymmetry. In the relativistic limit the ratio of the asymmetric abundance of a species $A$

relative to the photon density is [36]

$$\frac{n_A - n_{\bar{A}}}{n_\gamma} = \frac{g_A}{12\,\zeta(3)}\left[\pi^2\left(\frac{\mu_A}{T}\right) + \left(\frac{\mu_A}{T}\right)^3\right]. \tag{3.27}$$

For electrons, this implies $\mu_e/T \sim (n_e - n_{\bar{e}})/n_\gamma = (n_p - n_{\bar{p}})/n_\gamma \sim \mathcal{O}(\eta_b) \ll 1$ to first order, where the equality comes from matter neutrality. Estimating $\mu_{\nu_e}$ would similarly require the measurement of the neutrino asymmetry via the neutrino background radiation, which hasn't been observed yet. We will assume $\mu_{\nu_e}/T \ll 1$, like baryons and charged leptons, so that the neutron-proton ratio is approximated by

$$\frac{n_n}{n_p} \simeq \exp\left(-\frac{\Delta m_{np}}{T}\right). \tag{3.28}$$

Eq. (3.28) holds until the weak interactions (3.23) and (3.24) freeze out. The rate of these reactions is $\Gamma_W \simeq G_F^2 T^5$. Since $H \sim T^2/m_{\rm pl}$ (eq. (3.11)), the freeze-out condition $\Gamma_W = H$ is satisfied at a temperature $T_W \simeq (m_{\rm pl} G_F^2)^{-1/3} = 0.8$ MeV.

The neutron-proton ratio is fixed at its equilibrium value at the time of freeze-out, $(n_n/n_p)_W \simeq 0.2$, except for a small correction due to the neutron decay. This decay stops when light nuclei form.

Although weak interactions are out of equilibrium for $T \lesssim 0.8$ MeV, that is not the case for strong interactions that produce light elements. In particular, the deuterium (D) and $^4$He abundances still satisfy eq. (3.19). Using this equation, one may estimate the temperature $T_{\rm D}$ when D becomes significantly abundant, the so-called "deuterium bottleneck." Assuming $x_{\rm D}/x_n x_p \sim 1$ at that moment yields the following transcendental equation for $T_{\rm D}$:

$$T_{\rm D} \simeq \frac{B_{\rm D}}{(3/2)\ln(m_p/T_{\rm D}) - \ln\eta_b - \ln C}, \tag{3.29}$$

where $B_{\rm D} = 2.22$ MeV is the deuterium binding energy and we have defined the constant

$$C = 3\,\zeta(3)\left(\frac{64}{\pi}\right)^{1/2} \approx 16.28. \tag{3.30}$$

The factor of 3 comes from the fact that deuterium is a spin 1 nucleus and possesses $g_{\rm D} = 3$ internal degrees of freedom.

Numerically solving eq. (3.29) gives $T_{\rm D} \simeq 0.07$ MeV. The age of the universe at this moment is:

$$t_{\rm D} = \frac{1}{2H(t_{\rm D})} \simeq \frac{1}{3.32\sqrt{g_*}}\frac{m_{pl}}{T_{\rm D}^2} \approx 260 \text{ s}, \tag{3.31}$$

where the number of relativistic degrees of freedom is $g_* \sim 3.38$.

Between $t_{\rm D}$ and the weak interactions freeze-out ($t_W \sim 1$ s $\ll t_{\rm D}$), a fraction $[1 - \exp(-t_{\rm D}/\tau_n)]$ of neutrons decayed into protons, where $\tau_n = 886.7$ s is the neutron lifetime. At $t_{\rm D}$ the neutron-proton ratio has decreased to

$$\begin{aligned}\left(\frac{n_n}{n_p}\right)_{\rm D} &= \left(\frac{n_n}{n_p}\right)_W \frac{\exp\left(-t_{\rm D}/\tau_n\right)}{1 + (n_n/n_p)_W\ \left[1 - \exp\left(-t_{\rm D}/\tau_n\right)\right]}\\ &= \frac{\exp\left(-t_{\rm D}/\tau_n\right)}{1 + \exp\left(\Delta m_{mn}/T_W\right) - \exp\left(-t_{\rm D}/\tau_n\right)} \approx 0.14.\end{aligned} \tag{3.32}$$

Given the high formation rates of light elements past the bottleneck, to a very good approximation we can assume that every neutron will end up in D nuclei, all of which will then combine to form $^4$He. Since 2 neutrons are required to form $^4$He, its primordial mass fraction is roughly

$$\begin{aligned}Y \equiv x_{^4{\rm He}} = 2x_n = 2\left(\frac{n_n}{n_p}\right)_{\rm D} \left[\frac{1}{1 + (n_n/n_p)_{\rm D}}\right]\\ = \frac{2\exp\left(-t_{\rm D}/\tau_n\right)}{1 + \exp\left(\Delta m_{mn}/T_W\right)}\ \approx\ 0.24.\end{aligned} \tag{3.33}$$

The simple analysis that resulted in eq. (3.33) is consistent with the observed $^4$He abundance in the universe [20]. The next stable element in the nuclear chain is carbon-12 ($^{12}$C) which may only form via the triple-alpha process, $3\,(^4\mathrm{He}) \to {}^{12}\mathrm{C} + \gamma$. Because this reaction requires the collision of three particles and because matter is cooling rapidly, $^{12}$C formation is negligible in the early universe and BBN stops at $^4$He formation.

### 3.3.3 Mirror $^4$He formation

BBN in the MƧ proceeds exactly like in the SM, except that all critical temperatures are reached at an earlier time. Therefore, a simple rescaling of eq. (3.33) allows for an estimation of the $^4\mathrm{He}'$ mass fraction.

The weak interaction rate in the MƧ is given by $\Gamma'_W \simeq G_F^2 T'^5$ and the expansion rate can be approximated by $H \sim (1+x^{-4})^{1/2} T'^2/m_{\mathrm{pl}}$. Therefore the mirror freeze-out temperature is roughly $T'_W = (1+x^{-4})^{1/6}\ T_W$. The mirror deuterium bottleneck temperature can be obtained by changing $\eta_b \to \eta_{b'} = (\beta/x^3)\eta_b$ in eq. (3.29), but the dependence of $T_{\mathrm{D}}$ on the MƧ parameters $x, \beta$ is only logarithmic. So to a good approximation $T'_{\mathrm{D}} \simeq T_{\mathrm{D}}$. According to eq. (3.31) the age of the universe at the D$'$ bottleneck would then be given by $t'_{\mathrm{D}} = t_{\mathrm{D}}/(1+x^{-4})^{1/2}$. Substituting $T'_W$ and $t'_{\mathrm{D}}$ into eq. (3.33) yields the $^4\mathrm{He}'$ mass fraction,

$$Y' \simeq \frac{2\exp\left[-t_{\mathrm{D}}/\tau_n(1+x^{-4})^{1/2}\right]}{1+\exp\left[\Delta m_{mn}/T_W\ (1+x^{-4})^{1/6}\right]}. \tag{3.34}$$

This formula is plotted in fig. 3.1.

Because we neglected the logarithmic dependence of $T'_{\mathrm{D}}$ on $\eta_{b'}$, eq. (3.34) is $\beta$-independent. A more accurate treatment of BBN is required to determine how the density of mirror baryons affects the freeze-out temperature of light nuclei and their relic abundances. We used the code `AlterBBN` [130,131] to numerically compute the residual $^4\mathrm{He}'$ mass fraction for different values of $\beta$, modifying parameters of the code to match the conditions of the MƧ. Namely the current CMB temperature, the baryon density and the baryon-to-photon ratio were replaced by $T_0 \to T_0/x$, $\Omega_b \to \beta\Omega_b$ and $\eta_b \to \eta_b\beta/x^3$. Visible sector photons and neutrinos were incorporated as additional effective neutrino species. Rewriting eq. (3.13) from the

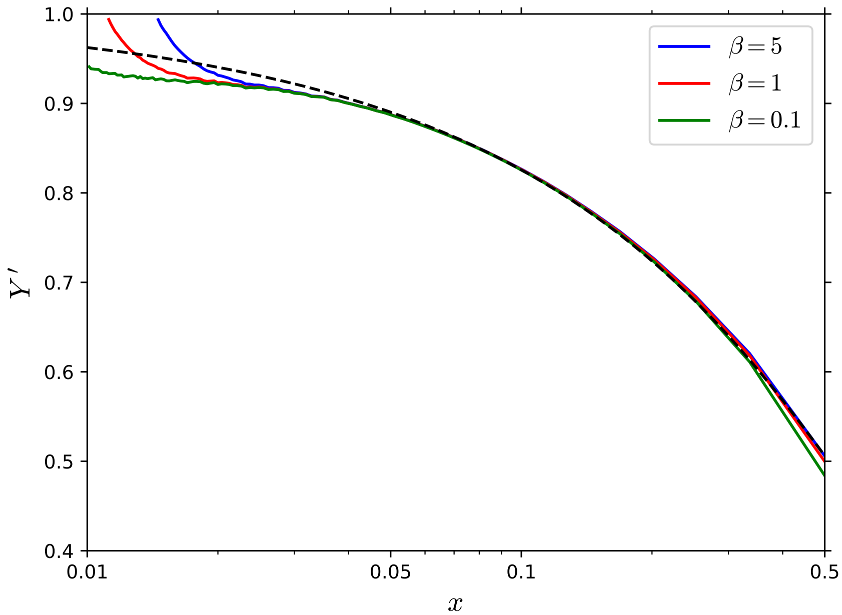


Figure 3.1: Mirror $^4$He relic abundances. The solid curves were computed numerically using `AlterBBN` and the dashed line shows the approximate formula of eq. (3.34).

perspective of the mirror world yields $\Delta N'_{\text{eff}} \simeq 7.44/x^4$ today. The results of our numerical calculations are also plotted in fig. 3.1 for three benchmark values of $\beta$. Eq. (3.34) agrees with the numerical calculations within a few percent, which is sufficient for the purposes of our analysis.

One sees that for any value of $\beta$, the $^4\text{He}'$ fraction computed numerically reaches 1 more rapidly than eq. (3.34) as $x$ decreases below some critical value. This is admittedly the result of `AlterBBN`'s limitations: the code is not suited to handle the situation where the $\text{H}'$ abundance vanishes since that species is used as a reference to normalize other abundances. Thus it cannot accurately keep track of very small $\text{H}'$ densities. Moreover the age of the universe at D formation scales roughly as $t'_{\text{D}} \sim x^2$. Hence for small values of $x$ mirror nucleosynthesis occurs in a fraction of a second and the Boltzmann equations for each species become too stiff for `AlterBBN` to maintain a high accuracy. But this has no impact on our main results since both eq. (3.34) and the numerical calculations agree that the $^4\text{He}'$ abundance is limited to $0.9 < Y' < 1$ for small values of $x$. The results presented in chapter 5 show little phenomenological variation within this range, so we can self-consistently claim that eq. (3.34) is accurate enough for our purposes.

The $^4$He$'$ abundance determines a number of other quantities that will be useful in the subsequent analysis. Let $X_i \equiv n_i/n_{\rm H}$ be the relative abundance of a given chemical species, conventionally normalized to the H$'$ density.[6] The helium-hydrogen number ratio is

$$X_{\rm He} \equiv \frac{n_{\rm He}}{n_{\rm H}} = \frac{m_p}{m_{\rm He}} \frac{Y'}{1-Y'} \simeq \frac{1}{4}\frac{Y'}{1-Y'}, \tag{3.35}$$

where $m_p$ is the proton mass. Furthermore the helium number fraction (distinct from the mass fraction $Y' = m_{\rm He}n_{\rm He}/(m_{\rm He}n_{\rm He} + m_{\rm H}n_{\rm H})$) is

$$f_{\rm He} \equiv \frac{n_{\rm He}}{n_N} = \frac{1}{1+1/X_{\rm He}} \simeq \frac{Y'}{4-3Y'}, \tag{3.36}$$

with $n_N = n_{\rm H} + n_{\rm He}$ denoting the number density of nuclei. The mean mass per nucleus is

$$\overline{m_N} = \left(\frac{1-Y'}{m_p} + \frac{Y'}{m_{\rm He}}\right)^{-1} \simeq \frac{m_p}{1-\frac{3}{4}Y'}. \tag{3.37}$$

By virtue of the approximation made in eq. (3.34), the expressions (3.35-3.37) are independent of $\beta$. Lastly, the background number density of nuclei at any redshift follows from

$$n_N = \frac{3H_0^2\Omega_b}{8\pi G}\frac{\beta}{\overline{m_N}}(1+z)^3 \ , \tag{3.38}$$

where we have used $\rho_{b'}(z) \propto (1+z)^3$ and $\rho_{\rm crit,0} = 3H_0^2/8\pi G$. Eq. (3.38) implies that $n_{\rm H} = (1-f_{\rm He})n_N$ and $n_{\rm He} = f_{\rm He}n_N$.

[6] In what follows, we will drop the prime from H$'$ and H will refer to mirror hydrogen in all its chemical forms whereas $H^0$, $H^+$ and $H_2$ designate its neutral, ionized and molecular states respectively. Thus for a gas of pure $H_2$, $n_{\rm H} = 2n_{\rm H_2}$. Similarly, He refers to all forms of mirror helium.

## 3.4 Recombination

Recombination is the cosmological formation of neutral atoms around the time of matter-radiation decoupling. In the SM, although most electrons end up in bound states after recombination, a small ionization fraction remains. That fraction was essential for structure formation, because primordial gas clouds required free electrons to cool and collapse into compact structures [35]. Therefore, understanding the evolution of the free electron abundance in the MƧ is a crucial step to study the formation of mirror galaxies.

As for BBN, recombination follows the same principles in the MƧ as in the SM and the outcome depends solely on the initial conditions. It proceeds through three major steps, which are the respective formations of $He^+$, $He^0$ and $H^0$. The latter is prevalent in the SM, but recombination of He is more important in the MƧ because of its high abundance.

For all three steps of recombination, electrons cannot directly transition from a free state to the ground state when they are captured by ions. This is because photons emitted in those transitions would immediately ionize other atoms, leading to no net change in the ionization fraction. Instead, electrons must cascade down a series of excited states before reaching their ground state, emitting multiple low-energy photons along the way [132, 133].

An effective description of recombination is a "3-level atom" model [134]. In this approximation one may only be concerned with three energy levels: the ground state ($n = 1$), the first excited state ($n = 2$) and a continuum of unbound states ($n \to \infty$). In this picture, electrons must fall into the $n = 2$ level when they are captured by nuclei. Electrons with orbital angular momentum $l = 1$ ($2p$ state) can then transition directly to the $n = 1$ level, emitting a single K$\alpha$ photon (also referred to as a Lyman-$\alpha$ (Ly$\alpha$) photon for H). On the other hand, $l = 0$ electrons ($2s$ orbital) must decay via a two-photon quantum process since the $2s$-$1s$ dipole transition is forbidden.

### 3.4.1 $\mathrm{He}^+$ recombination

In the two sectors, $\mathrm{He}^+$ recombination occurs very rapidly and at an early time. This is in part due to the high ionization energy of $\mathrm{He}^+$ ($\chi_{\mathrm{He}^+} = 54.4$ eV), but mostly because its two-photon $2s$-$1s$ transition rate dominates over the K$\alpha$ rate [133]. Instead, recombination dominated by the $2p$-$1s$ transition is slower in general, because the K$\alpha$ photons would excite electrons out of their ground state, leaving them vulnerable to photo-ionization from the background radiation. The two photons of the $2s$-$1s$ transition don't have enough energy to excite atoms so they don't impede recombination. Because it is fast, $\mathrm{He}^+$ recombination follows the Saha equation to a good approximation:

$$\frac{\left(X_e - 1 - X_{\mathrm{He}}\right) X_e}{1 + 2X_{\mathrm{He}} - X_e} = \frac{\left(2\pi m_e kT\right)^{3/2}}{h^3 n_{\mathrm{H}}} e^{-\chi_{\mathrm{He}^+}/kT}. \tag{3.39}$$

Matter neutrality requires $X_e = X_{\mathrm{H}^+} + X_{\mathrm{He}^+} + 2X_{\mathrm{He}^{++}}$ at all times. In the visible sector, $\mathrm{He}^+$ recombination occurred around $z \simeq 6000$, when $kT \sim 1.4$ eV. At this temperature, the exponential in eq. (3.39) is negligible, giving $X_e = 1 + X_{\mathrm{He}}$. Eliminating $X_e$ and using the fact that $X_{\mathrm{H}^+} \simeq 1$ and $X_{\mathrm{He}^0} \simeq 0$ until $T$ falls below $\sim 0.4$ eV (about 10 % of the $n = 2$ ionization energies of H or He), this implies $X_{\mathrm{He}^{++}} \simeq 0$. Thus, we can neglect any residual $\mathrm{He}^{++}$ fraction and both H and He are singly ionized from that point on. The same argument applies to the MS, but at a redshift $z' \simeq 6000/x$ instead.

### 3.4.2 $\mathrm{He}^0$ and $\mathrm{H}^0$ recombinations

$\mathrm{He}^0$ and $\mathrm{H}^0$ recombinations are much slower. The former is dominated by the optically thick K$\alpha$ emission, and although the latter is controlled by the two-photon $2s$-$1s$ transition, its rate is much lower than for $\mathrm{He}^+$ [133]. Therefore, the Saha equation cannot be used to accurately describe the later stages of recombination. Below, we will go over Peebles' derivation of the Boltzmann equation for H recombination [132], which can be adapted to give a similar formula for He [133].

Let $n_\gamma^{(\nu)}$ be the photon number per unit volume and frequency range. Then

$$n_{\gamma,\alpha} = \int_{\nu_\alpha}^{\nu_\alpha^+} n_\gamma^{(\nu)}\, d\nu \tag{3.40}$$

is the photon number density in the frequency range $[\nu_\alpha, \nu_\alpha^+]$, where $\nu_\alpha$ is the Ly$\alpha$ frequency and $\nu_\alpha^+$ is a frequency slightly above the Ly$\alpha$ resonance band.

The time evolution of $n_{\gamma,\alpha}/n_N$ depends only on the photon production rate per unit volume $R_\alpha$ in this frequency range and on the redshift of higher-frequency photons. The bounds of the integral (3.40) are fixed *physical* frequencies $\nu = \nu_c/a$. As the universe expands, higher comoving frequencies $\nu_c$ fall into the range of the integral, which leads to the following rate equation:

$$\begin{aligned}\frac{d}{dt}\left(\frac{n_{\gamma,\alpha}}{n_N}\right) &= \frac{\partial}{\partial t}\left(\frac{n_{\gamma,\alpha}}{n_N}\right) + \frac{R_\alpha}{n_N} \\ &= \frac{1}{n_N}\left[H\nu_\alpha\left(n_\gamma^{(\nu_\alpha^+)} - n_\gamma^{(\nu_\alpha)}\right) + R_\alpha\right].\end{aligned} \tag{3.41}$$

The evolution of $n_{\gamma,\alpha}$ is very slow since the $2p$-$1s$ transition quickly replaces the redshifted photons, leaving the Ly$\alpha$ resonance band in a steady state. It is therefore justified to set the left-hand side of eq. (3.41) to zero [132], which gives

$$n_\gamma^{(\nu_\alpha)} = n_\gamma^{(\nu_\alpha^+)} + \frac{R_\alpha}{H\nu_\alpha}. \tag{3.42}$$

Because $\nu_\alpha^+$ is above the Ly$\alpha$ line, the only contribution to the radiation spectrum at this frequency is the thermal background,

$$n_\gamma^{(\nu_\alpha^+)} = \frac{8\pi(\nu_\alpha^+)^2}{e^{h\nu_\alpha^+/kT} - 1} \approx 8\pi\nu_\alpha^2 e^{-h\nu_\alpha/kT} \tag{3.43}$$

where we have approximated $\nu_\alpha^+ \approx \nu_\alpha$ and $T \ll \nu_\alpha$ at the time of recombination. Eqs. (3.42-3.43) may be rewritten in terms of $\mathcal{N} = n_\gamma^{(\nu)}/8\pi\nu^2$, the number of photons per mode at frequency $\nu$:

$$\mathcal{N}_\alpha(z) = e^{-h\nu_\alpha/kT} + \frac{R_\alpha \lambda_\alpha^3}{8\pi H(z)}, \tag{3.44}$$

where $\lambda_\alpha$ is the Ly$\alpha$ wavelength.

The lifetime of Ly$\alpha$ photons is very short during recombination, which implies it is in equilibrium with matter. The principle of detailed balance indicates that

$$\mathcal{N}_\alpha = \frac{n_{\mathrm{H},2}}{n_{\mathrm{H},1}}, \tag{3.45}$$

where $n_{\mathrm{H,i}}$ is the number density of $\mathrm{H}^0$ atoms in the $i$th energy level. One should note that $n_{\mathrm{H}^0} \equiv n_{\mathrm{H},1}$, that is, we define fully recombined $\mathrm{H}^0$ atoms to be those that are in the ground state only.

The H ionization fraction evolves following the Boltzmann equation:

$$\begin{aligned} \frac{dX_{\mathrm{H}^+}}{dt} &= -\left(\frac{n_e n_{\mathrm{H}^+} \alpha_\mathrm{H}}{n_\mathrm{H}} - \frac{n_{\mathrm{H},2}\beta_\mathrm{H}}{n_\mathrm{H}}\right) \\ &= -\left(X_e X_{\mathrm{H}^+} n_\mathrm{H} \alpha_\mathrm{H} - \mathcal{N}_\alpha X_{\mathrm{H}^0} \beta_\mathrm{H}\right). \end{aligned} \tag{3.46}$$

In this expression, $\alpha_\mathrm{H}$ and $\beta_\mathrm{H}$ are the recombination and photoionization rates of the $n = 2$ energy level, since H cannot recombine from the ionized state. We also assume that thermal background cannot ionize the ground state.

Every net recombination results in the production of either a Ly$\alpha$ photon or two photons of lower energy, which gives the relation

$$X_e X_{\mathrm{H}^+} n_\mathrm{H} \alpha_\mathrm{H} - \mathcal{N}_\alpha X_{\mathrm{H}^0} \beta_\mathrm{H} = \frac{R_\alpha}{n_\mathrm{H}} + \Lambda_\mathrm{H} X_{\mathrm{H}^0} \left(\mathcal{N}_\alpha - e^{-h\nu_\alpha/kT_M}\right), \tag{3.47}$$

where the second term on the right-hand side parametrizes the $2s$-$1s$ transition. We have ignored the small energy difference between the $2s$ and $2p$ states so that they are both roughly $\sim h\nu_\alpha$ above the ground state. Here, $T_M$ is the matter temperature, which can be different from the radiation temperature $T$, but only long after recombination. Therefore, in what follows we will assume $T_M \approx T$ except when explicitly computing the late-time evolution of $T_M$.

Combining eqs. (3.44-3.47) yields an expression for $\mathcal{N}_\alpha$, which can then be plugged in eq. (3.46) to obtain the Peebles equation:

$$\frac{dX_{\mathrm{H}^+}}{dz} = \frac{\Big(X_e X_{\mathrm{H}^+} n_\mathrm{H} \alpha_\mathrm{H} - (1 - X_{\mathrm{H}^+}) \beta_\mathrm{H} e^{-h\nu_\alpha/kT_M}\Big)\Big(1 + K_\mathrm{H}\Lambda_\mathrm{H} n_\mathrm{H}(1 - X_{\mathrm{H}^+})\Big)}{H(z)\;(1+z)\Big(1 + K_\mathrm{H}(\Lambda_\mathrm{H} + \beta_\mathrm{H}) n_\mathrm{H}(1 - X_{\mathrm{H}^+})\Big)}, \tag{3.48}$$

where we have defined

$$K_\mathrm{H} = \frac{\lambda_\alpha^3}{8\pi H(z)}. \tag{3.49}$$

We also used $dt = -dz/[H(z)(1+z)]$ and we approximated $X_{\mathrm{H}^0} + X_{\mathrm{H}^+} \approx 1$, neglecting the small contributions from the short-lived excited states of $\mathrm{H}^0$.

$\mathrm{He}^0$ recombination follows a very similar pattern. However, the separation of the $2s$ and $2p$ states is sufficiently large that it cannot be ignored [133]. Since $\mathcal{N}$ is defined as the ratio of atoms in the $2s$ and the $1s$ states, it must be replaced with $\mathcal{N} \to \mathcal{N}\exp(-h\nu_{ps}/kT)$ in eq. (3.44) — which only concerns photons of the $2p$-$1s$ transition — where $\nu_{ps} = \nu_p - \nu_s$ is the frequency difference between the $2p$-$1s$ and the $2s$-$1s$ transitions of $\mathrm{He}^0$. In the same equation, the Ly$\alpha$ frequency $\nu_\alpha$ must also be replaced with $\nu_p$, while we must instead use $\nu_s$ in the last term on the right-hand side of eq. (3.47). Following the same steps as above leads to the $\mathrm{He}^0$ recombination equation:

$$\begin{aligned}\frac{dX_{\mathrm{He}^+}}{dz} &= \Big(X_e X_{\mathrm{He}^+} n_\mathrm{H} \alpha_\mathrm{He} - \beta_\mathrm{He}(X_\mathrm{He} - X_{\mathrm{He}^+}) e^{-h\nu_s/kT_M}\Big) \\ &\times \frac{\Big(1 + K_\mathrm{He}\Lambda_\mathrm{He} n_H (X_\mathrm{He} - X_{\mathrm{He}^+}) e^{h\nu_{ps}/kT_M}\Big)}{H(z)\;(1+z)\Big(1 + K_\mathrm{He}(\Lambda_\mathrm{He} + \beta_\mathrm{He}) n_\mathrm{H}(X_\mathrm{He} - X_{\mathrm{He}^+}) e^{h\nu_{ps}/kT_M}\Big)}.\end{aligned} \tag{3.50}$$

One also needs an equation for the matter temperature $T_M$ to fully solve for the recombination evolution. At early times, matter remains in thermal equilibrium with radiation due to the high Thomson scattering rate of free electrons. After recombination, the electron abundance drops and radiation decouples from matter. At this point the temperature of nonrelativistic particles redshifts as $T_M \sim a^{-2}$, faster than $T$. The cosmological evolution of $T_M$ is then given by

$$\frac{dT_M}{dz} = \frac{8\sigma_T a_R T^4}{3H(z)\,(1+z)\,m_e c}\left(\frac{X_e}{1+X_{\rm He}+X_e}\right)(T_M - T) + \frac{2T_M}{(1+z)}. \tag{3.51}$$

Eqs. (3.48-3.51) fully determine the evolution of the ionization fraction for both the SM and the MƧ. The values of all parameters used in this system are given in Appendix A.

We used `Recfast++` [134–140] to solve the system (3.48-3.51). For mirror recombination, we made the the same modifications to the code as for `AlterBBN`, with the $\mathrm{He}'$ mass fraction given by eq. (3.34). It was assumed that the species were initially singly ionized ($X_{\rm H^+} = 1$, $X_{\rm He^+} = X_{\rm He}$) and that matter was strongly coupled to radiation ($T_M = T$). The initial redshift was taken to be sufficiently high to encompass the beginning of $\mathrm{H}^0$ and $\mathrm{He}^0$ recombination, and the system was evolved until $z = 10$, the moment when we started our subsequent structure formation analysis. Fig. 3.2 shows the resulting evolution of the free electron fraction $f_e = n_e/n_{e,\rm tot}$ (where $n_{e,\rm tot}$ includes the electrons in the ground state of $\mathrm{He}^+$) during recombination for several values of $x$ (differentiated by color) and $\beta$ (differentiated by linestyle) as well as in the visible sector. The expected $x$-dependence of the redshift of recombination $z'_{\rm rec} \sim 1100/x$ is evident, scaling inversely to the MƧ temperature.

The most important feature for mirror structure formation is the residual ionization fraction $f'_e$ at low redshifts. As fig. 3.2 demonstrates, $f'_e$ is typically much smaller in the MƧ than in the SM ($f_e \sim 2\times10^{-4}$). Only when $\beta \ll 1$ can $f'_e$ reach higher values, because the low density reduces the number of ion-electron collisions and the overall efficiency of recombination. But in this case the total electron density is also suppressed by a factor of $\beta$, so the free electron density after recombination is always smaller in the MƧ.

Fig. 3.3 shows the $(x, \beta)$-dependence of the residual ionization fractions of H and He

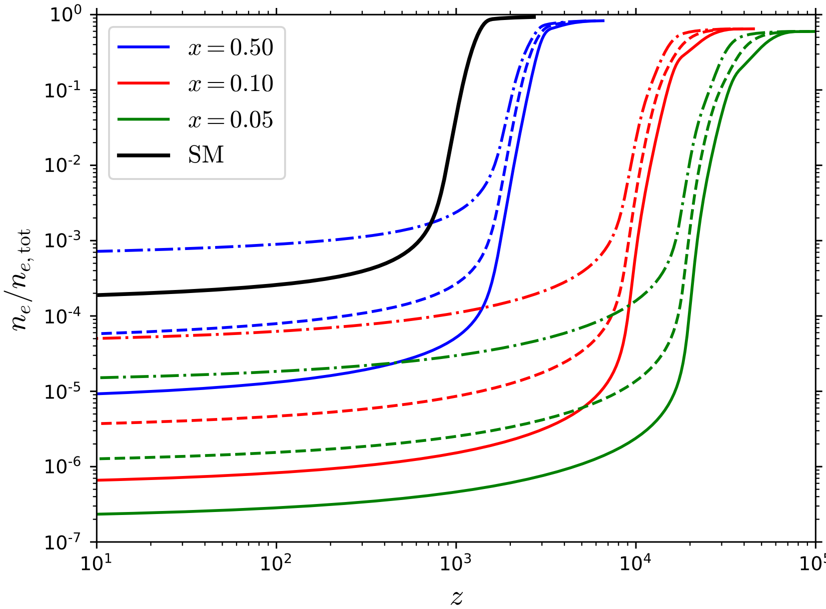


Figure 3.2: Evolution of the total ionization fraction during mirror recombination. The solid, dashed and dash-dotted curves represent $\beta = 5$, 1 and 0.1, respectively. Also shown for comparison is recombination in the SM.

at $z = 10$. For comparison, the SM values (at $x = 1$, $\beta = 1$, $Y = 0.24$) are $n_{\mathrm{H}^+}/n_{\mathrm{H}} = 2.2 \times 10^{-4}$ and $n_{\mathrm{He}^+}/n_{\mathrm{He}} = 1.2 \times 10^{-12}$. Recombination of He is more efficient (blue regions) for high $\beta$, because a larger mirror matter density increases the collision rate between ions and free electrons. As $x$ decreases, the interval between the beginning of recombination ($z'_{\mathrm{rec}} \simeq 1100/x$) and $z = 10$ becomes longer, increasing the number of occasional ion-electron collisions following freeze-out. This and the slightly larger value of $n_{\mathrm{He}}$ explain the somewhat higher efficiency of He recombination at low $x$.

We can also understand qualitative features of fig. 3.3 concerning H recombination. In contrast to He, there is a much stronger variation of $n_{\mathrm{H}}$, which changes by a factor of 60 as $x$ goes from $10^{-3}$ to 0.5, as compared to only a factor of 2 variation in $n_{\mathrm{He}}$. In particular, for $x \ll 1$ the low density of H is overwhelmed by free electrons, requiring relatively few collisions to recombine such that H may become neutral before He does so. In this situation, for $\beta \sim 1$, H recombination takes place much earlier than for He and it is more efficient than in the SM. But since He recombines very effectively, the number of free electrons available for

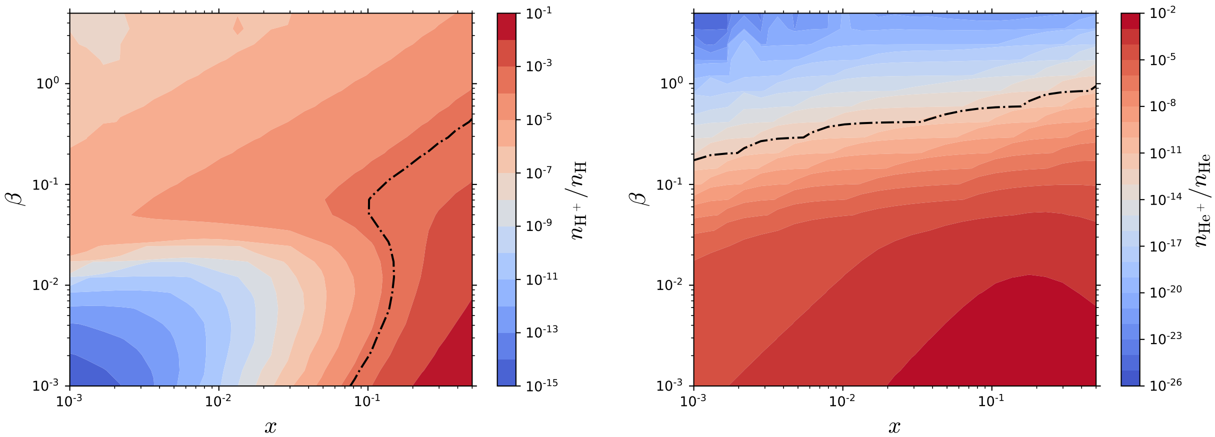


Figure 3.3: Residual ionization fractions $n_{\mathrm{H}^+}/n_{\mathrm{H}}$ (left) and $n_{\mathrm{He}^+}/n_{\mathrm{He}}$ (right) of the MƧ at $z = 10$. The dot-dashed contours indicate the SM values: $n_{\mathrm{H}^+}/n_{\mathrm{H}} = 2.2 \times 10^{-4}$ and $n_{\mathrm{He}^+}/n_{\mathrm{He}} = 1.2 \times 10^{-12}$.

hydrogen-electron collisions after the freeze-out drops significantly, leading to a much higher ionization fraction than for He. For $\beta \ll 1$, He recombination is very inefficient, leaving a larger number of free electrons to combine with H, and leading to a small ionization fraction. In the region where $x \gtrsim 0.1$, hydrogen and helium number densities are almost equal, and their ionization fractions display a similar qualitative dependence on $\beta$.

## 3.5 $H_2$ formation

$H_2$ is an important molecular species for structure formation since it can cool a primordial gas cloud to a temperature as low as $\sim 200$ K [109, 141]. As we will show in section 4.4, in the MƧ even a small fraction of $H_2$ can act as an effective heat sink that drives the collapse of large clouds into stellar objects. Conversely, without $H_2$, a virialized gas cloud of mirror helium might not cool below a temperature of order $10^4$ K (roughly 10 % of the ionization energy of helium and hydrogen), preventing structure formation.

Since $H_2$ has no dipole moment, it cannot form directly from the collision of two neutral

H atoms. Instead, at early times its formation proceeds through the reactions

$$\begin{aligned} H^0 + e^- &\to H^- + \gamma, \\ H^- + H^0 &\to H_2 + e^-. \end{aligned} \tag{3.52}$$

$H_2$ is always energetically favored at low temperatures, but the low matter density and ionization fractions inhibit its production after recombination. Hence $H_2$ can only form during recombination, when both $n_e$ and $n_{H^0}$ are significant. Other mechanisms involving $H_2^+$ and $HeH^+$ are known to contribute to the residual $H_2$ abundance, but these processes are subdominant [142].

As was shown in ref. [142], the production of $H_2$ depends on the abundance of $H^-$, which in the steady-state approximation is:

$$X_{H^-} = \frac{k_7 X_e X_{H^0} n_H}{k_{-7} + k_8 X_{H^0} n_H + k_9 X_e n_H + k_{15} X_{H^+} n_H}. \tag{3.53}$$

The rates $k_i$ are listed in table B.3 of Appendix B.

The residual $H_2$ abundance is determined by integrating the Boltzmann equation

$$\frac{dX_{H_2}}{dt} = k_8 X_{H^0} X_{H^-} n_H. \tag{3.54}$$

Since both $H^-$ and $H_2$ attain low abundances, their presence has little effect on recombination. We can integrate eq. (3.54) using the time evolution of $X_{H^0}$ and $X_e$ numerically computed in the previous subsection. The fraction of $f_2' = n_{H_2}/n_H$ produced by $z = 10$ is illustrated in fig. 3.4. For reference, the same analysis in the SM yields $f_2 \simeq 6 \times 10^{-7}$. We find that $f_2'$ is always greater than $f_2$, analogously to the higher efficiency of mirror recombination.

The degree of enhancement $f_2'/f_2$ depends on the timing of He recombination versus that of H, since $H_2$ requires both neutral H and free $e^-$ for its formation. When $\beta, x \sim 1$,

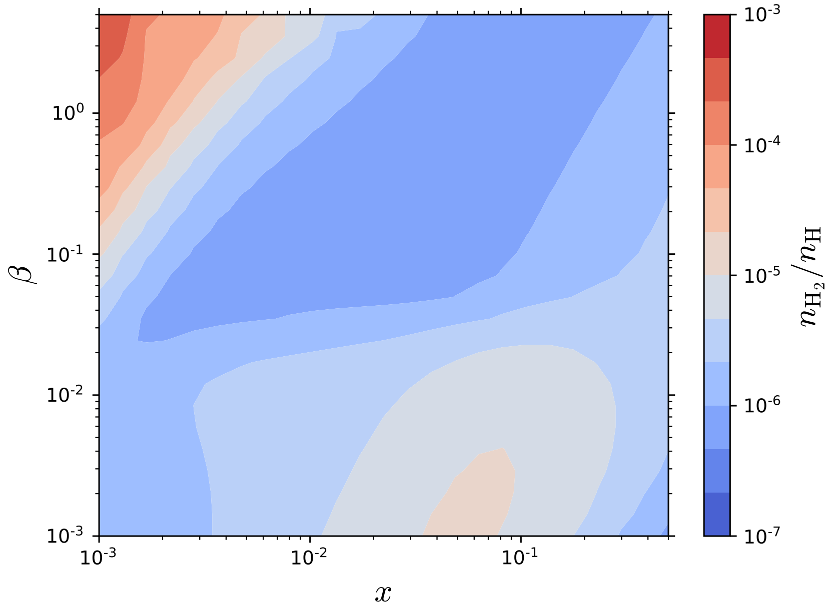


Figure 3.4: Residual fraction $f_2' = n_{\mathrm{H}_2}/n_{\mathrm{H}}$ produced during mirror recombination at $z = 10$. This fraction is higher than the SM value of $n_{\mathrm{H}_2}/n_{\mathrm{H}} \simeq 6 \times 10^{-7}$ for any $(x, \beta)$.

recombination proceeds similarly as in the SM: He recombines efficiently and prior to H, leaving too few $e^-$ for $H_2$ to form. As $\beta$ decreases, He recombination becomes incomplete and the extra $e^-$ density produces more $H_2$. For $x \ll 1$ but $\beta \sim 1$, H recombines before He, leading to simultaneously high abundances of neutral H and free $e^-$. This explains the enhanced $H_2$ production in fig. 3.4. If both $x \ll 1$ and $\beta \ll 1$, the two recombinations overlap, leaving fewer $e^-$ to produce molecules.

# Chapter 4

# Mirror structure formation

Our current understanding of structure formation is that galaxies formed following a bottom-up hierarchy: small-scale adiabatic matter perturbations grew linearly with the expansion of the universe until they became large enough to collapse into small halos, which expanded further by accreting matter and merging with other halos. The shock-heated baryons then radiated their energy away, allowing them to cool and condense into stars and galactic structures [35].

In this chapter we will review the main steps of structure formation in our mirror dark matter model in order to constrain $x$ and $\beta$ using astronomical observations. We will review the theory of perturbation growth and explain how we estimated the merger history of the MW halo. We will also review the concepts of radiative cooling in a gas cloud and gravitational collapse. With all these ingredients in hand, we will describe the methodology of our galaxy formation simulation. This chapter closely follows section III of ref. [19], the paper written by the author of this thesis.

## 4.1 Perturbation growth and halo merger tree

The extended Press-Schechter formalism [143–145], which we summarize in this section, is an analytic description of the statistical growth and merger history of a halo. The evolution of the MW halo will serve as a starting point to study the formation of a mirror matter galaxy within it.

If small-scale linear density perturbations $\delta_i = (\rho_i - \overline{\rho_i})/\overline{\rho_i}$ are adiabatic, their Fourier modes $\mathbf{k}$ evolve following the equation

$$\ddot{\delta}_{i,k} + 2H\dot{\delta}_{i,k} + \frac{k^2 c_i^2}{a^2}\delta_{i,k} = \frac{3}{2}H^2\,\Omega_m(t)\sum_j \delta_{j,k}, \tag{4.1}$$

where $c_i$ is the adiabatic sound speed and the indices $i, j$ refer to the matter components (CDM, ordinary matter or mirror particles). The adiabatic speed of sound of baryonic components is given by [146]

$$c_b^2(z) \equiv \frac{\partial p}{\partial \rho} = \frac{1}{3}\left(1 + \frac{3\rho_b(z)}{4\rho_\gamma(z)}\right)^{-1} = \frac{1}{3}\left[1 + \frac{45\Omega_b\rho_{\mathrm{crit},0}}{4\pi^2 T_0^4}\left(\frac{1}{1+z}\right)\right]^{-1}, \tag{4.2}$$

$$c_{b'}^2(z) \equiv \frac{\partial p'}{\partial \rho'} = \frac{1}{3}\left(1 + \frac{3\rho_{b'}(z)}{4\rho_{\gamma'}(z)}\right)^{-1} = \frac{1}{3}\left[1 + \frac{45\Omega_b\rho_{\mathrm{crit},0}}{4\pi^2 T_0^4}\frac{\beta}{x^4}\left(\frac{1}{1+z}\right)\right]^{-1}, \tag{4.3}$$

where we used $p = \rho_\gamma/3$ in each sector. Since CDM does not interact with radiation, its speed of sound is null ($c_c^2 = 0$).

During the radiation-dominated era ($H = 1/2t$, $\Omega_m(t) \ll 1$), matter overdensities don't grow significantly on small scales: visible and mirror baryons are strongly coupled to radiation and oscillate with it while the CDM component can only grow logarithmically: $\delta_c \sim \ln t$. Starting from matter-radiation equality, CDM density perturbations grow as $\delta_c \sim D(z)$, where we defined the linear growth coefficient as

$$D(z) = CH(z)\int_z^\infty \frac{1+z'}{H(z')^3}\,dz', \tag{4.4}$$

and $C$ is a normalization constant such that $D(0) = 1$. Note that in a matter-dominated universe $D(z) = a = (1+z)^{-1}$, but the growth slows down when dark energy becomes significant.

Ordinary baryon perturbations also scale as $D(z)$, but only once they decouple from radiation and become pressureless ($c_b^2 \approx 0$), which occurs roughly at the same time as recombination, around $z_{\rm rec} = 1100$. On the other hand, mirror baryons can grow as early as matter-radiation equality, like CDM. That is because recombination takes place at $z'_{\rm rec} \approx 1100/x$, which is earlier than $z_{\rm eq} = 3365$[7] for $x \lesssim 0.3$. But even for higher values of $x$, $c_{b'}^2$ is roughly suppressed by a factor of $x^4 \ll 1$ (eq. (4.3)), which means that mirror matter is effectively pressureless and follows the evolution of CDM.

Once a matter overdensity reaches $\delta_m = (3/5)(3\pi/4)^{2/3} \approx 1.0624$ on a given comoving scale (regardless of the relative abundance of each matter component), it becomes nonlinear and collapses under its self-gravity [35]. The collapse stops at a redshift $z_{\rm col}$ at which point the linear overdensity is

$$\delta_{\rm col} = \frac{3}{5}\left(\frac{3\pi}{2}\right)^{2/3}\left[\Omega_m(z_{\rm col})\right]^{0.0055} \approx 1.686\left[\Omega_m(z_{\rm col})\right]^{0.0055}. \tag{4.5}$$

One must be careful when interpreting $\delta_{\rm col}$: it is the comoving overdensity that the initial perturbation *would have had* at $z_{\rm col}$ had it continued to scale linearly as $D(z)$. That quantity is mainly used to relate an initial overdensity $\delta_i$ with the redshift $z_{\rm col}$ at which its gravitational collapse took place (see Appendix C for an example). At $z_{\rm col}$, the matter perturbation reaches a quasi-static state and forms a virialized halo with an actual average overdensity

$$\Delta_{\rm vir}(z_{\rm col}) = \frac{18\pi^2 + 82y - 39y^2}{\Omega_m(z_{\rm col})}, \tag{4.6}$$

where we have defined $y = \Omega_m(z_{\rm col}) - 1$.

Once halos form, their growth "breaks away" from the expansion of the universe. Their mass continues to increase, but only via matter accretion and mergers. Let $M_2$ be the mass of a given halo at time $t_2$. The mass fraction $f_{12}(M_1, M_2)dM_1$ of $M_2$ that was in halos in the

[7] Our bound on $x$ from CMB and BBN ensures that $z_{\rm eq}$ does not change significantly due to the presence of mirror radiation.

interval $[M_1, M_1 + dM_1]$ at a time $t_1 < t_2$ is [143–145, 147]

$$f_{12}(M_1, M_2)\, dM_1 = \frac{1}{\sqrt{2\pi}} \frac{\left(\delta^0_{\mathrm{col},1} - \delta^0_{\mathrm{col},2}\right)}{\left(\sigma_1^2 - \sigma_2^2\right)^{3/2}} \, \frac{d\sigma_1^2}{dM_1} \exp\left( -\frac{1}{2} \frac{\left(\delta^0_{\mathrm{col},1} - \delta^0_{\mathrm{col},2}\right)^2}{\left(\sigma_1^2 - \sigma_2^2\right)} \right) dM_1. \tag{4.7}$$

In that expression, we have defined $\delta^0_{\mathrm{col},i} = \delta_{\mathrm{col}}(t_i)/D(t_i)$, which is the linear overdensity of eq. (4.5) extrapolated to $z = 0$. We have also introduced $\sigma_i^2 = \sigma^2(R_i)$, the variance of the linear matter power spectrum $\mathcal{P}(k)$ inside a sphere of comoving radius $R_i = (3M_i/4\pi\rho_{m,0})^{1/3}$, also extrapolated to $z = 0$.

Formally, the power spectrum $\mathcal{P}(k)$ is defined as the Fourier transform of the matter correlation function $\xi(\mathbf{r}) \equiv \langle \delta(\mathbf{x} + \mathbf{r})\delta(\mathbf{x})\rangle$, that is,

$$\mathcal{P}(k) = V \int \xi(\mathbf{r}) e^{i\mathbf{k}\cdot\mathbf{r}} \, \mathrm{d}^3\mathbf{r}, \tag{4.8}$$

where $V$ is a fiducial volume. Its variance is given by:

$$\sigma^2(R) = \frac{1}{2\pi^2} \int_0^\infty k^2 \, \mathcal{P}(k) \, |W(kR)|^2 \, dk, \tag{4.9}$$

where for the present analysis we used the top-hat window function,

$$W(kR) = \frac{3}{(kR)^3} \, \big(\sin(kR) - kR\cos(kR)\big). \tag{4.10}$$

Taking $t_2 = t_1 + dt$ with $dt \to 0$, eq. (4.7) becomes

$$\frac{df_{12}}{dt} = \frac{1}{\sqrt{2\pi}} \frac{1}{\left(\sigma_1^2 - \sigma_2^2\right)^{3/2}} \frac{d\delta^0_{\mathrm{col},1}}{dt} \frac{d\sigma_1^2}{dM_1}. \tag{4.11}$$

Eq. (4.11) gives the relative contribution of objects in $[M_1, M_1 + dM_1]$ to the total growth rate of the main halo. The average number of halos in this mass range that combined during

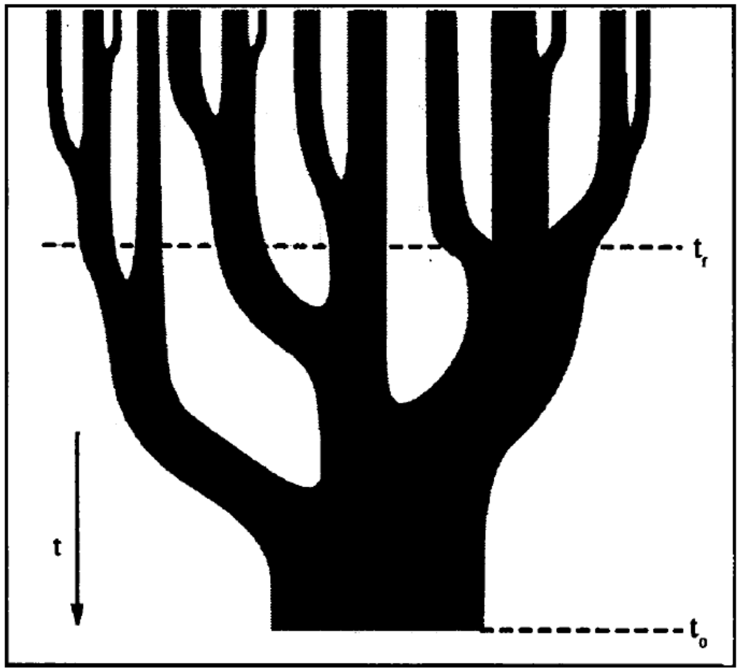


Figure 4.1: Diagram of a merger tree. To generate it, one must start from the bottom ($z = 0$) and take small steps backwards in time. At each time step the halo loses some mass due to matter accretion and there is a small probability of splitting into two subhalos, producing two branches in the tree. We followed the evolution of every branch above the resolution scale until $z = 10$. Figure taken from [35, 149].

$dt$ to form the halo of mass $M_2$ is therefore

$$dN = \frac{df_{12}}{dt} \frac{M_2}{M_1} \, dt \, dM_1. \tag{4.12}$$

The algorithm presented in refs. [147, 148] uses eq. (4.12) to find the progenitors of a halo of mass $M_2$ by taking small steps $dt$ backwards in time. We will outline this procedure below. The resulting "merger tree" describes the hierarchical formation of the halos observed at $z = 0$ regardless of the distribution or the nature of matter inside of them. Fig. 4.1 shows the diagram of a merger tree.

Numerically, one must define a resolution scale $M_{\rm res}$ below which there is no further tracking of individual halos. The probability that a halo of mass $M_2$ splits into halos of masses $M_1 \in [M_{\rm res}, M_2/2]$ and $(M_2 - M_1)$ in a backward step $dt$ is

$$P = \int_{M_{\rm res}}^{M_2/2} \frac{dN}{dM_1}\, dM_1. \tag{4.13}$$

Accretion of objects smaller than $M_{\rm res}$ also contributes to the growth of the halo during that period. The fraction of mass that is lost to those smaller fragments in the reverse time evolution is

$$F = \int_0^{M_{\rm res}} \frac{dN}{dM_1}\frac{M_1}{M_2}\, dM_1. \tag{4.14}$$

The algorithm to generate the merger tree is as follows. Starting at redshift $z_f$ with a single halo of mass $M_2 = M_f$, a backward time step $dt$ is taken, with $dt$ small enough that $P \ll 1$. A random number $R$ is generated from a uniform distribution between 0 and 1. If $R > P$, the halo does not fragment, but still loses a fraction of mass $F$ due to the accretion of matter below the resolution scale. Thus the mass of the halo at the next time step becomes $(1-F)M_2$. If $R < P$, the halo splits into two halos of mass $M_1$ and $(1-F)M_2 - M_1$ where $M_1$ is chosen randomly from the distribution given by eq. 4.12. These steps are repeated for every progenitor whose mass is above $M_{\rm res}$ until the chosen initial redshift $z_i$ is reached.

We used this algorithm to generate 10 merger trees for a final halo mass of $M_f = 10^{12}\ M_\odot$, about the size of the MW. The time interval between $z_f = 0$ and $z_i = 10$ was divided into $10^4$ logarithmically scaled time steps. The resolution was set to $M_{\rm res} = 3 \times 10^7\ M_\odot$, well below $M_f$ but large enough to avoid keeping track of too many halos simultaneously. To minimize possibly large statistical fluctuations, we used the ensemble of merger trees to average over all derived quantities in the end. By averaging over all outcomes, we are also applying the cosmological principle: the MW halo is not special and its evolution is similar to that of other halos of the same size. Inspection of the individual trees indicated that 10 was more than sufficient to avoid spurious effects of outliers.

Eq. 4.7 and the algorithm described above are completely model-independent, to the extent that matter overdensities are Gaussian. This allows us to use the same 10 merger trees in scanning over all values of $x$ and $\beta$ for structure formation. However $\mathcal{P}(k)$ depends on the nature of dark matter, which in turn affects the variance $\sigma^2(R)$ in eqs. (4.7,4.11-4.14). For simplicity, we computed $\sigma^2$ with `Colossus` [150], even though this package assumes a $\Lambda$CDM cosmology. For self-consistency, it is necessary to verify that the matter power spectrum and its variance do not differ too much from their standard cosmology expressions in the presence of a mirror sector. We discuss this issue below.

## 4.2 Silk damping

In the early universe, photons and baryons are tightly coupled, making the mean free path of photons $\lambda_\gamma$ negligible. But at the onset of recombination $\lambda_\gamma$ becomes significant. Photons can then diffuse out of overdense regions, effectively damping perturbations on scales smaller than the Silk scale $\lambda_D$, which we derive below. In the SM, the mass scale corresponding to the Silk length is $M_D \sim 10^{12}\ M_\odot$ [36], about the mass of the Milky Way halo. Structure formation below this scale is strongly inhibited, unless a significant component of CDM allows small-scale perturbations to grow.

Mirror matter can be similarly affected by collisional damping. Since we observe structures on scales smaller than $M_D$, Silk damping sets a lower bound on the amount of ordinary CDM required for the mirror model to agree with current data. A detailed analysis of cosmological perturbations, acoustic oscillations and the matter power spectrum for any value of $x$ and $\beta$ is outside the scope of this thesis. However, we can roughly estimate the impact of Silk damping on $\mathcal{P}(k)$ and the merger tree to check that the evolution of the MW halo is not too different from the $\Lambda$CDM scenario. Many other effects could alter $\mathcal{P}(k)$, like extra oscillations on scales smaller than the sound horizon of the mirror matter plasma [151], but Silk damping has the largest impact on our structure formation analysis. In particular, small-scale perturbations must be able to grow sufficiently for galaxy formation to proceed hierarchically. Hence we estimate the size of the MƧ counterpart of the damping scale, $\lambda'_D$, and its implications for the growth of MƧ density perturbations.

### 4.2.1 Mirror Silk scale

One can estimate the MƧ Silk scale as follows [36]. The mean free path of MƧ photons at low temperatures is

$$\lambda_{\gamma'} = \frac{1}{n_e \sigma_T} = \frac{1}{\xi_e n_N \sigma_T}, \tag{4.15}$$

where $\sigma_T$ is the Thomson scattering cross section and $\xi_e \equiv n_e/n_N$ is the ionization fraction during H and He$^0$ recombination (that is, neglecting the electrons in the ground state of He$^+$). During an interval $\Delta t$, a photon experiences $N = \Delta t/\lambda_{\gamma'}$ collisions. The average comoving distance $\Delta r$ traveled in this time is that of a random walk with a characteristic step of length $\lambda_{\gamma'}/a$,

$$(\Delta r)^2 = N \frac{\lambda_{\gamma'}^2}{a(t)^2} = \frac{\lambda_{\gamma'} \Delta t}{a(t)^2}. \tag{4.16}$$

Taking the limit $\Delta t \to 0$ and integrating until recombination gives

$$\begin{aligned} \lambda_D'^2 &= \int_0^{t_{\rm rec}} \frac{\lambda_{\gamma'}}{a(t)^2} dt \\ &\simeq -\lambda_{\gamma'}(z'_{\rm rec}) \; (1+z'_{\rm rec})^3 \int_{z'_{\rm rec}}^{\infty} \frac{1}{1+z} \left(\frac{dt}{dz}\right) dz, \end{aligned} \tag{4.17}$$

using the fact that $\lambda_{\gamma'}$ scales as $n_N^{-1} \sim a^3$ and approximating $\xi_e$ as constant for the period of interest when $\lambda_{\gamma'}$ is large.

For simplicity, consider the case $x \ll 0.3$ so that mirror recombination completes during the radiation-dominated era (recall section 4.1). Then $t \sim (1+z)^{-2}$ and eq. (4.17) reduces to

$$\lambda_D'^2 \simeq \frac{2}{3} t'_{\rm rec} \; \lambda_{\gamma'}(z'_{\rm rec}) \; (1+z'_{\rm rec})^2. \tag{4.18}$$

In the case where recombination occurs much later than $z_{\rm eq}$ (like in the SM), we would obtain the same expression but the numerical coefficient would be 3/5 instead of 2/3. Therefore the expression (4.18) is accurate within $\sim 10\,\%$ for any value of $x$ and even for the SM. Since $\lambda_D'^2 \sim \lambda_{\gamma'}(z'_{\rm rec}) \sim x^3/\beta$, in general $\lambda'_D \ll \lambda_D$, unless $\beta$ is very small and the mirror matter plasma is diluted before recombination. Therefore mirror Silk damping only affects very small scales and its impact on $\mathcal{P}(k)$ is usually less significant than the analogous effect in the SM.

To further quantify $\lambda'_D$, we note that at early times when vacuum energy is negligible so that $\Omega_m + \Omega_{\rm rad} = 1$, the age of the universe at a given redshift is [21]

$$t(z) = \frac{2}{3H_0\sqrt{\Omega_{\rm m}}}\frac{1}{(1+z_{\rm eq})^{3/2}}\left[2+\left(\frac{1+z_{\rm eq}}{1+z}-2\right)\sqrt{\frac{1+z_{\rm eq}}{1+z}+1}\right], \tag{4.19}$$

which for $z \gg z_{\rm eq}$ simplifies to

$$t(z \gg z_{\rm eq}) \simeq \frac{1}{2H_0\sqrt{\Omega_{\rm m}}}\frac{\sqrt{1+z_{\rm eq}}}{(1+z)^2}. \tag{4.20}$$

Using eqs. (3.38) and (4.20) we can rewrite eq. (4.18) in terms of $\beta$ and $x \ll 1$:

$$\lambda_D'^2 \simeq \frac{8\pi G}{9H_0^3\sqrt{\Omega_m}\Omega_b}\left(\frac{\overline{m}_N x^3}{\xi_e \sigma_T \beta}\right)\frac{\sqrt{1+z_{\rm eq}}}{(1+z_{\rm rec})^2}. \tag{4.21}$$

where we used $\xi_e \sim 0.1$ at the time of recombination. For larger values of $x$, $z'_{\rm rec}$ is close to $z_{\rm eq}$ and we cannot assume a fully matter- or radiation-dominated universe to compute the integral of eq. (4.17); nevertheless we verified that eq. (4.21) is accurate to within several percent even for $x > 0.3$.

### 4.2.2 Effect on the merger tree evolution

Section 4.2.1 allows us to quantify the impact of collisional damping on density perturbations in the MS and on the merger tree. Consider a mirror baryonic overdensity $\delta_{b',k}$ on a subhorizon scale $\lambda = \pi/k$. Assuming primordial perturbations are adiabatic, we have $\delta_{b',k} = \delta_{c,k}$ at early times ($z \gg z_{\rm eq}$). $\delta_{c,k}$ remains nearly constant prior to matter-radiation equality (ignoring a small logarithmic growth). However Silk damping suppresses $\delta_{b',k}$ by a factor $\sim \exp\left(-k^2/k_D'^2\right)$ after recombination [35], where $k_D' = \pi/\lambda_D'$.

For very small values of $\beta$, the MƧ constitutes only a small fraction of DM and the power spectrum is not significantly affected by mirror Silk damping. Therefore in what follows we only consider the scenario $\beta \gtrsim 0.1$, where consequently $\lambda_D \gg \lambda_D'$. The analysis below focuses on scales sufficiently small so that SM baryonic perturbations are always negligible compared to CDM and MƧ overdensities ($\delta_{b,k} \approx 0$).

As discussed below eq. (4.4), both CDM and mirror components grow as $D(z)$ during the matter-dominated era, which means their ratio is fixed to its value at $z_{eq}$. Let $f_i \equiv \Omega_i/\Omega_{\rm DM}$ be the fractions of the total DM density, such that $f_c + f_{b'} = 1$. Therefore the total DM density perturbation at $z_{eq}$ is:

$$\delta_{\rm DM,k} \equiv f_c\, \delta_{c,k} + f_{b'}\, \delta_{b',k} = \delta_{c,k}\, \left(1 - f_{b'}(1 - e^{-k^2/k_D'^2})\right), \tag{4.22}$$

where we combined the initial abadiatic condition $\delta_{b',k} = \delta_{c,k}$ with the exponential Silk damping. Since $\mathcal{P}(k) \sim \delta_k^2$, then we see that mirror matter damps the power spectrum by a factor $\sim \mathcal{F}_D^2$ compared to standard ΛCDM cosmology, where

$$\mathcal{F}_D = \left(1 - \frac{\beta\Omega_b}{\Omega_{\rm DM}}(1 - e^{-k^2/k_D'^2})\right). \tag{4.23}$$

To verify that our merger tree evolution is not significantly altered by the suppression of $\mathcal{P}(k)$ on small scales, we applied the damping factor 4.23 to the ΛCDM matter power spectrum, and we computed the variance $\sigma^2(R)$ and the integral $P$ of eq. (4.13) for a MW-like halo ($M_2 = 10^{12}\ M_\odot$) with this extra feature. Fig. 4.2 illustrates the damping of $\mathcal{P}(k)$ and $\sigma^2(R)$ due to mirror particles for $\beta = 5$ and a few benchmark values of $x$.

$P$ is the probability for a merger to happen and it is roughly inversely proportional to the lifetime of large halos $t_{\rm halo}$, which we will properly define in section 4.5. The accretion rate $F$ given by eq. (4.14) also affects $t_{\rm halo}$, but for large halos it represents such a small

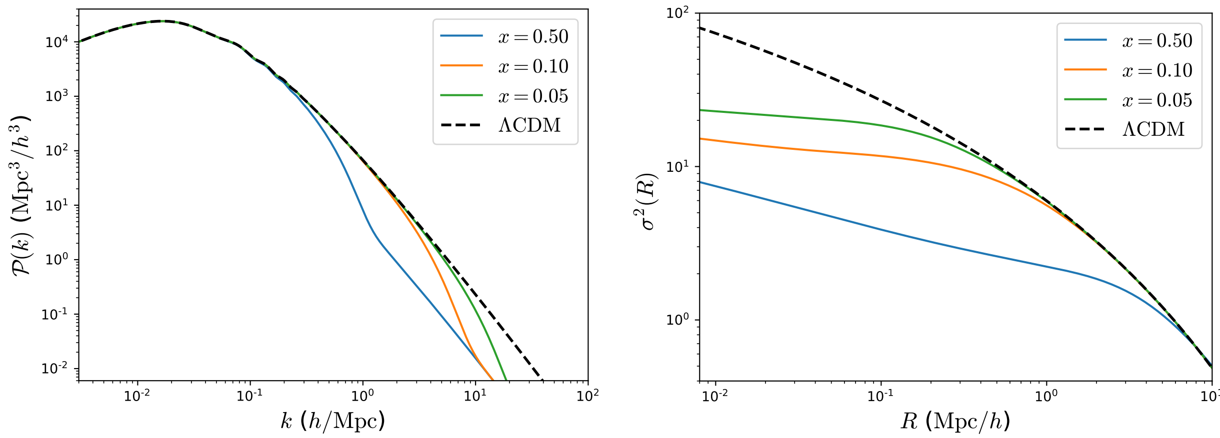


Figure 4.2: Effect of mirror Silk damping on the matter power spectrum $\mathcal{P}(k)$ (left) and variance $\sigma^2(R)$ (right) for $\beta = 5$ and comparison with standard ΛCDM cosmology. Note that every curve for $\sigma^2(R)$ is normalized so that $\sigma_8 \equiv \sigma(8\ \text{Mpc/h}) = 0.815$, following the Planck results [41].

fraction of the total mass that we can ignore it. Let $P_D$ be the value of the integral (4.13) computed with the damped power spectrum. We therefore expect that the lifetime should scale as $t_{\text{halo}} \sim P/P_D$.

In our 10 merger trees, the average lifetime of the Milky Way halo is 6.9 Gyr with a relative standard deviation of 21.5 %. To ensure the self-consistency of our analysis, we demand that the Silk damping does not change the average lifetime by more than $2\sigma$, or 43 %. In other words, our analysis is valid only if $0.57 < P/P_D < 1.43$; outside this region we cannot trust our conclusions because the merger trees would be too drastically affected by the damping effects. Our results are illustrated in fig. 4.3. We find that two regions above $\beta \gtrsim 3.7$ must be excluded from our analysis: for $0.02 \lesssim x \lesssim 0.12$, $t_{\text{halo}}$ would be much longer than the estimate we obtained using the ΛCDM power spectrum; whereas for $x \gtrsim 0.2$, the halo lifetime in the presence of mirror matter would be too small.

Note that the different behaviors in these two regions come from two competing effects in eq. (4.11): both $|d\sigma_1^2/dM_1|$ and $(\sigma_1^2 - \sigma_2^2)^{3/2}$ are suppressed by the collisional damping, but the latter effect dominates for large values of $x$, when the Silk scale is large. Interestingly, those effects cancel out around $x \approx 0.15$ and we can still use our structure formation analysis

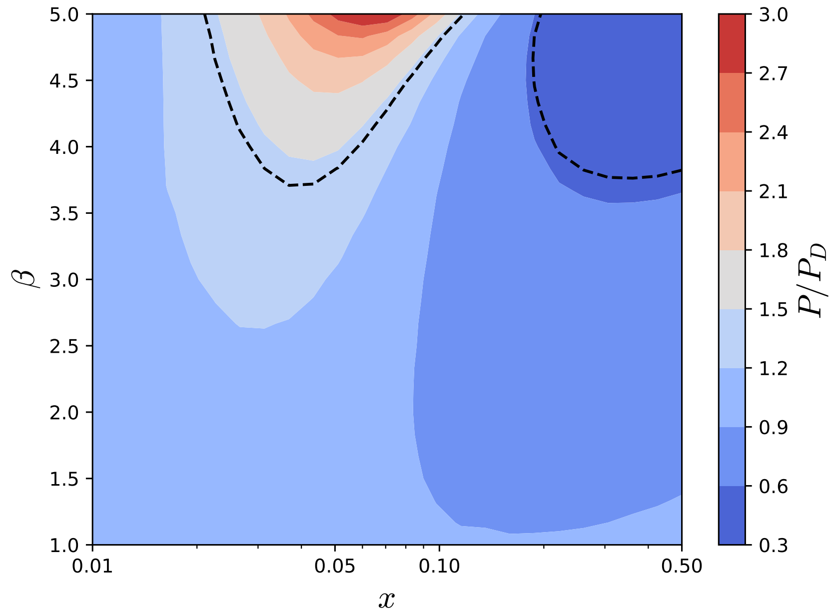


Figure 4.3: Ratio $P/P_D$ ($\sim t_{\text{halo}}$) of the halo splitting probability (eq. (4.13)) without and with mirror Silk damping. The regions above the dashed curves are outside the self-consistency range $0.57 < P/P_D < 1.43$ and are excluded from our analysis.

to constrain the scenario where mirror matter makes up all DM in this region. Fortunately, the high temperature region also corresponds to the parameter space that is more likely to be constrained by cosmological observables like the CMB or the matter power spectrum. In particular, these constraints allowed ref. [18] to rule out mirror matter from making up all DM ($\beta \approx 5$) if $x \gtrsim 0.3$.

## 4.3 Cooling of primordial gas clouds

After the gravitational collapse and virialization of density perturbations, CDM and mirror particles adopt different density profiles in the halos [147] (we ignore visible baryons in our structure formation analysis, see section 4.5). CDM has a cuspy NFW density profile,

$$\rho_c(r) = \frac{(\Omega_c/\Omega_m)(\Delta_{\rm vir}\rho_{\rm crit}/3)}{\left[\ln(1+c) - \dfrac{c}{1+c}\right] \dfrac{r}{r_{\rm vir}} \left(\dfrac{r}{r_{\rm vir}} + \dfrac{1}{c}\right)^2}. \tag{4.24}$$

Mirror matter instead forms a cored isothermal profile,

$$\rho_{b'}(r) = \frac{f_{\rm hot}(\Omega_{b'}/\Omega_m)(\Delta_{\rm vir}\rho_{\rm crit}/3)}{\left[1 - \dfrac{r_0}{r_{\rm vir}} \tan^{-1}\left(\dfrac{r_{\rm vir}}{r_0}\right)\right] \left(\left(\dfrac{r}{r_{\rm vir}}\right)^2 + \left(\dfrac{r_0}{r_{\rm vir}}\right)^2\right)}. \tag{4.25}$$

The virial radius $r_{\rm vir}$ is the radius of a sphere inside which the average overdensity is equal to $\Delta_{\rm vir}$ (eq. (4.6)). Both profiles are truncated at $r_{\rm vir}$. The NFW concentration $c$ sets the size of the central region of the CDM profile. The procedure to find $c$ for a given halo mass at a given redshift is described in Appendix C [152]. Note that the CDM profile remains constant throughout the lifetime of the halo.

The hot gas fraction $f_{\rm hot} = 1$ for all newly formed halos, but $f_{\rm hot}$ decreases as the gas cools and collapses. The core radius $r_0$ is initially related to the NFW concentration as $r_0/r_{\rm vir} = 1/(3c)$, but as the gas cools, $r_0$ increases such that the density and pressure at $r_{\rm vir}$ remain unaffected. This is impossible in the limit where a large fraction of the gas cools, so we set an upper limit of $r_0 = 15r_{\rm vir}$ to avoid a numerical divergence as $r_0 \to \infty$. In this limit $(r/r_{\rm vir})^2 \ll (r_0/r_{\rm vir})^2$ and the density profile becomes essentially homogeneous.

Since mirror matter is not pressureless, its collapse leads to accretion shocks that heat the gas to a temperature of roughly [35]

$$T_M = (\gamma - 1)\ T_{\rm vir} = (\gamma - 1)\ \frac{1}{2}\frac{GM\mu}{r_{\rm vir}}, \tag{4.26}$$

where $\gamma$ is the adiabatic index of the gas, $\mu$ is the mean molecular mass, $M$ is the total mass of the halo including CDM. For simplicity, we will assume the gas is purely monatomic, which sets $\gamma = 5/3$.

The temperature of a virial halo is always much greater than the temperature of the matter background. This means the baryonic pressure $p = \rho T/\mu$ becomes nonnegligible and prevents further collapse of mirror matter. In order for galaxies to form, mirror baryons must radiate energy, which is why structure formation is impossible without an efficient cooling mechanism.

Let $\mathcal{C}_i$ be the cooling rate of a given process $i$, in units of energy per unit time per unit volume. If several reactions contribute to the total $\mathcal{C}$, we can define the cooling timescale as

$$t_{\mathrm{cool}}(r) = \frac{3}{2}\frac{n(r)T_M}{\sum_i \mathcal{C}_i(r, T_M)}. \tag{4.27}$$

where $n(r)$ is the number density of all chemical species combined. Therefore $t_{\mathrm{cool}}$ is roughly the time required for the gas to radiate all its kinetic energy. For two-body cooling processes, $\mathcal{C}_i \sim n^2$. Since $n$ decreases monotonically with $r$, the cooling timescale increases as we move further away from the center of the halo. We now briefly describe the various contributions to $\mathcal{C}$ [35, 153–155].

### 4.3.1 Radiative processes

**Inverse Compton scattering.** At early times, electrons can scatter off background photons and transfer their kinetic energy to the radiation field. The cooling rate for this process is

$$\mathcal{C}_{\mathrm{Comp}} = \frac{4T_M}{m_e}\sigma_T n_e a_R T^4. \tag{4.28}$$

where $T_M$ is the matter temperature (given by eq. (4.26)), $T$ is the radiation temperature, $\sigma_T$ is the Thomson scattering cross section and $a_R$ is the radiation constant. Because the expansion of the universe redshifts $T$, inverse Compton cooling becomes negligible at late times. Also, since $T_M$ is usually much greater than $T$ inside virialized halos, standard Compton scattering (in which the photons transfer energy to particles) can safely be neglected.

**Bremsstrahlung.** At very high temperatures the gas will be fully ionized and will primarily cool via free-free emissions (bremsstrahlung). As free electrons scatter off ions, they emit radiation and cool at a rate

$$\mathcal{C}_{\rm ff} = \frac{16\alpha^3 g_{\rm ff}}{3}\left(\frac{2\pi T}{3m_e^3}\right)^{1/2} n_e \sum_{\rm ions} n_i Z_i^2. \tag{4.29}$$

The sum runs over the ionized species ($H^+$, $He^+$ and $He^{++}$) and $Z_i$ is their electric charge. For our analysis we took the Gaunt factor to be $g_{\rm ff} \simeq 1$.

**Atomic transitions.** When the ionization fraction of the gas is too small, bremsstrahlung becomes inefficient. At this point atomic processes take the lead in the cooling of the gas. As ions and free electrons recombine to form neutral atoms, they radiate energy. Atoms can also collide with free electrons which will temporarily excite or ionize the atom until they return to their ground state, losing energy by emitting photons. The atomic cooling rates $\mathcal{C}_{\rm atom}$ for all processes we considered are given in table B.1 of Appendix B. Note that the collision rate between atoms is much smaller than electron-atom scattering since free electrons have a much higher velocity at a given temperature. We can therefore neglect atom-atom collisions in our analysis.

**Molecular transitions.** Atomic cooling can only bring the gas to a temperature of $\sim$ 5 000 K (about 0.5 eV), since below this point electrons don't carry enough energy to excite or ionize the atoms. But unlike atoms, molecular hydrogen possesses rotational and vibrational modes which are easily excited by collisions. As the molecules return to their ground state, they emit low-energy photons which allow the temperature to drop to $\sim$ 200 K if $H_2$ is sufficiently abundant.

The cooling function for molecular hydrogen can be parametrized as follows [154–156]:

$$\mathcal{C}_{\rm mol} = \frac{n_{\rm H_2} L_{\rm LTE}}{1 + L_{\rm LTE}/L_{\rm low}} \tag{4.30}$$

The $L$'s are cooling coefficients associated with rotational and vibrational modes excited by collisions with other species, either in local thermodynamic equilibrium (LTE) or in the low density regime. The LTE coefficient can be split into the contributions from rotational and vibrational excitations: $L_{\rm LTE} = L_{\rm LTE}^{\rm rot} + L_{\rm LTE}^{\rm vib}$ [155], where:

$$L_{\rm LTE}^{\rm rot} = \left[ \left( \frac{9.5 \times 10^{-22} T_3^{3.76}}{1 + 0.12 T_3^{2.1}} \right) e^{-(0.13/T_3)^3} + (3 \times 10^{-24}) e^{-0.51/T_3} \right] \ \text{erg s}^{-1}, \tag{4.31}$$

$$L_{\rm LTE}^{\rm vib} = \left[ (6.7 \times 10^{-19}) e^{-5.86/T_3} + 1.6 \times 10^{-18} e^{-11.7/T_3} \right] \ \text{erg s}^{-1}. \tag{4.32}$$

In these expressions $T_3 = T/(10^3 \text{ K})$.

In the low density limits, each species excite $H_2$ with a different rate. One way to parametrize this is to write

$$L_{\rm low} = \sum_k L_k n_k, \tag{4.33}$$

where $k$ represents either $H^0$, $H^+$, $H_2$, He or $e$ and the $L_k$'s are determined from a fit of the following form:

$$\log_{10} L_k = \sum_{i=0}^{N} a_i^{(k)} \log_{10} T_3. \tag{4.34}$$

All fit coefficients $a_i$ are given in table B.2 of Appendix B.

At late times the intensity of the photon background is negligible, which is why we only considered ionization and excitation from collisions with matter and not with background photons. Moreover, all cooling rates given above are valid as long as the gas is optically thin, which is a good approximation in the primordial halos. If the density is too high, the emitted photons can't escape the gas and the energy loss is slowed down. In this approximation we can also ignore any heating process that would counter the cooling.

### 4.3.2 Chemical abundances

To compute the cooling rates and timescale, one must also specify the number density $n_i$ of each chemical species. In general, their relative abundances are determined by rate equations of the form [154]

$$\frac{dn_i}{dt} = \sum_{j \in F_i} \left( k_j \prod_{r \in R_j} n_r^{(j)} \right) - \sum_{j \in D_i} \left( k_j \prod_{r \in R_j} n_r^{(j)} \right), \tag{4.35}$$

where $F_i$ and $D_i$ are the sets of reactions $R_j$ that form and destroy the $i$th species and $n_r^j$ is the number density of each reactant in $R_j$. The coefficients $k_j$ set the rate of each reaction and usually depend on the temperature of the system. If the right-hand-side of eq. (4.35) vanishes for a given species, the reaction is in collisional equilibrium, or steady state. If all processes are two-body reactions, the steady-state density is given by

$$n_i = \frac{\sum_{j \in F_i} k_j n_1^{(j)} n_2^{(j)}}{\sum_{j \in D_i} k_j n_d^{(j)}}. \tag{4.36}$$

The cooling mechanisms depend on the abundances of eight chemical species: $H^0$, $H^+$, $H^-$, $H_2$, $He^0$, $He^+$, $He^{++}$ and $e^-$.[8] In the steady-state approximation, the network eq. (4.36) is usually underdetermined, but one can solve it if 1) the total nuclear density $n_N = n_{\rm H} + n_{\rm He}$ satisfies eq. (3.38); 2) the total He-H number ratio $X_{\rm He} = n_{\rm He}/n_{\rm H}$ satisfies eq. (3.35) (assuming nuclear reactions in stars do not strongly affect $X_{\rm He}$); 3) matter is neutral, which implies $n_e \simeq n_{\rm H^+} + n_{\rm He^+} + 2n_{\rm He^{++}}$ (since the density of $H^-$ is negligible). The reactions considered in our simplified chemical network and their rates are given in table B.3 of appendix B.

However, the steady-state approximation tends to break down at low temperature/densities: if the timescale of a given reaction $t_r \sim (k_r n)^{-1}$ is smaller than the dynamical timescale of the system, $t_{\rm dyn} \sim (G\rho)^{-1/2}$, the chemical species cannot reach collisional equilibrium. This is most likely to occur at early times in small halos with low density and temperature. At $z = 10$ the $t_{\rm dyn}$ corresponding to the virial overdensity is $\sim 0.2$ Gyr. Taking $n \sim 1$ cm$^{-3}$ — roughly the central density in halos at this epoch — we can check that $H_2$, $H^+$ and $He^+$ respectively come into collisional equilibrium at about 4,000 K, 9,000 K and 15,000 K. Below

[8] Reaction 11 in table B.3 produces $H_2^+$ but we did not consider any cooling mechanism associated with this ion. Since its abundance is negligible at all times we omit it from our analysis.

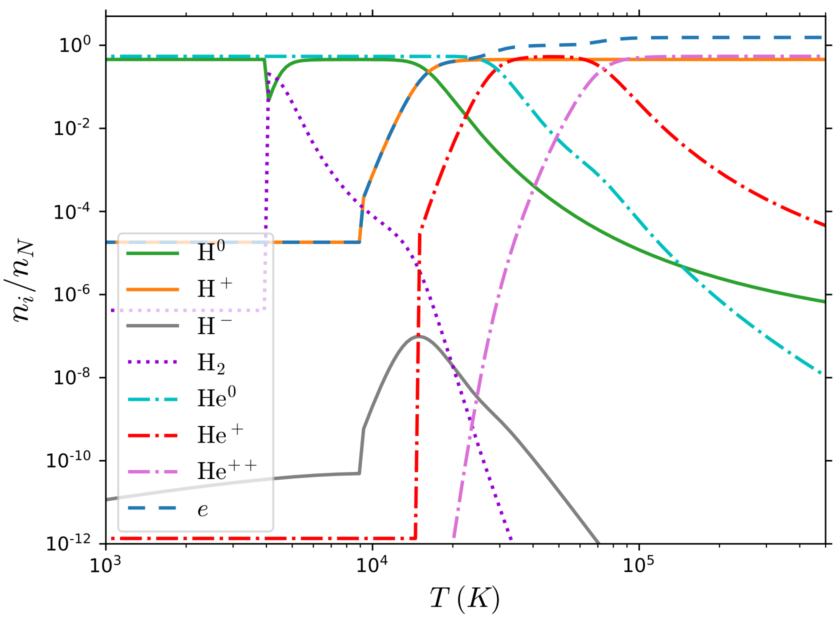


Figure 4.4: Example of the relative abundance of each chemical species $n_i/n_N$ at $z = 10$ as a function of the temperature of the gas. We used the benchmark parameters $x = 0.1$ and $\beta = 1$.

those critical temperatures we take the abundances of each species to be their relic densities after recombination, as determined by `Recfast++` (section 3.4).

In reality the chemical species evolve toward their equilibrium values during shock heating; the true densities therefore lie between the equilibrium and the freeze-out values, but this difference has a negligible impact on the cooling rates at high $z$, as well as on the overall evolution of the galaxy.[9] Figure 4.4 illustrates the evolution of each chemical species with the temperature at $z = 10$ with parameter $x = 0.1$ and $\beta = 1$. The abrupt transitions result from the approximations described here, and would be smoothed out by fully solving eqs. (4.35), but with no appreciable effect on the consequent formation of structure.

[9] $He^{++}$, which comes into equilibrium at $\sim 37{,}000$ K, is a special case since we do not solve for its relic density at recombination. Instead we take its steady-state value at all temperatures, which has no effct on the cooling rates since its abundance is negligible below 50 000 K. We do likewise for $H^-$ since its high destruction rate keeps its abundance small at all times [142].

## 4.4 Cloud collapse and star formation

As the hot gas cloud of mirror matter that fills the halo cools, its kinetic energy decreases and the virial condition $2K = -U$ is no longer satisfied. This will result in the collapse of the cloud [21]. The gas will also fragment since overdense regions have a higher potential energy and cool more efficiently, making them collapse at an earlier time.

If the cloud has a mass $M$, its kinetic energy is $K = 3MkT/2\mu$, where as in eq. (4.26) $\mu$ is the mean mass per molecule. Approximating the cloud as a homogeneous sphere of radius $R$ and density $\rho$, its potential energy is $U = -3GM^2/5R$. On can easily check that the collapse will take place ($2K < -U$) if $R > \lambda_J$, where the Jeans length is defined as[10] [21, 148]

$$\lambda_J = \sqrt{\frac{15kT}{4\pi G\mu\rho}}. \tag{4.37}$$

Below this scale the gas cannot collapse and fragment further. This sets the minimal mass of fragments that result from the collapse,

$$M_J = \frac{4\pi\rho}{3}\lambda_J^3. \tag{4.38}$$

This expression yields a rough estimate of the mass of primordial mirror matter stars if one knows the temperature and density at the end of the cloud collapse. Initially, if the cooling mechanism is very efficient, the collapse will occur on a characteristic timescale set by the free-fall time,

$$t_{\text{ff}}(r) = \sqrt{\frac{3\pi}{32G\rho_r}}. \tag{4.39}$$

In this expression $\rho_r$ is the average matter density inside a sphere of radius $r$. Near the end of the free-fall phase, the density of the cloud increases by many orders of magnitude very

[10] Another common definition for the Jeans length is $\lambda_J = c_s t_{\text{ff}}$, where $c_s \approx (5kT/3\mu)^{1/2}$ is the sound speed in a nonrelativistic monoatomic gas and $t_{\text{ff}}$ is given by eq. (4.39). With this definition, $\lambda_J$ is the maximum distance where waves can travel in the cloud and maintain an isothermal distribution before collapsing. This definition agrees with eq. (4.37) up to a constant of order unity.

rapidly while $T$ remains approximately constant [21]. Therefore, if the collapse is isothermal, the Jeans mass scales as

$$M_J \propto \rho^{-1/2} \quad \text{(isothermal collapse)}, \tag{4.40}$$

and decreases in time.

Once the cloud reaches a critical density, radiative processes become inefficient as the gas reabsorbs the emitted photons. In the optically thick limit where gas does not radiate its energy away, the temperature evolves adiabatically, $T \propto \rho^{\gamma-1}$, which in turn implies that $M_J$ increases:

$$M_J \propto \rho^{(3\gamma-4)/2} = \rho^{1/2} \quad \text{(adiabatic collapse)}, \tag{4.41}$$

where we used $\gamma = 5/3$.

Therefore, $M_J$ reaches a minimum somewhere between these two regimes, which corresponds roughly to the minimal mass of cloud fragments. To estimate at which point the collapse transitions between these two phases, we will follow ref. [109] which used `Krome` [154] to study the evolution of the temperature and the density of a collapsing cloud of mirror matter gas. `Krome` assumes the cloud is in a free fall,

$$\frac{\dot{n}}{n} \sim \frac{1}{t_{\rm ff}}, \tag{4.42}$$

and solves the out-of-equilibrium rate equations (4.35). The temperature evolves as [154]

$$\frac{\dot{T}}{T} = (\gamma - 1)\left(\frac{\dot{n}}{n} + \frac{\mathcal{H} - \mathcal{C}}{nkT}\right), \tag{4.43}$$

where the cooling rate is $\mathcal{C} = \sum_i \mathcal{C}_i$ and $\mathcal{H}$ is the heating rate. The heating rate is negligible in the optically thin limit because photons exit the cloud, but as the gas becomes denser we must include it in our calculations.

We focus on the cloud collapse inside the MW halo at $z = 10$, which according to the merger trees has an average mass $M \simeq 8 \times 10^8$ $\mathrm{M}_\odot$ and central density $n \sim 1$ cm$^{-3}$. It is assumed that the collapse can always happen, independently of $x$ and $\beta$, and that the fragments can cool to $\sim 10\,\%$ of $T_M$ (see eq. (4.26)) before collapsing. In section 4.5 we will verify the values of $(x, \beta)$ for which cooling is really efficient enough for the cloud to collapse. In such a case $T$ drops to values $\ll T_M$ before the density increases significantly. Then our assumptions are self-consistent and allow for estimating the mass of primordial stars independently of $\beta$; dependence on $x$ remains since it affects the chemical abundances.

Figure 4.5 (left) shows the evolution of the temperature from eq. (4.43) during the collapse for several values of $x$ and for the SM. It reveals that smaller values of $x$ lead to more efficient cooling, since more $H_2$ can form. Interestingly, even when the hydrogen fraction is small, $H_2$ cooling can reduce $T$ to $\sim$ few $\times$ 100 K very rapidly. We evaluated the Jeans mass at the minimum $T$ (near $n \sim 200$ cm$^{-3}$) to estimate the mass $M'_*$ ($M_*$) of the fragments in the MƧ (SM). After this point, the cloud collapses quasi-adiabatically and the rise of $T$ slows the decrease of the Jeans mass. This point allows us to set an upper limit on the final fragment mass $M'_*$ rather than evaluating it accurately, which is impossible in our simplified analysis. In reality, the angular momentum of the cloud becomes nonnegligible before then and the mass of the fragments is determined by criteria other than eq. (4.38) [21, 35].

Note that this oversimplification is not an issue, because we are only interested in the ratio $\zeta \equiv M'_*/M_*$ of the fragment mass in the MƧ and in the SM, which wouldn't change much if we evaluated eq. 4.38 at another point of the $(n, T)$ diagram. This ratio gives a rough approximation of how the mass of mirror stars scales compared to the visible ones, which allows us to estimate their lifetimes and their supernova feedback on structure formation. Figure 4.5 (right, blue curve) also illustrates the value of $\zeta$ for all values of $x$. It is apparent that $\zeta > 1$ for all values of $x$, indicative of the lower cooling efficiency in the MƧ (from suppressed H abundance) leading to less fragmentation of gas clouds.

We should emphasize that this estimate of $\zeta$ is only valid for primordial stars as we do not include any element heavier than He in our analysis. In reality, it is possible that the

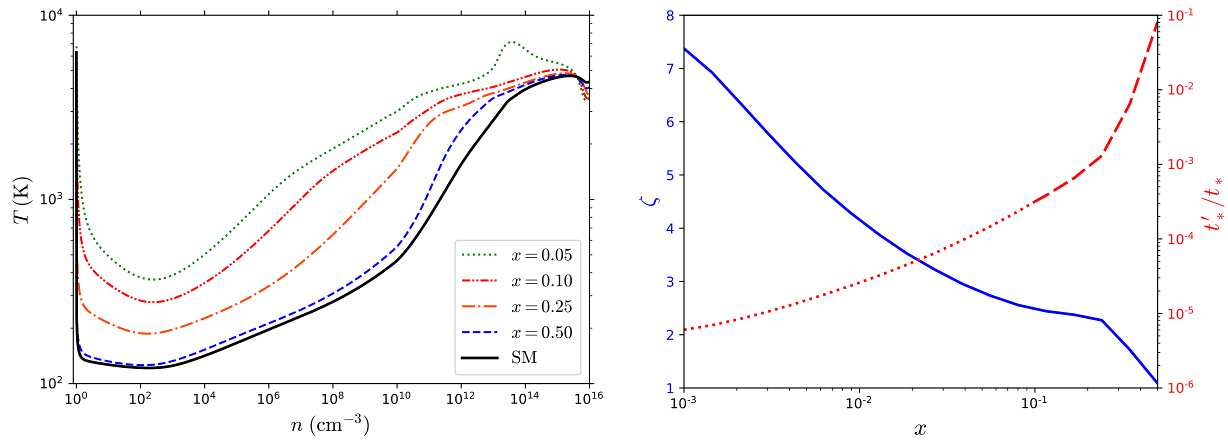


Figure 4.5: Left: Temperature evolution during the cloud collapse of a gas fragment at $z = 10$ in a Milky Way-like halo for values of $x$ increasing from top to bottom, including the SM ($x = 1, Y = 0.24$). Evaluating eq. (4.38) at the temperature minimum of each curve gives an estimate of the mass of primordial stars. Right: Ratio $\zeta$ of the minimal fragment mass in the MƧ relative to the SM (blue, solid) and ratio of the characteristic stellar lifetimes (red, dashed+dotted). The dotted curve illustrates the extrapolation of eq. (4.45) outside the fit interval of ref. [157].

short-lived He-dominated stars in the MƧ produce metals at a much higher rate than in the SM. Since metals are easier to ionize, their presence can significantly increase the cooling rate and the fragmentation inside a gas cloud [155, 158].

Unlike ordinary matter, mirror stars are usually He-dominated, which has important consequences for their evolution, notably their lifetime $t_*$. In the SM, the H-burning phase constitutes most of the lifetime of stars, with the post-main sequence evolution contributing only about 10 % of $t_*$ [21]. In the MƧ, with much less H to burn, stars quickly transition to the later stages of their evolution.

We note that the average mass for visible stars can be estimated using the initial mass function (IMF):

$$M_* = \int_{0.08\,M_\odot}^{100\,M_\odot} m\,\phi(m)\,dm \simeq 0.3\ M_\odot, \tag{4.44}$$

where $\phi(m) \propto m^{-2.35}$ is the Salpeter IMF [35, 159] normalized such that its integral over the mass range of stable stars ($0.08\ M_\odot < m < 100\ M_\odot$) is 1. Hence we take the characteristic stellar mass in the MƧ to be $M'_* = \zeta \times (0.3\ \mathrm{M}_\odot)$. Ref. [157] studied the dependence of $t_*$ on the He fraction and the mass of stars. Using their fit results, we estimate the scaling of typical lifetimes of MƧ stars by comparison to the SM:

$$\begin{aligned}\log_{10}\left(\frac{t'_*}{t_*}\right) &\simeq 0.74 - 2.86Y' - 0.94Y'^2 - 4.77\log_{10}\zeta + 0.99(\log_{10}\zeta)^2 \\ &\quad + 1.34Y'\log_{10}\zeta + 0.29Y'^2\log_{10}\zeta - 0.28Y'^2(\log_{10}\zeta)^2.\end{aligned} \tag{4.45}$$

The ratios $\zeta$ and $t'_*/t_*$ are plotted in figure 4.5 (right) as a function of $x$. $t'_*/t_*$ will be used to estimate the supernova feedback of MƧ stars on the formation of dark galactic structures in section 4.5.1. We note that eq. (4.45) is only valid up to $Y' = 0.8$ ($x \simeq 0.1$), so our estimate of the stellar lifetime for $x \lesssim 0.1$ is likely to be too small. However, in this range one nevertheless expects that $t'_*/t_* \ll 1$. In section 4.5.1 we will show that the main consequence of such short lifetimes is that supernova feedback favors star production over the formation of cold gas clouds in the mirror galactic disk, whereas in section 5.1 we show that star formation is already maximally efficient at $x = 0.1$; hence our results are not sensitive to the precise value of $t'_*/t_*$ at lower temperatures, and it is safe to use eq. (4.45) for $Y' > 0.8$.

## 4.5 Galaxy formation

We now have the necessary ingredients to study the formation of a dark galaxy. We will use the semi-analytical model GALFORM introduced in [147]. The steps to be carried out for implementing it are described as follows.

The MƧ matter is divided into three components: the hot gas component, the spheroidal bulge fraction and the disk fraction. The bulge and the disk together form the MƧ galaxy. The disk fraction is further subdivided into two components: active stars and cold gas clouds. Star formation is highly suppressed in the bulge so such a subdivision is not needed there. The remaining matter component is CDM. Visible baryons are omitted from our analysis for simplicity and since GALFORM is not set up to properly account for their gravitational interaction with the MƧ.[11] Instead, we include the visible baryons into the CDM fraction, so that $\Omega_m = \Omega_c + \Omega_{b'}$.

### 4.5.1 Disk formation

The GALFORM algorithm simulates structure formation beginning at redshift $z = 10$, taking as input the merger trees described above, and evolving forward in time using logarithmically spaced time steps $\Delta t$. Halo evolution is simulated semi-analytically until the present, $z = 0$. The lifetime of the halo $t_{\text{halo}}$ is defined to be the time it takes to double in mass, whether by matter accretion or by mergers.

The halo is modeled using spherical shells plus a disk component. At the end of each time step, two characteristic radii must be computed: the cooling radius $r_{\text{cool}}$ and the free-fall radius $r_{\text{ff}}$. These are respectively the maximal distances such that the cooling timescale $t_{\text{cool}}$ (eq. (4.27)) and the free-fall timescale (eq. (4.39)) are smaller than the elapsed time since the beginning of the halo's lifetime. Hence the radius $r_{\text{acc}} = \min(r_{\text{cool}}, r_{\text{ff}})$ is the maximum distance to which the gas has had time to cool down and accrete into compact objects.

The values of $r_{\text{acc}}$ before and after the time step $\Delta t$ delimit a spherical shell of width $\Delta r_{\text{acc}}$ that contains mass $\Delta M_{\text{acc}}$ of hot mirror matter gas. As shown in appendix B of ref. [147], this accreted matter determines how the masses of the hot gas $M_{\text{hot}}$ and the disk

[11]The only impact of SM particles in our analysis would be to potentially shorten the free-fall timescale, eq. (4.39) by collapsing and changing the total matter distribution in the halo. First, since visible baryons only represent about 15 % of the total matter content, their impact on $t_{\text{ff}}$ is small. Secondly, structure formation in the MƧ also equally depends on the cooling timescale, eq. (4.27), which is independent of the SM matter.

$M_{\rm disk}$ change during that time step:

$$\Delta M_{\rm disk} = \Delta M_{\rm cold} + \Delta M_{*}, \tag{4.46}$$

$$\begin{aligned}\Delta M_{\star} = {}& M^0_{\rm cold}\frac{1-R}{1-R+B}\left[1-e^{-\Delta t/\tau_{\rm eff}}\right]\\ &-\Delta M_{\rm acc}\frac{\tau_{\rm eff}}{\Delta t}\frac{1-R}{1-R+B}\left[1-\frac{\Delta t}{\tau_{\rm eff}}-e^{-\Delta t/\tau_{\rm eff}}\right],\end{aligned} \tag{4.47}$$

$$\Delta M_{\rm cold} = \Delta M_{\rm acc} - \frac{1-R+B}{1-R}\Delta M_{\star}, \tag{4.48}$$

$$\Delta M_{\rm hot} = -\Delta M_{\rm acc} + \frac{B}{1-R}\Delta M_{\star}. \tag{4.49}$$

Here $M_{\rm cold}$ and $M_*$ are the masses of the cold gas and stellar components of the disk, and $M^0_{\rm cold}$ is the cold gas mass at the beginning of the time step. $R$ is the fraction of mass recycled by stars (*e.g.*, stellar winds that contribute to the cold gas component of the disk) and $B$ parametrizes the efficiency of the supernova feedback that heats the cold gas fraction.

The effective mirror star formation timescale is $\tau_{\rm eff} = \tau'_*/(1-R+B)$. To determine $\tau'_*$, one can assume that the star formation rate is in equilibrium with the stellar death rate (the inverse of the average stellar lifetime). Then the ratio of star formation timescales $\tau'_*/\tau_*$ in the MƧ and in the SM is equal to the ratio of the characteristic stellar lifetimes $t'_*/t_*$ given by eq. (4.45),

$$\tau'_* \simeq \left(\frac{t'_*}{t_*}\right)\tau_* = 200\frac{r_D}{V_D}\left(\frac{t'_*}{t_*}\right)\left(\frac{V_D}{200\ \text{km/s}}\right)^{-1.5}. \tag{4.50}$$

Following ref. [147], we take $R = 0.31$ and $B = (V_{\rm D}/(200\ \text{km/s}))^{-2}$, where $V_{\rm D} = (GM_{r_D}/r_D)^{1/2}$ is the circular velocity at the half-mass radius $r_D$ of the galactic disk. Assuming the disk has an exponential surface density, its half-mass radius can be estimated as $r_D = 1.19\lambda_H r_{\rm acc}$ where $\lambda_H$ is a spin parameter that follows a log-normal distribution with average value $\lambda_H = 0.039$, that we adopt for simplicity.

The evolution of the disk and the hot gas mass fractions is found by iterating eqs. (4.46-

4.49). During the characteristic time $t_{\rm halo}$, the temperature $T_M$ of the hot mirror matter gas is assumed to remain at its initial value, eq. (4.26), and likewise for the relative abundances of each chemical species and the core radius $r_0$ of the hot gas density profile. All of these quantities are updated at the beginning of each stage of evolution spanning time $t_{\rm halo}$, for all the active halos of the merger tree.

### 4.5.2 Galaxy mergers and bulge formation

Eventually, every halo in the merger tree combines with another halo, the smaller of the two becoming a satellite of the larger one. We assume that all the hot gas of the satellite halo is stripped by hydrodynamic drag, so that its disk and bulge fractions no longer evolve. After this the satellite orbits the main halo until they merge, over the characteristic timescale

$$\tau_{\rm mrg} = \Theta_{\rm orbit}\frac{\pi r_{\rm vir}}{V_H}\frac{0.3722}{\ln(M_H/M_{\rm sat})}\frac{M_H}{M_{\rm sat}}. \tag{4.51}$$

Here $V_H = (GM_H/r_{\rm vir})^{1/2}$ is the circular velocity at the virial radius, $M_{\rm sat}$ is the total mass of the satellite halo (mirror baryons and CDM) and $M_H$ is the total mass of the main halo, including all the satellite halos. $\Theta_{\rm orbit}$ is a parameter that depends on the orbit of the satellite. It is characterized by a random log-normal distribution with an average $\langle\log_{10}\Theta_{\rm orbit}\rangle = -0.14$ and a standard deviation $\sigma_{\log\Theta} = 0.26$.

The outcome of a galaxy merger depends on the mass ratio of the two galaxies (disk and bulge components only), $M_{\rm gal}^{\rm sat}/M_{\rm gal}^{\rm cen}$. If this ratio is smaller than a critical value $f_{\rm crit}$, the merger is "minor:" the satellite galaxy is disrupted, its bulge and stellar components are added to the bulge fraction of the central galaxy, and the cold gas falls into the central disk. If the mass ratio is greater than $f_{\rm crit}$, the merger is "major," in which case both galaxies are disrupted by dynamical friction and all the mirror matter ends up in a spheroidal bulge. We take $f_{\rm crit} = 0.3$, the lowest possible value in agreement with numerical studies [147], but it has been argued in ref. [148] that larger values do not change the results significantly.

In a minor merger, the cold gas of the satellite galaxy is added to the main galactic disk, which changes its half-mass radius $r_D$. The new radius is determined by the conservation of angular momentum, $\mathbf{j_{D'}} = \mathbf{j_{D1}} + \mathbf{j_{D2}}$, where $|\mathbf{j_D}| = 2r_D V_H/1.68$. Squaring and averaging over the relative orientation of the two galaxies ($\langle \mathbf{j_{D1}} \cdot \mathbf{j_{D2}} \rangle = 0$) yields

$$r_{D'} = \frac{r_{D1} M_{D1} + r_{D2} M_{D2}}{M_{D1} + M_{D2}}, \tag{4.52}$$

that is, the new radius is the weighted average of the two initial radii. The bulge component is expected to have a de Vaucouleurs density profile, $\log \rho_{\text{bulge}} \sim -r^{1/4}$, but we find that it can be more simply modeled as a sphere of uniform density and radius $r_D/2$, without significantly changing the final results.

By iterating over all halos and evolving until $z = 0$, the procedure described in the previous sections allows us to predict the fraction of mirror matter that forms galactic structures (either a disk or a bulge) and the fraction that remains in a hot gas cloud. We present our results in the following chapter.

# Chapter 5

# Results and experimental constraints

We simulated galaxy evolution in 10 different merger trees for $18^2$ combinations of $(x, \beta)$ in the range $10^{-3} < x < 0.5$ and $10^{-3} < \beta < 5$ and averaged over the final fractions. Smaller values of $\beta$ cannot be constrained with present data given the current experimental sensitivity to a very subdominant component of MƧ dark matter. Similarly, for $x < 10^{-3}$ the helium mass fraction is saturated ($Y' \sim 0.99$) and the chemical evolution of the MƧ gas cannot be distinguished from that at $x = 10^{-3}$. In this chapter, we will use these predictions in conjunction with astronomical data to constrain the parameters of the model. This chapter covers the material in section IV of ref. [19], the paper written by the author of this thesis.

## 5.1 Galactic distribution of mirror matter

The results of our MƧ structure formation analysis are shown in figure 5.1, where the fractions of the different components $f_{\rm gas}$, $f_{\rm disk}$, $f_{\rm bulge}$, $f_{\rm sat}$ and $f_*$ (the fraction in stars in the disk) are plotted as functions of $(x, \beta)$. One of the most striking features is that for much of the parameter space ($x \lesssim 0.1$, $\beta \lesssim 1$), over 90 % of mirror matter is in a hot gas cloud and does not condense to form structures in the halo. This is readily understood, since the low density and low hydrogen abundance lead to inefficient cooling, maintaining high pressure in the gas cloud and preventing it from collapsing. Our results show that at low $x$ and in the range

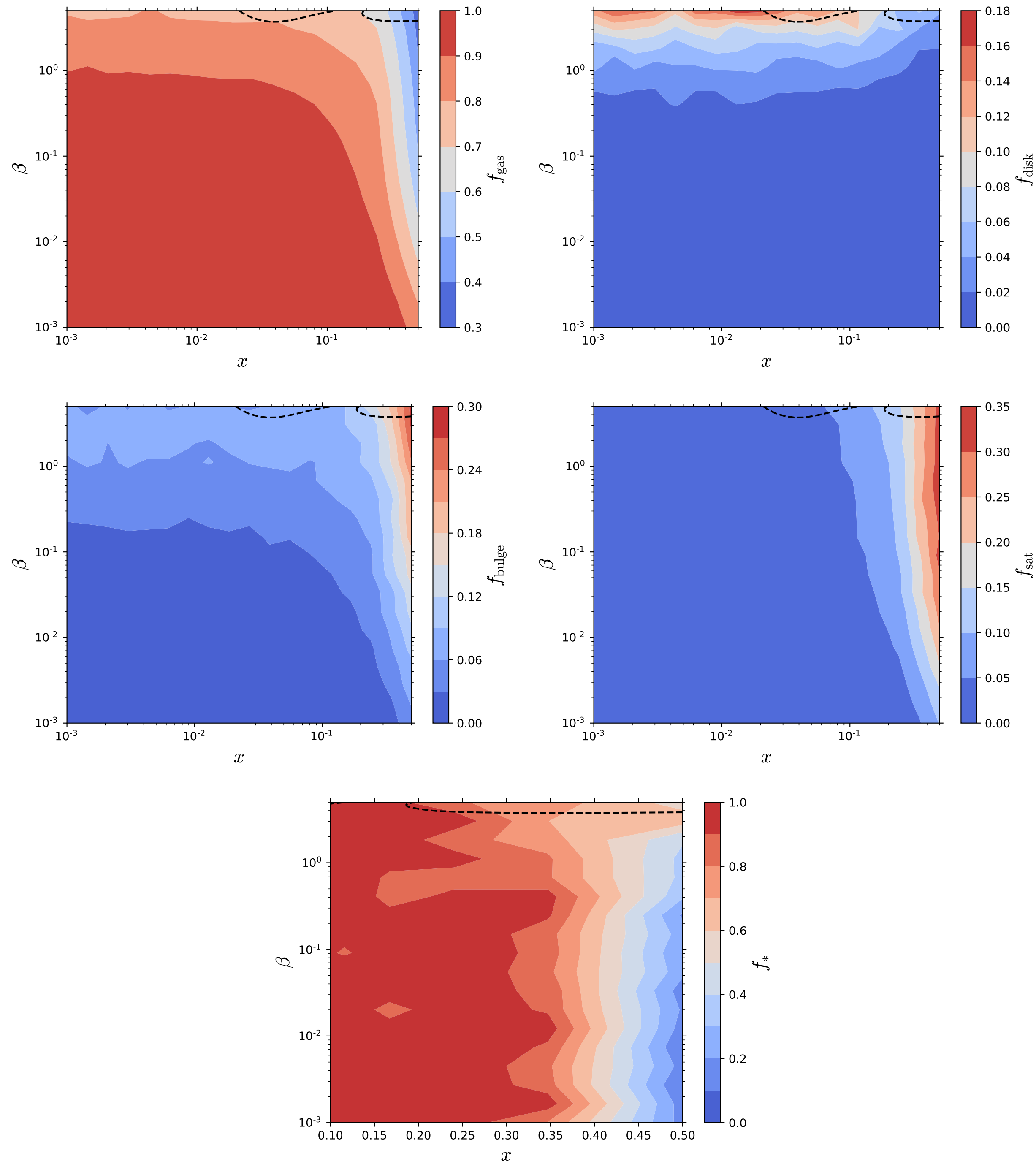


Figure 5.1: Results of the mirror structure formation analysis. The top four panels show the average fraction of mirror particles in each galactic structure (hot gas, disk, bulge and satellite galaxies) in a $10^{12}\ M_\odot$ halo such that $f_{\text{gas}} + f_{\text{disk}} + f_{\text{bulge}} + f_{\text{sat}} = 1$. The bottom panel shows the fraction of stars $f_*$ in the mirror galactic disk. The fraction of cold gas in the disk is given by $f_{\text{cold}} = 1 - f_*$. The regions above the dashed curves are excluded from our analysis due to the self-consistency check discussed in section 4.2.

$0.5 \lesssim \beta \lesssim 1$ about 5–10 % of the MƧ forms a dark galaxy. In this case, even if the dark galaxy is subdominant in the halo, the mirror stars and supernovae within it would amplify the baryonic effects of SM particles, which have been argued to significantly alleviate the small-scale tension of CDM [80, 81].

For MƧ densities $\beta \lesssim 0.5$, mirror matter behaves similarly to generic models of dissipative DM, such as atomic DM, that have no nuclear or chemical reactions and do not collapse into compact objects. Although the MƧ would constitute only a small fraction of DM and would not lead to dark stuctures (stars, planets, life forms), it could still have interesting cosmological effects, like the suppression of the matter power spectrum on small scales. The mirror gas cloud would also have a cored density profile, resulting in a shallower gravitational potential in the center of the halo than in a pure CDM scenario, possibly ameliorating the cusp-core problem.

The disk fraction $f_{\rm disk}$ depends much more strongly on $\beta$ than on $x$. This comes about because the long lifetime of the main halo allows for the formation of a mirror galaxy at sufficiently high density, even though cooling is less efficient at small $x$ (due to the low hydrogen fraction). The fraction $f_{\rm sat}$ of mirror matter in satellite galaxies behaves differently: even at large mirror particles densities, for $x < 0.1$ the cooling timescale becomes longer than the lifetime of subhalos merging with the MW, leaving too little time for structures to form. Hence dwarf galaxies orbiting the MW will host few mirror particles if $x < 0.1$. It is likely however that we underestimate $f_{\rm sat}$ due to our assumption that galaxy formation ended once the subhalos merged with the main halo. In reality the satellite galaxies can accrete cooling gas from the main halo and continue to grow after a merger.

There is a clear correlation between $f_{\rm bulge}$ and the sum of $f_{\rm disk}$ and $f_{\rm sat}$, which arises because bulge formation requires both the main halo and the satellite subhalos to form, before the latter are disrupted by dynamical friction. The absence of a disk for $x \gtrsim 0.1$, where $f_{\rm bulge}$ is at its maximum, indicates that a major merger destroyed the disk of the central halo. That major merger is probably recent, otherwise the disk would have had time to form again. Similarly, we can understand the small bulge fraction in the region $\beta \gtrsim 0.2$, $x \lesssim 0.1$ as resulting from a series of minor mergers or an early-time major merger, since there is a significant disk fraction at $z = 0$ for these parameters.

The bottom panel of figure 5.1 shows the effect of the shortened stellar lifetime in the MƧ (see eqs. (4.45) and (4.50)). The high He abundance and the larger mass of primordial stars increase the stellar feedback from supernovae to a point where most of the cold molecular clouds are rapidly heated and return to the hot fraction of the halo, leaving mirror stars as the only inhabitants of the mirror galaxy.

## 5.2 Astronomical constraints

We now consider various astronomical constraints on MƧ galactic structures. The excluded regions lie above the curves shown in figure 5.2. The limits on disk surface density, bulge and total stellar mass, and from gravitational lensing surveys, are described in the following subsections.

### 5.2.1 Thin disk surface density

Data from Gaia DR2 allowed ref. [160] to constrain the surface density $\Sigma_D$ of a thin dark disk in the vicinity of the Sun. The gravitational potential in the presence of a DM disk would be deeper, leading to greater acceleration towards the galactic plane than what ordinary stars can account for. This affects the transverse velocities and density distribution of nearby stars. Assuming that the dark disk possesses an exponential profile and a scale height $h_D \simeq 10$ pc (which could explain phenomena like the periodicity of comet impacts [161, 162]), the 95 % C.L. bound on its local surface density is

$$\Sigma_D(R_\odot) = \frac{M_D}{2\pi L_D^2} e^{-R_\odot/L_D} \lesssim 4.15 \ \frac{M_\odot}{\mathrm{pc}^2}, \tag{5.1}$$

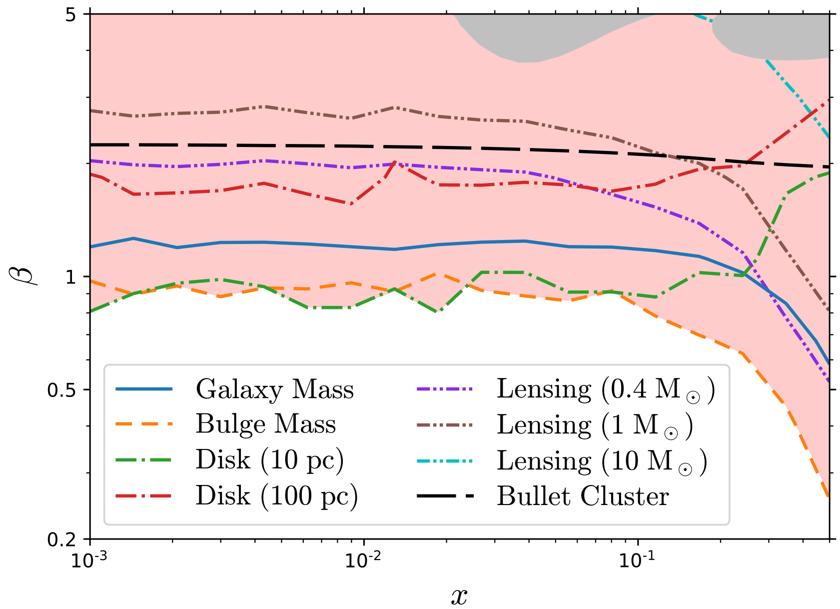


Figure 5.2: Upper limits for M2 model from constraints on: the total mass of the galaxy (defined as bulge plus disk, solid curve); the bulge mass (dashed); the thin disk surface density (dot-dashed), assuming $h_D = 10$ (green) or 100 pc (red) for the dark disk; gravitational lensing events (double-dot-dashed) for $m_{\rm mac} = 0.4$ (violet), 1 (brown) or 10 (cyan) $M_\odot$; and the Bullet Cluster (long-dashed). The red shaded area is excluded, while the grey regions lie outside the validity of our analysis (see section 4.2).

where $R_\odot = 8.1$ kpc is the distance of the Sun from the center of the galaxy and $L_D$ is the scale length of the disk. The scale length is related to the half-mass radius $r_D$, which we included in our analysis, as $r_D/L_D \simeq 1.68$.

The constraint (5.1) led ref. [160] to conclude that a dissipative dark sector can constitute less than 1 % of the total DM. However a more conservative interpretation is that less than 1 % of the DM *has accreted into a thin dark disk*; in that case the dissipative dark sector could be more abundant since we expect only a fraction of it to form a galactic disk, $\lesssim 20\,\%$ for mirror matter, as shown in figure 5.1.

Assuming a thin disk with scale height $h_D = 10\,$pc, this bound rules out the region $\beta \gtrsim 1$, except for $x \gtrsim 0.25$ where it is relaxed to $\beta \gtrsim 1.8$. For a thicker disk with $h_D = 100\,$pc, closer to the height of the visible disk, the constraint is relaxed to $\Sigma_D(R_\odot) \lesssim 12.9\ M_\odot/\mathrm{pc}^2$, loosening the bound on $\beta$ by a factor of $\sim 2$.

An underlying assumption is that the dark disk lies withing the MW plane. Although the two disks need not be initially aligned, one expects their gravitational attraction to do so on the dynamical timescale of the inner region of the halo, $t_{\rm dyn} \sim 1/\sqrt{G\rho} \sim \sqrt{L_D^3/GM_D}$. Even if the dark disk has a negligible density such that only the visible disk contributes to $t_{\rm dyn}$ ($M_D \sim 10^{10}\ M_\odot$, $L_D \sim 2.5$ kpc), one finds $t_{\rm dyn} \sim 20\,\rm Myr$, much shorter than the lifetime of the halo. Hence in all cases the two disks should be coincident.

### 5.2.2 Bulge and total stellar mass

Data from Gaia DR2 further enabled ref. [163] to determine the total mass of each component of the MW halo by fitting the rotation curves of nearby stars and using other kinematic data. They determined the mass of the galaxy (disk and bulge components combined) to be $4.99^{+0.34}_{-0.50} \times 10^{10}\ M_\odot$ in a $1.12 \times 10^{12}\ M_\odot$ halo. Scaling down their result to coincide with our $10^{12}\ M_\odot$ halo, the total mass of the galactic components in our simulation should be $M_{\rm gal} = 4.46^{+0.30}_{-0.45} \times 10^{10}\ M_\odot$.

Since this measurement was obtained from stellar dynamics only, it is sensitive to the presence of a mirror galactic component. However it is difficult to accurately estimate the contribution of ordinary baryons to the MW mass from the mass-luminosity relation. It is believed that about 20 % of the baryons in the halo should condense into compact structures in the galaxy (see [164] and references therein), which represents a visible matter contribution of $3.1 \times 10^{10}\ M_\odot$. This leaves room for the remainder to come from a mirror galaxy component.[12]

Under this assumption, we derive a $2\sigma$ upper bound on the mass of the mirror galaxy (disk plus bulge),

$$M'_{\rm gal} \lesssim 2 \times 10^{10}\ M_\odot. \tag{5.2}$$

[12]The fraction of condensed baryons fluctuates by a factor of $\sim 1.5$ from galaxy to galaxy, which is consistent with the disk + bulge components of our halo containing only ordinary baryons.

It is also possible to constrain the bulge mass of the MW separately. Ref. [163] determined $M_{\rm bulge} = 0.93^{+0.9}_{-0.8} \times 10^{10}\ M_\odot$ using Gaia DR2, in agreement with the value of ref. [165] obtained from rotation curves. A larger value was derived using photometric data from the VVV survey, estimating the contribution from visible stars to the bulge mass as $M^{\rm SM}_{\rm bulge} = 2.0 \pm 0.3 \times 10^{10}\ M_\odot$ [166, 167]. Combining errors in quadrature, these imply the $2\sigma$ upper bound on the MƧ contribution

$$M'_{\rm bulge} = M_{\rm bulge} - M^{\rm SM}_{\rm bulge} \lesssim 0.83 \times 10^{10}\ M_\odot\,. \tag{5.3}$$

Both (5.2) and (5.3) imply limits comparable to that from the dark disk surface density, excluding $\beta \gtrsim 1$ for any $x$. Due to the increased bulge fraction at large $x$, the bound on $M'_{\rm bulge}$ becomes tighter at large $x$, ruling out $\beta \gtrsim 0.3$ at $x \simeq 0.5$.

We note that this method cannot be used to constrain the mass of the dark disk alone since luminosity data don't allow for an accurate measurement of the total mass of the MW disk $M_{\rm disk}$ due to the optical thickness of the galactic plane. The only constraint we can obtain from the disk is an upper bound on the surface density in the vicinity of the Sun, *cf.* section 5.2.1.

### 5.2.3 Gravitational lensing

Compact objects made of mirror matter could be detected through their gravitational lensing of distant stars, similar to more general "MACHO" models of DM. However, it is difficult to predict the microlensing rate from MƧ structures since it depends strongly on their masses. Like in the SM, these compact objects could include asteroids and comets, planets, molecular clouds, or stars and dense globular clusters, spanning over 15 orders of magnitude in mass. We will focus on compact objects of mass $10^{-1}\ M_\odot \lesssim m_{\rm mac} \lesssim 10\ M_\odot$, corresponding to a main-sequence star or a small molecular cloud. As in the SM, smaller objects should represent a negligible fraction of the collapsed matter in the MƧ.

Constraints on the MACHO fraction $f_{\rm mac}$ of DM in this mass range have been discrepant. The MACHO collaboration studied microlensing events towards the Large Magellanic Cloud (LMC) and initially reported evidence that MACHOs of mass 0.15–0.9 $M_\odot$ comprise 8–50 % of the total halo DM [168], but it was later found that their dataset was contaminated by variable stars [169]. The same survey showed no evidence for MACHOs in the mass range 0.3–30 $M_\odot$ [170]. The EROS and OGLE surveys found no evidence for MACHOs towards the LMC [171–174] leading them to place an upper limit $f_{\rm mac} \lesssim 7$–30 %. The MEGA and POINT-AGAPE experiments came to different conclusions, the former finding no evidence for MACHOs towards M31 [175] while the latter reported $0.2 \lesssim f_{\rm mac} \lesssim 0.9$ [176].

To interpret these results we review some of the theory underlying MACHO searches [23, 173]. Gravitational lensing is characterized by an optical depth

$$\tau = \frac{4\pi G D_s^2}{c^2} \int_0^1 \rho(x)\, x(1-x)\, dx, \tag{5.4}$$

where $D_s$ is the distance to the amplified star and the integral is taken along the line of sight, with $x$ in units of $D_s$. The optical depth is the instantaneous probability that a star's brightness is amplified by a factor of at least 1.34, and is proportional to the mass density $\rho$ of the lens.

If $N_{\rm s}$ stars are monitored during a period $T_{\rm obs}$, then the expected number of detected microlensing events is

$$N_{\rm ex} = \frac{2}{\pi} \frac{T_{\rm obs}}{\langle t_E \rangle} \tau N_{\rm s} \langle \epsilon \rangle, \tag{5.5}$$

where $\langle t_E \rangle$ is the average Einstein radius crossing time and $\langle \epsilon \rangle$ is an efficiency coefficient that depends on the experimental selection criteria.

All the constraints cited above assumed that the MACHOs have an isothermal density profile $\rho \sim (r^2 + r_0^2)^{-1}$, which is often referred to as the "S model." This assumption is not valid for mirror matter compact objects since they are preferentially distributed in the disk and the bulge of galaxies, like visible stars. Ref. [168] estimated the total optical depth due to visible stars in the MW and the LMC galaxies as $\tau \simeq 2.4 \times 10^{-8}$ with an average Einstein radius crossing time $\langle t_E \rangle \simeq 60$ days.

The optical depth $\tau'$ due to a mirror galaxy is roughly proportional to its mass; we can therefore estimate it as $\tau' \simeq \tau\beta \times (f_{\rm mac}/0.2)$, where $f_{\rm mac} = f_{\rm disk} + f_{\rm bulge} + f_{\rm sat}$ is the fraction of mirror particles that form compact objects in both the MW and its satellite galaxies. The factor of 0.2 comes from the estimate that $\sim 20\,\%$ of the SM baryons in the halo end up in stars [164]. In reality the contribution from each component weighs differently in the value of $\tau$: MACHOs in the LMC are about twice as likely to produce a lensing event as one located in the MW bulge or disk. To be more precise we should sum the optical depth $\tau_i' \simeq \tau_i(M_i'/M_i)$ of each component, where $M_i$ ($M_i'$) is the mass of ordinary (mirror) stars in the LMC or in the MW bulge or disk. But the stellar masses of the LMC and of the individual MW components have large uncertainties and our simple treatment of satellite galaxies does not allow for an accurate identification of an LMC-like subhalo and the mass of its mirror galaxy. We can nevertheless make an order-of-magnitude estimate of $\tau'$ by putting all contributions on an equal footing and using the global fraction $f_{\rm mac}$ of condensed objects in the halo.

Since the Einstein radius is proportional to the square root of the mass of the lens [173], the value of $\langle t_E \rangle$ can also be different in the MƧ. Assuming a fiducial mass of $0.4\,M_\odot$ for SM stars, then we can approximate $\langle t_E' \rangle = \langle t_E \rangle \sqrt{m_{\rm mac}/0.4\,M_\odot}$, where $m_{\rm mac}$ is the mirror MACHO mass.

The EROS-2 survey sets one of the most stringent limit on MACHOs in the direction of the LMC [173]. During $T_{\rm obs} = 2500$ days, it monitored $N_{\rm s} = 5.5 \times 10^6$ stars and detected no microlensing event. This sets the 95 % confidence limit $N_{\rm ex} < 3$. From visible stars alone we expect $N_{\rm ex} \simeq 1.23$ events for an efficiency coefficient $\langle \epsilon \rangle \approx 0.35$. Then the limit on events from mirror stars is $N_{\rm ex}' \lesssim 1.77$, giving

$$\beta f_{\rm mac} \lesssim 0.29 \left( \frac{0.35}{\langle \epsilon' \rangle} \right) \sqrt{\frac{m_{\rm mac}}{0.4 M_\odot}}\,, \tag{5.6}$$

where $\langle \epsilon' \rangle$ is the efficiency coefficient of the MƧ, which could differ from the SM value if the MACHO mass is different. We will consider three benchmark values of $m_{\rm mac}$ to constrain our model: 0.4 $M_\odot$, 1 $M_\odot$ and 10 $M_\odot$. For simplicity we will also assume $\langle \epsilon' \rangle \approx 0.35$ for all masses.

The constraint (5.6) is not very restrictive, despite mirror matter being in principle capable of forming roughly as many compact objects as visible matter. If mirror stars had a mass distribution similar to visible stars, then $m_{\rm mac} \simeq 0.4\ M_\odot$ would only rule out $\beta \gtrsim 2$, which is already excluded by other observations. It is possible that the typical MƧ MACHO mass exceeds that of SM stars since cooling and cloud fragmentation are less efficient in the MƧ, as we argued in section 4.4. In that case the bound would be relaxed even more. A full analysis of the stellar evolution in the MƧ, including heavier elements that we have not included, would be required to estimate $m_{\rm mac}$ and the microlensing rate more accurately. But based on the present analysis, it seems unlikely that MACHO detection towards the LMC could be more constraining than the disk surface density or the stellar mass in the MW.

### 5.2.4 Bullet Cluster

Interestingly, the Bullet Cluster allows us to set an upper limit on the hot gas fraction of mirror baryons, that is, the absence of structure formation in the MƧ. The visible galaxies and stars on the scale of this cluster are essentially collisionless, but the hot gaseous baryons that surround the galaxies were slowed down by dynamical friction and stripped from their hosts. Similarly, mirror galaxies and stars pass through each other unimpeded, just like CDM, while the hot clouds of mirror baryons will self-interact.

The most stringent constraint on DM comes from the survival of the smaller subcluster in the merger, as less than 30 % of its mass inside a radius of 150 kpc was stripped in the collision [25]. As mentioned in chapter 2, this normally yields a bound on the integrated cross section $\sigma/m$. Here we instead follow the approach of ref. [17], constraining the distribution of mirror matter, in particular the mass of the hot gas fraction. We recapitulate the argument as follows.

Consider the elastic collision of two equal-mass mirror particles in the subcluster's reference frame. The incoming particles from the main cluster have an initial velocity $v_0 \approx 4800$ km/s. After the collision, they scatter with velocities

$$v_1 = v_0 \cos\Theta, \quad v_2 = v_0 \sin\Theta, \tag{5.7}$$

where $\Theta$ is the scattering angle of the incoming particle in the subcluster's frame.

For the subcluster to lose mass, both particles must be ejected from the halo: $v_1, v_2 > v_{\rm esc}$ where $v_{\rm esc} \approx 1200$ km/s is the escape velocity. This happens for a scattering angle $\theta$ (in the CM frame)

$$\frac{v_{\rm esc}}{v_0} < \sin\frac{\theta}{2} < \sqrt{1 - \left(\frac{v_{\rm esc}}{v_0}\right)^2}. \tag{5.8}$$

The scattering angles in the two frames are related by $\Theta = \theta/2$ for equal-mass particles. The evaporation rate is $R = N^{-1}dN/dt$ where $N$ is the total number of hot mirror particles in the subcluster. It can be expressed as [27]

$$R = n_2 v_0 \int_{\rm esc} \frac{d\sigma}{d\Omega_{CM}} d\Omega_{CM}, \tag{5.9}$$

where $n_2$ is the number density of mirror particles in the main cluster and the bounds of the integral are given by eq. (5.8). Integrating (5.9) over the crossing time $t = w/v_0$, where $w$ is the width of the main cluster, leads to the fraction of evaporated hot mirror particles,

$$\frac{\Delta N}{N} = 1 - \exp\left(-\frac{\Sigma_2}{m_N}\int_{esc}\frac{d\sigma}{d\Omega_{CM}} d\Omega_{CM}\right), \tag{5.10}$$

where $\Sigma_2$ is the surface density of the hot mirror matter gas in the main cluster. Taking the total DM surface density to be $\Sigma_{\rm DM} \simeq 0.3\,{\rm g/cm^2}$, we can estimate $\Sigma_2 \simeq f_{\rm gas}^{\rm BC}(\Omega_{b'}/\Omega_{\rm DM})\Sigma_{\rm DM}$, where $f_{\rm gas}^{\rm BC}$ is the hot mirror matter gas fraction in the main cluster.

Because of the large mass of the cluster and the subcluster ($M \gtrsim 2 \times 10^{14}\, M_\odot$), the virial temperature of the mirror matter gas is high enough to fully ionize the H and He atoms. Mass evaporation therefore proceeds via Rutherford scattering between ions. Assuming that all mirror nuclei have a mass $\overline{m_N}$ and a charge $Z = 1 + f_{\rm He}$ (see eqs. (3.36,3.37)), their differential cross section in the CM frame is

$$\frac{d\sigma}{d\Omega_{CM}} = \left(\frac{Z^2\alpha}{4E\sin^2(\theta/2)}\right)^2. \tag{5.11}$$

where $E = \overline{m_N}(v_0/2)^2$ is the total kinetic energy in the CM frame. Plugging this in eq. (5.10) and evaluating the integral within the bounds of eq. (5.8) yields

$$\frac{\Delta N}{N} = 1 - \exp\left\{\frac{-4\pi Z^4\alpha^2\Sigma_2}{\overline{m_N}^3 v_0^4}\frac{1-2\left(v_{esc}/v_0\right)^2}{\left(v_{esc}/v_0\right)^2\left(1-\left(v_{esc}/v_0\right)^2\right)}\right\}. \tag{5.12}$$

Assuming that only hot mirror particles are stripped in the collision, the constraint on the evaporated mass fraction of the subcluster is:

$$f_{\rm evap} = \frac{f_{\rm gas}^{\rm BC}\beta\Omega_b}{\Omega_{\rm DM}}\frac{\Delta N}{N} < 0.3. \tag{5.13}$$

This does not apply directly to our study, since we specifically studied structure formation in a $10^{12}\ M_\odot$ halo, while the Bullet subcluster has mass $\sim 2 \times 10^{14}\ M_\odot$. However ref. [164] indicates that the stellar mass fraction in a Bullet subcluster-sized halo is $\sim 10\,\%$ of the same fraction in a MW-like halo. We can therefore estimate the hot gas fraction of M$\mathbb{S}$ matter in the Bullet Cluster as $f_{\rm gas}^{\rm BC} \simeq (1 - 0.1 f_{\rm mac})$ (recall that $f_{\rm mac}$ is the fraction of mirror matter compact objects in the central galaxy and its satellites, that we derived above). However this is weaker than the kinematic data limits, and the resulting bound from the Bullet Cluster is similar in strength to that from microlensing, excluding only the region $\beta \gtrsim 2$.

## 5.3 Outlook

In this section we describe other astronomical observations that could lead to new constraints on the MƧ in the next few years, as more data is collected and experimental sensitivity increases.

Gravitational wave (GW) astronomy is a promising new window to study our universe and the properties of DM. LIGO and other interferometer experiments are forecasted to put strong constraints on the fraction of primordial black holes (PBHs) in the universe, down to a mass scale of $\sim 10^{-13}\ M_\odot$ [177–180]. However, the binary black hole (BBH) merger rate $\mathcal{R}_{BBH}^{exp} \sim 9.7$–$101\ \mathrm{Gpc}^{-3}\ \mathrm{y}^{-1}$ detected by LIGO [181] seems to exceed the predictions of $\mathcal{R}_{BBH}^{th} \sim 5.4\ \mathrm{Gpc}^{-3}\ \mathrm{y}^{-1}$ in some theoretical models of star formation [182].

In has been suggested in refs. [183, 184] that this discrepancy could be explained by the early formation of BHs in mirror matter-dominated systems. This idea is supported by the fact that none of the GW signals from BBH mergers detected by LIGO were accompanied by an electromagnetic counterpart, indicating that those systems had accreted very little visible matter. A similar idea can be applied to binary neutron star (NS) mergers and BH-NS coalescence [185], which only led to the detection of one electromagnetic signal [186] out of the many candidate events.

According to [183, 184], since the cosmic star formation rate (SFR) peaked at $z \sim 1.9$ for visible matter, then it should have peaked at a redshift $z' \simeq -1 + (1 + 1.9)/x$ in the MƧ, leaving more time for mirror matter to form BHs and binary systems. According to our present findings, this argument is incorrect, since we have shown that star formation depends primarily on chemical abundances, matter temperature and the gravitational potential, not on the background radiation temperature. At late times ($z \ll z_{\mathrm{dec}}$), visible and mirror particles collapse inside the same local gravitational potential well and they are shock-heated to the same temperature $\sim T_{\mathrm{vir}}$ (recall eq. (4.26)). Hence the mirror SFR differs from that of the SM only because of its high He abundance and how it impacts the cooling rate. These effects are not encoded by a simple $x$-dependent rescaling of $z$.

Nevertheless, the authors of [109, 110] suggested that the inefficient cooling and fragmentation of mirror gas clouds could lead to the early formation of direct collapse black holes (DCBHs). Although they would more likely act as supermassive BH seeds, they could also increase the binary merger rate in the mass range probed by LIGO and the other GW interferometers. In the next decade, as the measurements and predictions for $\mathcal{R}_{BBH}$ are refined, as well as the understanding of BH formation from mirror matter, this could be a useful observable to further constrain such models.

21-cm line surveys are another promising technique for studying late-time cosmology and structure formation. The 21-cm line is a consequence of the hyperfine structure of hydrogen and is emitted when the spin of its electron flips. The intensity of this signal depends on the abundance of neutral hydrogen as well as the temperature at the moment of its emission. The EDGES experiment reported a surprisingly deep absorption feature in the signal emitted at the epoch of reionization [187]. Although it still awaits confirmation, many have tried to relate this anomaly to DM properties [188–193]. Mirror matter could be compatible with the EDGES result if the model is augmented by a large photon-mirror photon kinetic mixing term, $\epsilon \sim 10^{-3}$, and if the CDM is light, $\sim 10\,\mathrm{MeV}$. To explain the EDGES anomaly would also require breaking the mirror symmetry by allowing for a new long-range force between the DM and the CDM, as shown in ref. [192]. (The large kinetic mixing would evade constraints from underground direct detection since millicharged mirror DM would not be able to penetrate the earth.) Ref. [194] proposed an alternative mechanism in which mirror neutrinos decay to visible photons, $\nu_i' \to \gamma\nu_j$, to explain the EDGES anomaly, using a smaller kinetic mixing $\epsilon \lesssim 10^{-6}$. This scenario too would require mirror symmetry breaking, in the form of a small MS photon mass. These two models might require even further breaking of the mirror symmetry in order to avoid stringent limits $\epsilon \lesssim 10^{-9}$–$10^{-7}$ set by $N_{\mathrm{eff}}$ [17, 125] and orthopositronium decay [124] in the unbroken symmetry scenario.

Independently of whether the EDGES anomaly is confirmed, furture 21-cm line surveys can be used to constrain compact DM objects like mirror stars. Should mirror matter compact objects form before visible stars (as in the early formation of DCBHs proposed by [109, 110]), those objects would accrete visible matter and accelerate the reonization of the universe, leaving a characteristic imprint on the 21-cm signal [195] and distorting the CMB spectrum [196]. The suppression of the power spectrum by a dark sector, as we discussed in section 4.2, is also expected to delay structure formation and the absorption feature of the 21-cm line [197].

It was recently suggested that gravitational lensing of fast radio bursts would present a characteristic interference pattern and could probe MACHOs in the mass range $10^{-4}$–$10^{-1}\,M_\odot$ [198]. Although this is smaller than the typical mass scale for mirror stars, it could lead to new constraints on the abundance of smaller objects, like mirror brown dwarfs and mirror planets.

The idea that mirror planets could orbit visible stars (or the opposite) was proposed two decades ago [199, 200], but not explored in detail. A smoking gun signal for small mirror matter structures would be the detection of an exoplanet-like object via Doppler spectroscopy or microlensing without the expected transit, in the case where the inclination angle is 90°. With improved understanding of how mirror planets form and how often they could be captured by a visible stars, the nondiscovery of such events could eventually rule out some of the parameter space of the model.

Finally, mirror stars would heat and potentially dissolve visible wide binary star systems, star clusters and ultra-faint dwarf galaxies via dynamical relaxation. This effect was used to rule out heavy MACHOs ($m_{\rm mac} \gtrsim 5$–$10\,M_\odot$) from making up a significant fraction of DM [201, 202]. Future studies of similar systems could tighten the constraints on MACHOs and, pending a more refined model for mirror star formation, on mirror matter.

# Chapter 6

# Conclusions

Working within the context of unbroken mirror symmetry, this thesis investigated the formation of galactic structures of mirror dark matter in a MW-like halo and constrained the parameters $x = T'/T$, $\beta = \Omega_{b'}/\Omega_b$ of the theory using astrophysical data. We have shown that the temperature hierarchy $x < 1$ required by cosmological observations leads to a He-dominated mirror sector. We also presented a numerical calculation of the mirror recombination evolution and the relic ionization fraction. Our results show that recombination is generally more efficient in the MS, leaving fewer free electrons at late times. Consequently, and because of the low ${H_2}'$ abundance, primordial gas clouds of mirror matter cool more slowly and are less prone to structure formation than ordinary baryons.

Our structure formation simulation showed that over 90 % of mirror baryons remain in an isothermal hot gas cloud if $x \lesssim 0.1$ and $\beta \lesssim 1$. Nevertheless, astronomical observations allowed us to rule out $\beta \gtrsim 1$ for $x \lesssim 0.1$ and $\beta \gtrsim 0.3$ at $x = 0.5$. The most stringent constraints come from observations of the MW disk surface density and bulge mass. Both of these are derived by comparing stellar dynamics (measured *e.g.* by Gaia) with spectroscopy data. One can therefore hope that the release of Gaia EDR3 in 2020 and improved understanding of luminosity data will shed more light on the existence of dark galactic structures.

One may wonder how likely it is to find an embedding of perfect mirror symmetry in a complete model including inflation, such that the relative temperatures in the two sectors differ as we have presumed. Surprisingly, little effort has been devoted to this issue in the past decades. In ref. [19], we proposed an 'out-of-phase' tachyonic reheating mechanism in which the two sectors couple to the inflaton with opposite signs. In principle, this could naturally lead to a temperature difference between visible and mirror matter, but further investigation is required to check if this model is consistent with the constraint $x \lesssim 0.5$.

It is also interesting to contemplate non-minimal scenarios in which mirror symmetry is not exactly conserved at the microscopic level. This of course makes it easier to achieve the asymmetry between temperatures of the two sectors. A simple example is to allow for the mirror Higgs field to have a different VEV, $v' \neq v$, which changes the mirror fermions masses by a factor $v'/v$. In that case, if $v'/v > 1$ and we introduce portal interactions between the two sectors in the early universe, there would be a net transfer of entropy to the less massive SM fermions until the two sectors decouple from each other. Mirror symmetry could also already be broken during reheating, which would affect the decay rate of the inflaton into each sector and lead to different reheating temperatures without portal interactions [126]. By generalizing the chemical and cooling rates described in Appendices A and B for the nonsymmetric MS, our present analysis could be repeated to study structure formation in theses altered scenarios.

Another variation of the model is the inclusion of the Higgs portal interaction $h^2 h'^2$ or kinetic mixing $F^{\mu\nu} F'_{\mu\nu}$ between the MS and the SM. Although significantly constrained by laboratory and astrophysical considerations, they could have important implications for cosmology and structure formation. For instance, mirror photons produced in ordinary supernovae would heat the dark MS disk, leading to its expansion (larger scale height $h_D$) [17] and possibly lifting our current constraint from the MW disk surface density. More importantly, these portal interactions would also open the possibility for direct and indirect detection experiments, providing us with new ways to probe the mirror sector.

# Appendix A

# Recombination parameters

Here we define quantities appearing in the evolution equations (3.48-3.51) that are needed for recombination in the mirror sector [132–140].

The Thomson scattering cross section is $\sigma_T = 6.6524 \times 10^{-25}$ cm$^{-2}$ and $a_R = \pi^2 k^4/15\hbar^3 c^3$ is the radiation constant. The other parameters come from the atomic configuration of both elements. The Ly$\alpha$ frequency is $\nu_\alpha = 2466.0$ THz. The He$^0$ $2s$-$1s$ frequency is $\nu_s =$ 4984.9 THz and $\nu_{ps} = 145.62$ THz is the frequency difference between the $2p$-$1s$ and the $2s$-$1s$ transitions of He$^0$. The two-photon rates are $\Lambda_{\rm H} = 8.22458$ s$^{-1}$ and $\Lambda_{\rm He} = 51.3$ s$^{-1}$.

The two recombination parameters $\alpha_i$ are given by (in m$^3$ s$^{-1}$):

$$\alpha_{\rm H} = \frac{F}{10^{19}} \frac{a t^b}{1 + c t^d}, \tag{A.1}$$

$$\alpha_{\rm He} = q \left[ \sqrt{\frac{T'_M}{T_2}} \left( 1 + \sqrt{\frac{T'_M}{T_2}} \right)^{1-p} \left( 1 + \sqrt{\frac{T'_M}{T_1}} \right)^{1+p} \right]^{-1}, \tag{A.2}$$

where the fit coefficients are $a = 4.309$, $b = -0.6166$, $c = 0.6703$, $d = 0.5300$ and $t = T'_M/10^4$ K. $F$ is a fudge factor set to 1.125 [203]. Furthermore, $q = 10^{-16.744}$, $p = 0.711$, $T_1 = 10^{5.114}$ K and $T_2$ was fixed at 3 K. The principle of detailed balance gives the photoionization coefficients $\beta_i$:

$$\beta_i = g_i \alpha_i \left( \frac{m_e k T'_M}{2\pi\hbar^2} \right)^{3/2} e^{-\chi_i / k T'_M}. \tag{A.3}$$

The statistical weight factor $g_i$ is 1 for H and 4 for He and the ionization energies from the $2s$ level are $\chi_{\rm H} = 3.3996$ eV and $\chi_{\rm He} = 3.9716$ eV.

Finally, the coefficients $K_i$ take into account the cosmological redshift of the H Ly$\alpha$ and He$^0$ $2p$-$11s$ photons that reionize the atoms. They are given by $K_i = \lambda_i^3/(8\pi H(z))$ with $\lambda_\alpha = 121.5682$ nm and $\lambda_{\rm He} = 58.4334$ nm.

# Appendix B

# Cooling and chemical rates

The tables below list the cooling rates of all atomic processes as well as the fitting coefficients for eq. (4.34). We also list every chemical rate that enters the Boltzmann equations (4.36) and that allowed us to find the steady-state abundances of every species.

Table B.1: Cooling rates for atomic processes. $T_K$ is the gas temperature in kelvin and $T_n = T/(10^n \text{ K})$. The densities $n_i$ are in cm$^{-3}$. Adapted from [35, 153].

| Process | Species | $\mathcal{C}_{\text{atom}}$ (erg s$^{-1}$ cm$^{-3}$) |
|---|---|---|
| Collisional excitation | $\mathrm{H}^0$ | $7.5 \times 10^{-19}(1+T_5^{1/2})^{-1}e^{-118348/T_K}n_e n_{\mathrm{H}^0}$ |
| | $\mathrm{He}^+$ | $5.54 \times 10^{-17}T_K^{-0.397}(1+T_5^{1/2})^{-1}e^{-473638/T_K}n_e n_{\mathrm{He}^+}$ |
| | $\mathrm{He}^0$ (triplets) | $9.10 \times 10^{-27}T_K^{-0.1687}(1+T_5^{1/2})^{-1}e^{-13179/T_K}n_e^2 n_{\mathrm{He}^+}$ |
| Collisional ionization | $\mathrm{H}^0$ | $1.27 \times 10^{-21}T_K^{1/2}(1+T_5^{1/2})^{-1}e^{-157809.1/T_K}n_e n_{\mathrm{H}^0}$ |
| | $\mathrm{He}^0$ | $9.38 \times 10^{-22}T_K^{1/2}(1+T_5^{1/2})^{-1}e^{-285335.41/T_K}n_e n_{\mathrm{He}^0}$ |
| | $\mathrm{He}^+$ | $4.95 \times 10^{-22}T_K^{1/2}(1+T_5^{1/2})^{-1}e^{-631515/T_K}n_e n_{\mathrm{He}^+}$ |
| | $\mathrm{He}^0(2^3S)$ | $5.01 \times 10^{-27}T_K^{-0.1687}(1+T_5^{1/2})^{-1}e^{-55338/T_K}n_e^2 n_{\mathrm{He}^+}$ |
| Recombination | $\mathrm{H}^+$ | $8.7 \times 10^{-27}T_K^{1/2}T_3^{-0.2}(1+T_6^{0.7})^{-1}n_e n_{\mathrm{H}^+}$ |
| | $\mathrm{He}^+$ | $1.55 \times 10^{-26}T_K^{0.3647}n_e n_{\mathrm{He}^+}$ |
| | $\mathrm{He}^{++}$ | $3.48 \times 10^{-26}T_K^{1/2}T_3^{-0.2}(1+T_6^{0.7})^{-1}n_e n_{\mathrm{He}^{++}}$ |
| Dielectronic recombination | $\mathrm{He}^+$ | $1.24 \times 10^{-13}T_K^{-1.5}e^{-470000/T_K}(1+0.3e^{-94000/T_K})n_e n_{\mathrm{He}^+}$ |

Table B.2: Fitting coefficients for $H_2$ cooling rates in the low density limit assuming a 3:1 ortho-para ratio. Adapted from [154].

| Species | Temperature range (K) | Coefficients | Species | Temperature range (K) | Coefficients |
|---|---|---|---|---|---|
| $H^0$ | $10 < T \leq 100$ | $a_0 = -16.818342$ | $H^0$ | $100 < T \leq 1000$ | $a_0 = -24.311209$ |
| | | $a_1 = 37.383713$ | | | $a_1 = 3.5692468$ |
| | | $a_2 = 58.145166$ | | | $a_2 = -11.332860$ |
| | | $a_3 = 48.656103$ | | | $a_3 = -27.850082$ |
| | | $a_4 = 20.159831$ | | | $a_4 = -21.328264$ |
| | | $a_5 = 3.8479610$ | | | $a_5 = -4.2519023$ |
| $H^0$ | $1000 < T \leq 6000$ | $a_0 = -24.311209$ | $H_2$ | $100 < T \leq 6000$ | $a_0 = -23.962112$ |
| | | $a_1 = 4.6450521$ | | | $a_1 = 2.09433740$ |
| | | $a_2 = -3.7209846$ | | | $a_2 = -0.77151436$ |
| | | $a_3 = 5.9369081$ | | | $a_3 = 0.43693353$ |
| | | $a_4 = -5.5108047$ | | | $a_4 = -0.14913216$ |
| | | $a_5 = 1.5538288$ | | | $a_5 = -0.033638326$ |
| $He^0$ | $10 < T \leq 6000$ | $a_0 = -23.689237$ | $H^+$ | $10 < T \leq 10000$ | $a_0 = -21.716699$ |
| | | $a_1 = 2.1892372$ | | | $a_1 = 1.3865783$ |
| | | $a_2 = -0.81520438$ | | | $a_2 = -0.37915285$ |
| | | $a_3 = 0.29036281$ | | | $a_3 = 0.11453688$ |
| | | $a_4 = -0.16596184$ | | | $a_4 = -0.23214154$ |
| | | $a_5 = 0.19191375$ | | | $a_5 = 0.058538864$ |
| $e$ | $10 < T \leq 200$ | $a_0 = -34.286155$ | $e$ | $200 < T \leq 10000$ | $a_0 = -22.190316$ |
| | | $a_1 = -48.537163$ | | | $a_1 = 1.5728955$ |
| | | $a_2 = -77.121176$ | | | $a_2 = -0.21335100$ |
| | | $a_3 = -51.352459$ | | | $a_3 = 0.96149759$ |
| | | $a_4 = -15.169160$ | | | $a_4 = -0.91023195$ |
| | | $a_5 = -0.98120322$ | | | $a_5 = 0.13749749$ |

Table B.3: Chemical reaction rates considered in our analysis. $T_K$ and $T_e$ represent the gas temperature in K and eV, respectively, while $T_{\gamma,e}$ is the photon temperature in eV. Table adapted from [142, 154, 204]. Some minor reactions were ignored for simplicity.

| Reaction | Rate coefficient ($cm^3$ $s^{-1}$ or $s^{-1}$) | Temperature range |
|---|---|---|
| 1) $H^0 + e \to H^+ + 2e$ | $k_1$ = exp[-32.71396786+13.5365560 ln $T_e$ | |
| | - 5.73932875 (ln $T_e$)$^2$+1.56315498 (ln $T_e$)$^3$ | |
| | - 0.28770560 (ln $T_e$)$^4$+3.48255977 × $10^{-2}$(ln $T_e$)$^5$ | |
| | - 2.63197617 × $10^{-3}$(ln $T_e$)$^6$+1.11954395 × $10^{-4}$(ln $T_e$)$^7$ | |
| | - 2.03914985 × $10^{-6}$(ln $T_e$)$^8$] | |
| 2) $H^+ + e \to H^0 + \gamma$ | $k_2 = 3.92 \times 10^{-13}\ T_e^{\ -0.6353}$ | $T \leq 5500$ K |
| | $k_2$ = exp[-28.61303380689232 | $T > 5500$ K |
| | - 7.241 125 657 826 851 × $10^{-1}$ ln $T_e$ | |
| | - 2.026 044 731 984 691 × $10^{-2}$ (ln $T_e$)$^2$ | |
| | - 2.380 861 877 349 834 × $10^{-3}$ (ln $T_e$)$^3$ | |
| | - 3.212 605 213 188 796 × $10^{-4}$ (ln $T_e$)$^4$ | |
| | - 1.421 502 914 054 107 × $10^{-5}$ (ln $T_e$)$^5$ | |
| | + 4.989 108 920 299 510 × $10^{-6}$ (ln $T_e$)$^6$ | |
| | + 5.755 614 137 575 750 × $10^{-7}$ (ln $T_e$)$^7$ | |
| | - 1.856 767 039 775 260 × $10^{-8}$ (ln $T_e$)$^8$ | |
| | - 3.071 135 243 196 590 × $10^{-9}$ (ln $T_e$)$^9$] | |
| 3) $He^0 + e \to He^+ + 2e$ | $k_3$ = exp[-44.09864886 | |
| | + 23.915 965 63 ln$T_e$ | |
| | - 10.753 230 2 (ln $T_e$)$^2$ | |
| | + 3.058 038 75 (ln $T_e$)$^3$ | |
| | - 5.685 118 9 × $10^{-1}$ (ln $T_e$)$^4$ | |
| | + 6.795 391 23 × $10^{-2}$ (ln $T_e$)$^5$ | |
| | - 5.009 056 10 × $10^{-3}$ (ln $T_e$)$^6$ | |
| | + 2.067 236 16 × $10^{-4}$ (ln$T_e$)$^7$ | |
| | - 3.649 161 41 × $10^{-6}$ (ln $T_e$)$^8$] | |
| 4) $He^+ + e \to He^0 + \gamma$ | $k_4 = 3.92 \times 10^{-13}\ T_e^{\ -0.6353}$ | $T_e \leq 0.8$ |
| | $k_4 = 3.92 \times 10^{-13}\ T_e^{-0.6353}$ | $T_e > 0.8$ |
| | + 1.54 × $10^{-9}$ $T_e^{-1.5}$ [1.0 + 0.3 / exp(8.099 328 789 667/$T_e$)] | |
| | /[exp(40.496 643 948 336 62/$T_e$)] | |
| 5) $He^+ + e \to He^{++} + 2e$ | $k_5$ = exp[-68.710 409 902 120 01 | |
| | + 43.933 476 326 35 ln$T_e$ | |
| | - 18.480 669 935 68 (ln $T_e$)$^2$ | |
| | + 4.701 626 486 759 002 (ln $T_e$)$^3$ | |
| | - 7.692 466 334 492 × $10^{-1}$ (ln $T_e$)$^4$ | |
| | + 8.113 042 097 303 × $10^{-2}$ (ln $T_e$)$^5$ | |
| | - 5.324 020 628 287 001 × $10^{-3}$ (ln $T_e$)$^6$ | |
| | + 1.975 705 312 221 × $10^{-4}$ (ln $T_e$)$^7$ | |
| | - 3.165581065665 × $10^{-6}$ (ln $T_e$)$^8$] | |
| 6) $He^{++} + e \to He^+ + \gamma$ | $k_6 = 3.36 \times 10^{-10}\ T_K^{-1/2}(T_K/1000)^{-0.2}(1 + (T/10^6)^{0.7})^{-1}$ | |

Table B.3: *(Continued)* Chemical reaction rates considered in our analysis. $T_K$ and $T_e$ represent the gas temperature in K and eV, respectively, while $T_{\gamma,e}$ is the photon temperature in eV. Table adapted from [142, 154, 204]. Some minor reactions were ignored for simplicity.

| Reaction | Rate coefficient ($\mathrm{cm^3\ s^{-1}}$ or $\mathrm{s^{-1}}$) | Temperature range |
|---|---|---|
| 7) $H^0 + e \to H^- + \gamma$ | $k_7 = 3 \times 10^{-16}\ (T_K/300)^{0.95}\ \exp(-T_K/9320)$ | |
| -7) $H^- + \gamma \to H^0 + e$ | $k_{-7} = 4\ k_7\ (m_e T_{\gamma,e}/2\pi\hbar^2)^{3/2} \exp(-0.754/T_{\gamma,e})$ | |
| 8) $H^- + H^0 \to H_2 + e$ | $k_8 = 1.5 \times 10^{-9}\ (T_K/300)^{-0.1}$ | |
| 11) $H_2 + H^+ \to H_2^+ + H^0$ | $k_{11}$ = exp[-24.249 146 877 315 36 | |
| | + 3.400 824 447 095 291 ln $T_e$ | |
| | - 3.898 003 964 650 152 (ln$T_e$)$^2$ | |
| | + 2.045 587 822 403 071 (ln $T_e$)$^3$ | |
| | - 5.416 182 856 220 388 $\times 10^{-1}$ (ln $T_e$)$^4$ | |
| | + 8.410 775 037 634 12 $\times 10^{-2}$ (ln $T_e$)$^5$ | |
| | - 7.879 026 154 483 455 $\times 10^{-3}$ (ln $T_e$)$^6$ | |
| | + 4.138 398 421 504 563 $\times 10^{-4}$ (ln $T_e$)$^7$ | |
| | - 9.363 458 889 286 11 $\times 10^{-6}$ (ln $T_e$)$^8$] | |
| 12) $H_2 + e \to 2H^0 + e$ | $k_{12} = 5.6 \times 10^{-11} T_K^{0.5} \exp(-102124.0/T_K)$ | |
| 13) $H^- + e \to H^0 + 2e$ | $k_{13}$ = exp(-18.018 493 342 73 | |
| | + 2.360 852 208 681 ln $T_e$ | |
| | - 2.827 443 061 704 $\times 10^{-1}$ (ln $T_e$)$^2$ | |
| | + 1.623 316 639 567 $\times 10^{-2}$ (ln $T_e$)$^3$ | |
| | - 3.365 012 031 362 999 $\times 10^{-2}$ (ln $T_e$)$^4$ | |
| | + 1.178 329 782 711 $\times 10^{-2}$ (ln $T_e$)$^5$ | |
| | - 1.656 194 699 504 $\times 10^{-3}$ (ln $T_e$)$^6$ | |
| | + 1.068 275 202 678 $\times 10^{-4}$ (ln $T_e$)$^7$ | |
| | - 2.631 285 809 207 $\times 10^{-6}$ (ln $T_e$)$^8$ | |
| 15) $H^- + H^+ \to 2H^0 + \gamma$ | $k_{15} = 4 \times 10^{-8}\ (T_K/300)^{-0.5}$ | |

# Appendix C

# Finding the NFW concentration

In this appendix we outline the procedure presented in the appendix of ref. [152] to determine the concentration $c$ that parametrizes the NFW density profile (eq. (4.24)) of CDM in a given halo.

Let $M$ be the mass of a given halo at a redshift $z_0$. The authors of ref. [152] defined the collapse redshift $z_{\rm col}$ as the moment at which half the mass of the halo was inside progenitors more massive than $fM$, where $f \approx 0.01$ is a fraction determined by numerical simulations (so that this definition of $z_{\rm col}$ agrees with eqs. (4.5,4.6)). Integrating eq. (4.7) between $M_1 = fM$ at $t_1 = t_{\rm col}$ and $M_2 = M$ at $t_2 = t_0$ gives the fraction of $M$ that was in halos more massive than $fM$ at $z_{\rm col}$ [149], which according to the definition above should be one half:

$$\int_{fM}^{M} f_{12}(M_1, M) dM_1 = \mathrm{erfc}\left( \frac{\delta^0_{\rm col,1} - \delta^0_{\rm col,2}}{\sqrt{2\left(\sigma_1^2 - \sigma_2^2\right)}} \right) \equiv \frac{1}{2}. \tag{C.1}$$

Here erfc$(x)$ is the complementary error function. Recall that $\delta^0_{\rm col}$ and $\sigma^2$ are the values extrapolated to $z = 0$ (which may be different from $z_0$). Expanding this expression in series and using $\delta^0_{{\rm col},i} = \delta_{\rm col}(z_i)/D(z_i)$, where $\delta_{\rm col}(z_i)$ and $D(z_i)$ are given by eqs. (4.5) and (4.4), gives the following relation:

$$\frac{\delta^0_{\mathrm{col},1}}{\delta^0_{\mathrm{col},2}} = \frac{\delta_{\mathrm{col},1}}{\delta_{\mathrm{col},2}} \frac{D(z_0)}{D(z_{\mathrm{col}})} = 1 + \frac{\sqrt{\pi}}{4\,\delta^0_{\mathrm{col},2}} \sqrt{2\,(\sigma_1^2 - \sigma_2^2)}. \tag{C.2}$$

Eq. (C.2) can be solved to obtain $z_{\mathrm{col}}$. In an Einstein-de Sitter universe ($\Omega_{\mathrm{m}} = 1$, $\Lambda = 0$), which is a good approximation at high redshift, the solution is

$$1 + z_{\mathrm{col}} = (1 + z_0)^{-1} + \left( \frac{125}{3888\sqrt{\pi}} \right)^{1/3} \sqrt{2\,(\sigma_1^2 - \sigma_2^2)}. \tag{C.3}$$

If $\Lambda \neq 0$ the solution must be found numerically.

Let $r_s = r_{\mathrm{vir}}/c$ be the characteristic scale of the NFW profile. Eq. (4.24) can be rewritten as:

$$\rho_c(r) = \frac{\delta_c}{(r/r_s)(r/r_s + 1)^2} \left( \frac{\Omega_c}{\Omega_m} \right) \rho_{\mathrm{crit}}, \tag{C.4}$$

where we have introduced the (dimensionless) characteristic overdensity of the halo:

$$\delta_c = \frac{\Delta_{\mathrm{vir}}}{3} \frac{c^3}{\ln(1 + c) - c/(1 + c)}. \tag{C.5}$$

N-body simulations suggested the following relation between $z_{\mathrm{col}}$ and $\delta_c$ [149]:

$$\delta_c(z_0) \simeq C\Omega_m(z_0) \left( \frac{1 + z_{\mathrm{col}}}{1 + z_0} \right)^{1/3}, \tag{C.6}$$

where $C \approx 3 \times 10^3$ is a fit parameter. Combining eqs. (C.5) and (C.6) after obtaining $z_{\mathrm{col}}$ yields a transcendental equation for $c$ that must be solved numerically.

# Bibliography


[1] G. Bertone and D. Hooper, "History of dark matter," *Rev. Mod. Phys.* **90** no. 4, (2018) 045002, `arXiv:1605.04909 [astro-ph.CO]`.

[2] J. C. Kapteyn, "First Attempt at a Theory of the Arrangement and Motion of the Sidereal System," *Astrophys. J.* **55** (1922) 302–328.

[3] J. H. Jeans, "The Motions of Stars in a Kapteyn Universe," *MNRAS* **82** (Jan, 1922) 122–132.

[4] F. Zwicky, "Die Rotverschiebung von extragalaktischen Nebeln," *Helvetica Physica Acta* **6** (Jan, 1933) 110–127. English translation: H. Andernach, "The Redshift of Extragalactic Nebulae," (2017), `arXiv:1711.01693 [astro-ph.IM]`.

[5] F. Zwicky, "On the Masses of Nebulae and of Clusters of Nebulae," *ApJ* **86** (Oct, 1937) 217.

[6] V. C. Rubin and J. Ford, W. Kent, "Rotation of the Andromeda Nebula from a Spectroscopic Survey of Emission Regions," *ApJ* **159** (Feb, 1970) 379.

[7] M. S. Roberts, "A High-Resolution 21-CM Hydrogen-Line Survey of the Andromeda Nebula," *ApJ* **144** (May, 1966) 639.

[8] K. C. Freeman, "On the Disks of Spiral and S0 Galaxies," *ApJ* **160** (Jun, 1970) 811.

[9] V. C. Rubin, J. Ford, W. K., and N. Thonnard, "Rotational properties of 21 SC galaxies with a large range of luminosities and radii, from NGC 4605 (R=4kpc) to UGC 2885 (R=122kpc).," *ApJ* **238** (June, 1980) 471–487.

[10] H. W. Babcock, "The rotation of the Andromeda Nebula," *Lick Observatory Bulletin* **498** (Jan, 1939) 41–51.

[11] P. J. E. Peebles, "Large scale background temperature and mass fluctuations due to scale invariant primeval perturbations," *Astrophys. J.* **263** (1982) L1–L5. [,85(1982)].

[12] A. Del Popolo and M. Le Delliou, "Small scale problems of the ΛCDM model: a short review," *Galaxies* **5** no. 1, (2017) 17, `arXiv:1606.07790 [astro-ph.CO]`.

[13] J. S. Bullock and M. Boylan-Kolchin, "Small-Scale Challenges to the ΛCDM Paradigm," *Ann. Rev. Astron. Astrophys.* **55** (2017) 343–387, `arXiv:1707.04256 [astro-ph.CO]`.

[14] S. Tulin, H.-B. Yu, and K. M. Zurek, "Beyond Collisionless Dark Matter: Particle Physics Dynamics for Dark Matter Halo Structure," *Phys. Rev.* **D87** no. 11, (2013) 115007, `arXiv:1302.3898 [hep-ph]`.

[15] S. Tulin and H.-B. Yu, "Dark Matter Self-interactions and Small Scale Structure," *Phys. Rept.* **730** (2018) 1–57, `arXiv:1705.02358 [hep-ph]`.

[16] Z. Berezhiani, D. Comelli, and F. L. Villante, "The Early mirror universe: Inflation, baryogenesis, nucleosynthesis and dark matter," *Phys. Lett.* **B503** (2001) 362–375, `arXiv:hep-ph/0008105 [hep-ph]`.

[17] R. Foot, "Mirror dark matter: Cosmology, galaxy structure and direct detection," *Int. J. Mod. Phys.* **A29** (2014) 1430013, `arXiv:1401.3965 [astro-ph.CO]`.

[18] P. Ciarcelluti, "Cosmology with mirror dark matter," *Int. J. Mod. Phys.* **D19** (2010) 2151–2230, `arXiv:1102.5530 [astro-ph.CO]`.

[19] J.-S. Roux and J. M. Cline, "Constraining galactic structures of mirror dark matter," `arXiv:2001.11504 [astro-ph.CO]`.

[20] **Particle Data Group** Collaboration, M. Tanabashi *et al.*, "Review of Particle Physics," *Phys. Rev.* **D98** no. 3, (2018) 030001.

[21] B. W. Carroll and D. A. Ostlie, *An Introduction to Modern Astrophysics.* Cambridge University Press, 2017.

[22] F. W. Dyson, A. S. Eddington, and C. Davidson, "A Determination of the Deflection of Light by the Sun's Gravitational Field, from Observations Made at the Total Eclipse of May 29, 1919," *Philosophical Transactions of the Royal Society of London Series A* **220** (Jan., 1920) 291–333.

[23] M. Bartelmann, "Gravitational Lensing," *Class. Quant. Grav.* **27** (2010) 233001, `arXiv:1010.3829 [astro-ph.CO]`.

[24] A. G. Bergmann, V. Petrosian, and R. Lynds, "Gravitational Lens Models of Arcs in Clusters," *ApJ* **350** (Feb., 1990) 23.

[25] M. Markevitch, A. H. Gonzalez, D. Clowe, A. Vikhlinin, L. David, W. Forman, C. Jones, S. Murray, and W. Tucker, "Direct constraints on the dark matter self-interaction cross-section from the merging galaxy cluster 1E0657-56," *Astrophys. J.* **606** (2004) 819–824, `arXiv:astro-ph/0309303 [astro-ph]`.

[26] S. W. Randall, M. Markevitch, D. Clowe, A. H. Gonzalez, and M. Bradac, "Constraints on the Self-Interaction Cross-Section of Dark Matter from Numerical Simulations of the Merging Galaxy Cluster 1E 0657-56," *Astrophys. J.* **679** (2008) 1173–1180, `arXiv:0704.0261 [astro-ph]`.

[27] F. Kahlhoefer, K. Schmidt-Hoberg, M. T. Frandsen, and S. Sarkar, "Colliding clusters and dark matter self-interactions," *Mon. Not. Roy. Astron. Soc.* **437** no. 3, (2014) 2865–2881, `arXiv:1308.3419 [astro-ph.CO]`.

[28] A. Robertson, R. Massey, and V. Eke, "What does the Bullet Cluster tell us about self-interacting dark matter?," *Mon. Not. Roy. Astron. Soc.* **465** no. 1, (2017) 569–587, `arXiv:1605.04307 [astro-ph.CO]`.

[29] C. Lechanoine-LeLuc and F. Lehar, "Nucleon-nucleon elastic scattering and total cross-sections," *Rev. Mod. Phys.* **65** (1993) 47–86.

[30] P. J. E. Peebles, "Primeval adiabatic perturbations - Constraints from the mass distribution," *ApJ* **248** (Sept., 1981) 885–897.

[31] J. Silk and M. L. Wilson, "Large-scale anisotropy of the cosmic microwave background radiation," *ApJ (Letters)* **244** (Mar., 1981) L37–L41.

[32] J. M. Uson and D. T. Wilkinson, "Search for Small-Scale Anisotropy in the Cosmic Microwave Background," *Phys. Rev. Lett.* **49** no. 19, (Nov., 1982) 1463–1465.

[33] G. F. Smoot, C. L. Bennett, A. Kogut, E. L. Wright, J. Aymon, N. W. Boggess, E. S. Cheng, G. de Amici, S. Gulkis, M. G. Hauser, G. Hinshaw, P. D. Jackson, M. Janssen, E. Kaita, T. Kelsall, P. Keegstra, C. Lineweaver, K. Loewenstein, P. Lubin, J. Mather, S. S. Meyer, S. H. Moseley, T. Murdock, L. Rokke, R. F. Silverberg, L. Tenorio, R. Weiss, and D. T. Wilkinson, "Structure in the COBE Differential Microwave Radiometer First-Year Maps," *ApJ (Letters)* **396** (Sept., 1992) L1.

[34] W. Hu and S. Dodelson, "Cosmic Microwave Background Anisotropies," *Ann. Rev. Astron. Astrophys.* **40** (2002) 171–216, `arXiv:astro-ph/0110414`.

[35] H. Mo, F. C. van den Bosch, and S. White, *Galaxy Formation and Evolution*. Cambridge University Press, May, 2010.

[36] E. W. Kolb and M. S. Turner, "The Early Universe," *Front. Phys.* **69** (1990) 1–547.

[37] R. H. Cyburt, "Primordial nucleosynthesis for the new cosmology: Determining uncertainties and examining concordance," *Phys. Rev.* **D70** (2004) 023505, `arXiv:astro-ph/0401091 [astro-ph]`.

[38] D. N. Schramm, *Primordial Nucleosynthesis*, vol. 99 of *Astronomical Society of the Pacific Conference Series*, p. 36. 1996.

[39] H. Reeves, J. Audouze, W. A. Fowler, and D. N. Schramm, "On the Origin of Light Elements," *ApJ* **179** (Feb., 1973) 909–930.

[40] K. Garrett and G. Duda, "Dark Matter: A Primer," *Adv. Astron.* **2011** (2011) 968283, `arXiv:1006.2483 [hep-ph]`.

[41] **Planck** Collaboration, N. Aghanim *et al.*, "Planck 2018 results. VI. Cosmological parameters," `arXiv:1807.06209 [astro-ph.CO]`.

[42] U. Seljak, "A Two fluid approximation for calculating the cosmic microwave background anisotropies," *Astrophys. J.* **435** (1994) L87–L90, arXiv:astro-ph/9406050.

[43] W. Hu and N. Sugiyama, "Anisotropies in the cosmic microwave background: An Analytic approach," *Astrophys. J.* **444** (1995) 489–506, arXiv:astro-ph/9407093.

[44] N. Halverson *et al.*, "DASI first results: A Measurement of the cosmic microwave background angular power spectrum," *Astrophys. J.* **568** (2002) 38–45, arXiv:astro-ph/0104489.

[45] C. L. Bennett, D. Larson, J. L. Weiland, N. Jarosik, G. Hinshaw, N. Odegard, K. M. Smith, R. S. Hill, B. Gold, M. Halpern, E. Komatsu, M. R. Nolta, L. Page, D. N. Spergel, E. Wollack, J. Dunkley, A. Kogut, M. Limon, S. S. Meyer, G. S. Tucker, and E. L. Wright, "Nine-year Wilkinson Microwave Anisotropy Probe (WMAP) Observations: Final Maps and Results," *ApJS* **208** no. 2, (Oct., 2013) 20, arXiv:1212.5225 [astro-ph.CO].

[46] P. J. E. Peebles and J. T. Yu, "Primeval Adiabatic Perturbation in an Expanding Universe," *ApJ* **162** (Dec., 1970) 815.

[47] R. A. Sunyaev and Y. B. Zeldovich, "Small-Scale Fluctuations of Relic Radiation," *Ap&SS* **7** no. 1, (Apr., 1970) 3–19.

[48] D. J. Eisenstein and W. Hu, "Baryonic features in the matter transfer function," *Astrophys. J.* **496** (1998) 605, arXiv:astro-ph/9709112.

[49] J. A. Peacock, "Large scale surveys and cosmic structure," arXiv:astro-ph/0309240 [astro-ph].

[50] J. R. Primack and M. A. K. Gross, "Hot dark matter in cosmology," arXiv:astro-ph/0007165 [astro-ph].

[51] W. J. Percival, B. A. Reid, D. J. Eisenstein, N. A. Bahcall, T. Budavari, J. A. Frieman, M. Fukugita, J. E. Gunn, Ž. Ivezić, G. R. Knapp, R. G. Kron, J. Loveday, R. H. Lupton, T. A. McKay, A. Meiksin, R. C. Nichol, A. C. Pope, D. J. Schlegel, D. P. Schneider, D. N. Spergel, C. Stoughton, M. A. Strauss, A. S. Szalay, M. Tegmark, M. S. Vogeley, D. H. Weinberg, D. G. York, and I. Zehavi, "Baryon acoustic oscillations in the Sloan Digital Sky Survey Data Release 7 galaxy sample," *MNRAS* **401** no. 4, (Feb., 2010) 2148–2168, arXiv:0907.1660 [astro-ph.CO].

[52] **2dFGRS** Collaboration, S. Cole *et al.*, "The 2dF Galaxy Redshift Survey: Power-spectrum analysis of the final dataset and cosmological implications," *Mon. Not. Roy. Astron. Soc.* **362** (2005) 505–534, arXiv:astro-ph/0501174 [astro-ph].

[53] M. Boylan-Kolchin, V. Springel, S. D. M. White, A. Jenkins, and G. Lemson, "Resolving cosmic structure formation with the millennium-ii simulation," *MNRAS* **398** no. 3, (Sep, 2009) 1150–1164. http://dx.doi.org/10.1111/j.1365-2966.2009.15191.x.

[54] R. Reyes, R. Mandelbaum, U. Seljak, T. Baldauf, J. E. Gunn, L. Lombriser, and R. E. Smith, "Confirmation of general relativity on large scales from weak lensing and galaxy velocities," *Nature* **464** (2010) 256–258, `arXiv:1003.2185 [astro-ph.CO]`.

[55] S. Boran, S. Desai, E. O. Kahya, and R. P. Woodard, "GW170817 Falsifies Dark Matter Emulators," *Phys. Rev.* **D97** no. 4, (2018) 041501, `arXiv:1710.06168 [astro-ph.HE]`.

[56] L. Roszkowski, "Light neutralino as dark matter," *Phys. Lett. B* **262** (1991) 59–67.

[57] H. Pagels and J. R. Primack, "Supersymmetry, Cosmology and New TeV Physics," *Phys. Rev. Lett.* **48** (1982) 223.

[58] H.-C. Cheng, J. L. Feng, and K. T. Matchev, "Kaluza-Klein dark matter," *Phys. Rev. Lett.* **89** (2002) 211301, `arXiv:hep-ph/0207125`.

[59] G. Servant and T. M. Tait, "Is the lightest Kaluza-Klein particle a viable dark matter candidate?," *Nucl. Phys. B* **650** (2003) 391–419, `arXiv:hep-ph/0206071`.

[60] J. M. Cline, "TASI Lectures on Early Universe Cosmology: Inflation, Baryogenesis and Dark Matter," *PoS* **TASI2018** (2019) 001, `arXiv:1807.08749 [hep-ph]`.

[61] G. Jungman, M. Kamionkowski, and K. Griest, "Supersymmetric dark matter," *Phys. Rept.* **267** (1996) 195–373, `arXiv:hep-ph/9506380`.

[62] H. Baer and X. Tata, *Dark matter and the LHC*, pp. 179–203. 2009. `arXiv:0805.1905 [hep-ph]`.

[63] R. Bernabei *et al.*, "Dark matter search," *Riv. Nuovo Cim.* **26N1** (2003) 1–73, `arXiv:astro-ph/0307403`.

[64] **DAMA** Collaboration, R. Bernabei *et al.*, "First results from DAMA/LIBRA and the combined results with DAMA/NaI," *Eur. Phys. J. C* **56** (2008) 333–355, `arXiv:0804.2741 [astro-ph]`.

[65] **CoGeNT** Collaboration, C. Aalseth *et al.*, "Search for An Annual Modulation in Three Years of CoGeNT Dark Matter Detector Data," `arXiv:1401.3295 [astro-ph.CO]`.

[66] **CDMS-II** Collaboration, Z. Ahmed *et al.*, "Search for annual modulation in low-energy CDMS-II data," `arXiv:1203.1309 [astro-ph.CO]`.

[67] **CRESST-II** Collaboration, G. Angloher *et al.*, "Results on low mass WIMPs using an upgraded CRESST-II detector," *Eur. Phys. J. C* **74** no. 12, (2014) 3184, `arXiv:1407.3146 [astro-ph.CO]`.

[68] **XENON** Collaboration, J. Angle *et al.*, "First Results from the XENON10 Dark Matter Experiment at the Gran Sasso National Laboratory," *Phys. Rev. Lett.* **100** (2008) 021303, `arXiv:0706.0039 [astro-ph]`.

[69] **LUX** Collaboration, D. Akerib *et al.*, "First results from the LUX dark matter experiment at the Sanford Underground Research Facility," *Phys. Rev. Lett.* **112** (2014) 091303, `arXiv:1310.8214 [astro-ph.CO]`.

[70] S. Blais-Ouellette, P. Amram, and C. Carignan, "Accurate determination of the mass distribution in spiral galaxies. 2. testing the shape of dark halos," *Astron. J.* **121** (2001) 1952, `arXiv:astro-ph/0006449`.

[71] M. Spano, M. Marcelin, P. Amram, C. Carignan, B. Epinat, and O. Hernandez, "GHASP: An H-alpha kinematic survey of spiral and irregular galaxies. 5. Dark matter distribution in 36 nearby spiral galaxies," *Mon. Not. Roy. Astron. Soc.* **383** (2008) 297–316, `arXiv:0710.1345 [astro-ph]`.

[72] A. A. Klypin, A. V. Kravtsov, O. Valenzuela, and F. Prada, "Where are the missing Galactic satellites?," *Astrophys. J.* **522** (1999) 82–92, `arXiv:astro-ph/9901240`.

[73] V. Springel, J. Wang, M. Vogelsberger, A. Ludlow, A. Jenkins, A. Helmi, J. F. Navarro, C. S. Frenk, and S. D. White, "The Aquarius Project: the subhalos of galactic halos," *Mon. Not. Roy. Astron. Soc.* **391** (2008) 1685–1711, `arXiv:0809.0898 [astro-ph]`.

[74] H. Aihara, C. Allende Prieto, D. An, S. F. Anderson, r. Aubourg, E. Balbinot, T. C. Beers, A. A. Berlind, S. J. Bickerton, D. Bizyaev, and et al., "The eighth data release of the sloan digital sky survey: First data from sdss-iii," *The Astrophysical Journal Supplement Series* **193** no. 2, (Mar, 2011) 29. `http://dx.doi.org/10.1088/0067-0049/193/2/29`.

[75] M. J. Rees and J. P. Ostriker, "Cooling, dynamics and fragmentation of massive gas clouds: clues to the masses and radii of galaxies and clusters.," *MNRAS* **179** (June, 1977) 541–559.

[76] G. Efstathiou, "Suppressing the formation of dwarf galaxies via photoionization," *Mon. Not. Roy. Astron. Soc.* **256** (1992) 43P–47P.

[77] S. Garrison-Kimmel, M. Boylan-Kolchin, J. Bullock, and K. Lee, "ELVIS: Exploring the Local Volume in Simulations," *Mon. Not. Roy. Astron. Soc.* **438** no. 3, (2014) 2578–2596, `arXiv:1310.6746 [astro-ph.CO]`.

[78] A. H. Wright, A. S. G. Robotham, S. P. Driver, M. Alpaslan, S. K. Andrews, I. K. Baldry, J. Bland-Hawthorn, S. Brough, M. J. I. Brown, M. Colless, and et al., "Galaxy and mass assembly (gama): the galaxy stellar mass function to z = 0.1 from the r-band selected equatorial regions," *MNRAS* **470** no. 1, (May, 2017) 283–302. `http://dx.doi.org/10.1093/mnras/stx1149`.

[79] M. Boylan-Kolchin, J. S. Bullock, and M. Kaplinghat, "The milky way's bright satellites as an apparent failure of $\lambda$cdm," *MNRAS* **422** no. 2, (Mar, 2012) 1203–1218. `http://dx.doi.org/10.1111/j.1365-2966.2012.20695.x`.

[80] A. Zolotov, A. M. Brooks, B. Willman, F. Governato, A. Pontzen, C. Christensen, A. Dekel, T. Quinn, S. Shen, and J. Wadsley, "Baryons matter: Why luminous satellite galaxies have reduced central masses," *APJ* **761** no. 1, (Nov, 2012) 71. `http://dx.doi.org/10.1088/0004-637X/761/1/71`.

[81] A. M. Brooks and A. Zolotov, "Why Baryons Matter: The Kinematics of Dwarf Spheroidal Satellites," *ApJ* **786** no. 2, (May, 2014) 87, `arXiv:1207.2468 [astro-ph.CO]`.

[82] E. Papastergis and A. A. Ponomareva, "Testing core creation in hydrodynamical simulations using the HI kinematics of field dwarfs," *A&A* **601** (May, 2017) A1, `arXiv:1608.05214 [astro-ph.GA]`.

[83] R. A. Flores and J. R. Primack, "Observational and theoretical constraints on singular dark matter halos," *Astrophys. J.* **427** (1994) L1–4, `arXiv:astro-ph/9402004`.

[84] B. Moore, "Evidence against dissipationless dark matter from observations of galaxy haloes," *Nature* **370** (1994) 629.

[85] P. Kroupa, C. Theis, and C. M. Boily, "The Great disk of Milky Way satellites and cosmological sub-structures," *Astron. Astrophys.* **431** (2005) 517–521, `arXiv:astro-ph/0410421`.

[86] M. Metz, P. Kroupa, and H. Jerjen, "The spatial distribution of the Milky Way and Andromeda satellite galaxies," *Mon. Not. Roy. Astron. Soc.* **374** (2007) 1125–1145, `arXiv:astro-ph/0610933`.

[87] S. S. McGaugh, "The Baryonic Tully-Fisher Relation of Gas-rich Galaxies as a Test of ΛCDM and MOND," *AJ* **143** no. 2, (Feb., 2012) 40, `arXiv:1107.2934 [astro-ph.CO]`.

[88] K. A. Oman *et al.*, "The unexpected diversity of dwarf galaxy rotation curves," *Mon. Not. Roy. Astron. Soc.* **452** no. 4, (2015) 3650–3665, `arXiv:1504.01437 [astro-ph.GA]`.

[89] J. L. Feng, "Dark Matter Candidates from Particle Physics and Methods of Detection," *Ann. Rev. Astron. Astrophys.* **48** (2010) 495–545, `arXiv:1003.0904 [astro-ph.CO]`.

[90] P. Colin, V. Avila-Reese, and O. Valenzuela, "Substructure and halo density profiles in a warm dark matter cosmology," *Astrophys. J.* **542** (2000) 622–630, `arXiv:astro-ph/0004115`.

[91] V. Iršič *et al.*, "New Constraints on the free-streaming of warm dark matter from intermediate and small scale Lyman-$\alpha$ forest data," *Phys. Rev.* **D96** no. 2, (2017) 023522, `arXiv:1702.01764 [astro-ph.CO]`.

[92] R. Peccei and H. R. Quinn, "CP Conservation in the Presence of Instantons," *Phys. Rev. Lett.* **38** (1977) 1440–1443.

[93] R. Peccei and H. R. Quinn, "Constraints Imposed by CP Conservation in the Presence of Instantons," *Phys. Rev. D* **16** (1977) 1791–1797.

[94] H.-Y. Cheng, "The Strong CP Problem Revisited," *Phys. Rept.* **158** (1988) 1.

[95] R. Crewther, P. Di Vecchia, G. Veneziano, and E. Witten, "Chiral Estimate of the Electric Dipole Moment of the Neutron in Quantum Chromodynamics," *Phys. Lett. B* **88** (1979) 123. [Erratum: Phys.Lett.B 91, 487 (1980)].

[96] E. Witten, "Some Properties of O(32) Superstrings," *Phys. Lett. B* **149** (1984) 351–356.

[97] L. D. Duffy and K. van Bibber, "Axions as Dark Matter Particles," *New J. Phys.* **11** (2009) 105008, `arXiv:0904.3346 [hep-ph]`.

[98] W. Hu, R. Barkana, and A. Gruzinov, "Cold and fuzzy dark matter," *Phys. Rev. Lett.* **85** (2000) 1158–1161, `arXiv:astro-ph/0003365`.

[99] D. J. E. Marsh, "Axion Cosmology," *Phys. Rept.* **643** (2016) 1–79, `arXiv:1510.07633 [astro-ph.CO]`.

[100] K.-H. Leong, H.-Y. Schive, U.-H. Zhang, and T. Chiueh, "Testing extreme-axion wave-like dark matter using the BOSS Lyman-alpha forest data," *Mon. Not. Roy. Astron. Soc.* **484** no. 3, (2019) 4273–4286, `arXiv:1810.05930 [astro-ph.CO]`.

[101] K. Schutz, "The Subhalo Mass Function and Ultralight Bosonic Dark Matter," `arXiv:2001.05503 [astro-ph.CO]`.

[102] D. N. Spergel and P. J. Steinhardt, "Observational evidence for selfinteracting cold dark matter," *Phys. Rev. Lett.* **84** (2000) 3760–3763, `arXiv:astro-ph/9909386 [astro-ph]`.

[103] J. Miralda-Escude, "A test of the collisional dark matter hypothesis from cluster lensing," *Astrophys. J.* **564** (2002) 60, `arXiv:astro-ph/0002050 [astro-ph]`.

[104] P. Agrawal, F.-Y. Cyr-Racine, L. Randall, and J. Scholtz, "Make Dark Matter Charged Again," *JCAP* **1705** (2017) 022, `arXiv:1610.04611 [hep-ph]`.

[105] A. H. G. Peter, M. Rocha, J. S. Bullock, and M. Kaplinghat, "Cosmological Simulations with Self-Interacting Dark Matter II: Halo Shapes vs. Observations," *Mon. Not. Roy. Astron. Soc.* **430** (2013) 105, `arXiv:1208.3026 [astro-ph.CO]`.

[106] J. L. Feng, M. Kaplinghat, H. Tu, and H.-B. Yu, "Hidden Charged Dark Matter," *JCAP* **07** (2009) 004, `arXiv:0905.3039 [hep-ph]`.

[107] C. Boehm and R. Schaeffer, "Constraints on dark matter interactions from structure formation: Damping lengths," *Astron. Astrophys.* **438** (2005) 419–442, `arXiv:astro-ph/0410591`.

[108] J. Choquette, J. M. Cline, and J. M. Cornell, "Early formation of supermassive black holes via dark matter self-interactions," *JCAP* **07** (2019) 036, `arXiv:1812.05088 [astro-ph.CO]`.

[109] G. D'Amico, P. Panci, A. Lupi, S. Bovino, and J. Silk, "Massive Black Holes from Dissipative Dark Matter," *Mon. Not. Roy. Astron. Soc.* **473** no. 1, (2018) 328–335, `arXiv:1707.03419 [astro-ph.CO]`.

[110] M. A. Latif, A. Lupi, D. R. G. Schleicher, G. D'Amico, P. Panci, and S. Bovino, "Black hole formation in the context of dissipative dark matter," *Mon. Not. Roy. Astron. Soc.* **485** no. 3, (2019) 3352–3359, `arXiv:1812.03104 [astro-ph.CO]`.

[111] Z. Chacko, H.-S. Goh, and R. Harnik, "The Twin Higgs: Natural electroweak breaking from mirror symmetry," *Phys. Rev. Lett.* **96** (2006) 231802, `arXiv:hep-ph/0506256 [hep-ph]`.

[112] Z. Chacko, D. Curtin, M. Geller, and Y. Tsai, "Cosmological Signatures of a Mirror Twin Higgs," *JHEP* **09** (2018) 163, `arXiv:1803.03263 [hep-ph]`.

[113] L. B. Okun, "Mirror particles and mirror matter: 50 years of speculations and search," *Phys. Usp.* **50** (2007) 380–389, `arXiv:hep-ph/0606202 [hep-ph]`.

[114] K. Nishijima and M. Saffouri, "CP Invariance and the Shadow Universe," *Phys. Rev. Lett.* **14** (1965) 205–207.

[115] R. Foot and Z. K. Silagadze, "Supernova explosions, 511-keV photons, gamma ray bursts and mirror matter," *Int. J. Mod. Phys.* **D14** (2005) 143–152, `arXiv:astro-ph/0404515 [astro-ph]`.

[116] R. Foot and R. Volkas, "Neutrino physics and the mirror world: How exact parity symmetry explains the solar neutrino deficit, the atmospheric neutrino anomaly and the LSND experiment," *Phys. Rev. D* **52** (1995) 6595–6606, `arXiv:hep-ph/9505359`.

[117] R. Foot and S. N. Gninenko, "Can the mirror world explain the ortho-positronium lifetime puzzle?," *Phys. Lett. B* **480** (2000) 171–175, `arXiv:hep-ph/0003278`.

[118] R. Foot and R. Volkas, "Was ordinary matter synthesized from mirror matter? An Attempt to explain why Omega(Baryon) approximately equal to 0.2 Omega(Dark)," *Phys. Rev. D* **68** (2003) 021304, `arXiv:hep-ph/0304261`.

[119] R. Foot, "Implications of the DAMA and CRESST experiments for mirror matter type dark matter," *Phys. Rev. D* **69** (2004) 036001, `arXiv:hep-ph/0308254`.

[120] Z. Berezhiani, "Neutron lifetime puzzle and neutron–mirror neutron oscillation," *Eur. Phys. J.* **C79** no. 6, (2019) 484, `arXiv:1807.07906 [hep-ph]`.

[121] E. W. Kolb, D. Seckel, and M. S. Turner, "The shadow world of superstring theories," *Nature* **314** no. 6010, (Apr, 1985) 415–419.

[122] D. Dunsky, L. J. Hall, and K. Harigaya, "Higgs Parity, Strong CP, and Dark Matter," *JHEP* **07** (2019) 016, `arXiv:1902.07726 [hep-ph]`.

[123] R. Foot, H. Lew, and R. Volkas, "A Model with fundamental improper space-time symmetries," *Phys. Lett. B* **272** (1991) 67–70.

[124] C. Vigo, L. Gerchow, L. Liszkay, A. Rubbia, and P. Crivelli, "First search for invisible decays of orthopositronium confined in a vacuum cavity," *Phys. Rev.* **D97** no. 9, (2018) 092008, `arXiv:1803.05744 [hep-ex]`.

[125] Z. Berezhiani and A. Lepidi, "Cosmological bounds on the 'millicharges' of mirror particles," *Phys. Lett.* **B681** (2009) 276–281, `arXiv:0810.1317 [hep-ph]`.

[126] Z. G. Berezhiani, A. D. Dolgov, and R. N. Mohapatra, "Asymmetric inflationary reheating and the nature of mirror universe," *Phys. Lett.* **B375** (1996) 26–36, `arXiv:hep-ph/9511221 [hep-ph]`.

[127] G. Mangano, G. Miele, S. Pastor, T. Pinto, O. Pisanti, and P. D. Serpico, "Relic neutrino decoupling including flavor oscillations," *Nucl. Phys.* **B729** (2005) 221–234, `arXiv:hep-ph/0506164 [hep-ph]`.

[128] R. H. Cyburt, B. D. Fields, K. A. Olive, and T.-H. Yeh, "Big Bang Nucleosynthesis: 2015," *Rev. Mod. Phys.* **88** (2016) 015004, `arXiv:1505.01076 [astro-ph.CO]`.

[129] M. Hufnagel, K. Schmidt-Hoberg, and S. Wild, "BBN constraints on MeV-scale dark sectors. Part I. Sterile decays," *JCAP* **1802** (2018) 044, `arXiv:1712.03972 [hep-ph]`.

[130] A. Arbey, "AlterBBN: A program for calculating the BBN abundances of the elements in alternative cosmologies," *Comput. Phys. Commun.* **183** (2012) 1822–1831, `arXiv:1106.1363 [astro-ph.CO]`.

[131] A. Arbey, J. Auffinger, K. P. Hickerson, and E. S. Jenssen, "AlterBBN v2: A public code for calculating Big-Bang nucleosynthesis constraints in alternative cosmologies," `arXiv:1806.11095 [astro-ph.CO]`.

[132] P. J. E. Peebles, "Recombination of the Primeval Plasma," *ApJ* **153** (Jul, 1968) 1.

[133] S. Seager, D. D. Sasselov, and D. Scott, "How exactly did the universe become neutral?," *Astrophys. J. Suppl.* **128** (2000) 407–430, `arXiv:astro-ph/9912182 [astro-ph]`.

[134] S. Seager, D. D. Sasselov, and D. Scott, "A new calculation of the recombination epoch," *Astrophys. J.* **523** (1999) L1–L5, `arXiv:astro-ph/9909275 [astro-ph]`.

[135] J. Chluba and R. M. Thomas, "Towards a complete treatment of the cosmological recombination problem," *Mon. Not. Roy. Astron. Soc.* **412** (2011) 748, `arXiv:1010.3631 [astro-ph.CO]`.

[136] J. A. Rubino-Martin, J. Chluba, W. A. Fendt, and B. D. Wandelt, "Estimating the impact of recombination uncertainties on the cosmological parameter constraints from cosmic microwave background experiments," *Mon. Not. Roy. Astron. Soc.* **403** (2010) 439, `arXiv:0910.4383 [astro-ph.CO]`.

[137] J. Chluba, G. M. Vasil, and L. J. Dursi, "Recombinations to the Rydberg States of Hydrogen and Their Effect During the Cosmological Recombination Epoch," *Mon. Not. Roy. Astron. Soc.* **407** (2010) 599, `arXiv:1003.4928 [astro-ph.CO]`.

[138] E. R. Switzer and C. M. Hirata, "Primordial helium recombination. 1. Feedback, line transfer, and continuum opacity," *Phys. Rev.* **D77** (2008) 083006, `arXiv:astro-ph/0702143 [ASTRO-PH]`.

[139] D. Grin and C. M. Hirata, "Cosmological hydrogen recombination: The effect of extremely high-n states," *Phys. Rev. D* **D81** (2010) 083005, `arXiv:0911.1359 [astro-ph.CO]`.

[140] Y. Ali-Haïmoud and C. M. Hirata, "Ultrafast effective multilevel atom method for primordial hydrogen recombination," *Phys. Rev. D* **82** no. 6, (Sep, 2010) 063521, `arXiv:1006.1355 [astro-ph.CO]`.

[141] M. Tegmark, J. Silk, M. J. Rees, A. Blanchard, T. Abel, and F. Palla, "How small were the first cosmological objects?," *Astrophys. J.* **474** (1997) 1–12, `arXiv:astro-ph/9603007`.

[142] C. M. Hirata and N. Padmanabhan, "Cosmological production of H(2) before the formation of the first galaxies," *Mon. Not. Roy. Astron. Soc.* **372** (2006) 1175–1186, `arXiv:astro-ph/0606437 [astro-ph]`.

[143] W. H. Press and P. Schechter, "Formation of galaxies and clusters of galaxies by selfsimilar gravitational condensation," *Astrophys. J.* **187** (1974) 425–438.

[144] J. R. Bond, S. Cole, G. Efstathiou, and N. Kaiser, "Excursion set mass functions for hierarchical Gaussian fluctuations," *Astrophys. J.* **379** (1991) 440.

[145] C. G. Lacey and S. Cole, "Merger rates in hierarchical models of galaxy formation," *Mon. Not. Roy. Astron. Soc.* **262** (1993) 627–649.

[146] P. Ciarcelluti, "Cosmology with mirror dark matter. 1. Linear evolution of perturbations," *Int. J. Mod. Phys. D* **14** (2005) 187–222, `arXiv:astro-ph/0409630`.

[147] S. Cole, C. G. Lacey, C. M. Baugh, and C. S. Frenk, "Hierarchical galaxy formation," *Mon. Not. Roy. Astron. Soc.* **319** (2000) 168, `arXiv:astro-ph/0007281 [astro-ph]`.

[148] A. Ghalsasi and M. McQuinn, "Exploring the astrophysics of dark atoms," *Phys. Rev.* **D97** no. 12, (2018) 123018, `arXiv:1712.04779 [astro-ph.GA]`.

[149] C. Lacey and S. Cole, "Merger rates in hierarchical models of galaxy formation," *MNRAS* **262** no. 3, (June, 1993) 627–649.

[150] B. Diemer, "COLOSSUS: A python toolkit for cosmology, large-scale structure, and dark matter halos," *Astrophys. J. Suppl.* **239** no. 2, (2018) 35, `arXiv:1712.04512 [astro-ph.CO]`.

[151] F.-Y. Cyr-Racine, R. de Putter, A. Raccanelli, and K. Sigurdson, "Constraints on Large-Scale Dark Acoustic Oscillations from Cosmology," *Phys. Rev.* **D89** no. 6, (2014) 063517, `arXiv:1310.3278 [astro-ph.CO]`.

[152] J. F. Navarro, C. S. Frenk, and S. D. M. White, "A Universal density profile from hierarchical clustering," *Astrophys. J.* **490** (1997) 493–508, `arXiv:astro-ph/9611107 [astro-ph]`.

[153] R. Cen, "A Hydrodynamic approach to cosmology - Methodology," *Astrophys. J. Suppl.* **78** (1992) 341–364.

[154] T. Grassi, S. Bovino, D. R. G. Schleicher, J. Prieto, D. Seifried, E. Simoncini, and F. A. Gianturco, "KROME – a package to embed chemistry in astrophysical simulations," *Mon. Not. Roy. Astron. Soc.* **439** no. 3, (2014) 2386–2419, `arXiv:1311.1070 [astro-ph.GA]`.

[155] D. Hollenback and C. F. McKee, "Molecule formation and infrared emission in fast interstellar shocks. I. Physical processes.," *Astrophys. J. Suppl.* **41** (1979) 555–592.

[156] S. C. O. Glover and T. Abel, "Uncertainties in H2 and HD Chemistry and Cooling and their Role in Early Structure Formation," *Mon. Not. Roy. Astron. Soc.* **388** (2008) 1627, `arXiv:0803.1768 [astro-ph]`.

[157] Z. Berezhiani, S. Cassisi, P. Ciarcelluti, and A. Pietrinferni, "Evolutionary and structural properties of mirror star MACHOs," *Astropart. Phys.* **24** (2006) 495–510, `arXiv:astro-ph/0507153 [astro-ph]`.

[158] S. Hocuk and M. Spaans, "The thermodynamics of molecular cloud fragmentation. Star formation under non-Milky Way conditions," *A&A* **510** (Feb., 2010) A110, `arXiv:0911.5122 [astro-ph.SR]`.

[159] E. E. Salpeter, "The Luminosity Function and Stellar Evolution.," *ApJ* **121** (Jan, 1955) 161.

[160] J. Buch, S. C. J. Leung, and J. Fan, "Using Gaia DR2 to Constrain Local Dark Matter Density and Thin Dark Disk," *JCAP* **1904** (2019) 026, `arXiv:1808.05603 [astro-ph.GA]`.

[161] L. Randall and M. Reece, "Dark matter as a trigger for periodic comet impacts," arXiv:1403.0576 [astro-ph.GA].

[162] K. Schutz, T. Lin, B. R. Safdi, and C.-L. Wu, "Constraining a thin dark matter disk with gaia," arXiv:1711.03103 [astro-ph.GA].

[163] M. Cautun, A. Benitez-Llambay, A. J. Deason, C. S. Frenk, A. Fattahi, F. A. Gómez, R. J. J. Grand, K. A. Oman, J. F. Navarro, and C. M. Simpson, "The milky way total mass profile as inferred from gaia dr2," arXiv:1911.04557 [astro-ph.GA].

[164] P. S. Behroozi, C. Conroy, and R. H. Wechsler, "A comprehensive analysis of uncertainties affecting the stellar mass - halo mass relation for 0¡z¡4," arXiv:1001.0015 [astro-ph.CO].

[165] Y. Sofue, "Rotation curve and mass distribution in the galactic center — from black hole to entire galaxy —," arXiv:1307.8241 [astro-ph.GA].

[166] M. Portail, C. Wegg, O. Gerhard, and I. Martinez-Valpuesta, "Made-to-measure models of the galactic box/peanut bulge: stellar and total mass in the bulge region," arXiv:1502.00633 [astro-ph.GA].

[167] M. Zoccali, E. Valenti, and O. A. Gonzalez, "Weighing the two stellar components of the galactic bulge," arXiv:1807.06377 [astro-ph.GA].

[168] **MACHO** Collaboration, C. Alcock *et al.*, "The MACHO project: Microlensing results from 5.7 years of LMC observations," *Astrophys. J.* **542** (2000) 281–307, arXiv:astro-ph/0001272 [astro-ph].

[169] D. P. Bennett, "Large Magellanic Cloud microlensing optical depth with imperfect event selection," *Astrophys. J.* **633** (2005) 906–913, arXiv:astro-ph/0502354 [astro-ph].

[170] **Macho** Collaboration, R. A. Allsman *et al.*, "MACHO project limits on black hole dark matter in the 1-30 solar mass range," *Astrophys. J.* **550** (2001) L169, arXiv:astro-ph/0011506 [astro-ph].

[171] L. Wyrzykowski, S. Kozlowski, J. Skowron, A. Udalski, M. K. Szymanski, M. Kubiak, G. Pietrzynski, I. Soszynski, O. Szewczyk, K. Ulaczyk, and R. Poleski, "The ogle view of microlensing towards the magellanic clouds. iii. ruling out sub-solar machos with the ogle-iii lmc data," arXiv:1012.1154 [astro-ph.GA].

[172] L. Wyrzykowski, S. Kozlowski, J. Skowron, V. Belokurov, M. C. Smith, A. Udalski, M. K. Szymanski, M. Kubiak, G. Pietrzynski, I. Soszynski, O. Szewczyk, and K. Zebrun, "The ogle view of microlensing towards the magellanic clouds. i. a trickle of events in the ogle-ii lmc data," arXiv:0905.2044 [astro-ph.GA].

[173] **EROS-2** Collaboration, P. Tisserand *et al.*, "Limits on the Macho Content of the Galactic Halo from the EROS-2 Survey of the Magellanic Clouds," *Astron. Astrophys.* **469** (2007) 387–404, arXiv:astro-ph/0607207 [astro-ph].

[174] C. Renault, C. Afonso, E. Aubourg, P. Bareyre, F. Bauer, S. Brehin, C. Coutures, C. Gaucherel, J. F. Glicenstein, B. Goldman, M. Gros, D. Hardin, J. de Kat, M. Lachieze-Rey, B. Laurent, E. Lesquoy, C. Magneville, A. Milsztajn, L. Moscoso, N. Palanque-Delabrouille, F. Queinnec, J. Rich, M. Spiro, L. Vigroux, S. Zylberajch, R. Ansari, F. Cavalier, F. Couchot, B. Mansoux, M. Moniez, O. Perdereau, J. P. Beaulieu, R. Ferlet, P. Grison, A. Vidal-Madjar, J. Guibert, O. Moreau, E. Maurice, L. Prevot, C. Gry, S. Char, and J. Fernandez, "Observational limits on MACHOS in the Galactic Halo.," *A&A* **324** (Aug, 1997) L69–L72.

[175] **MEGA** Collaboration, J. T. A. de Jong *et al.*, "Machos in M31? Absence of evidence but not evidence of absence," *Astron. Astrophys.* **446** (2006) 855–875, `arXiv:astro-ph/0507286 [astro-ph]`.

[176] **POINT-AGAPE** Collaboration, S. Calchi Novati *et al.*, "POINT-AGAPE pixel lensing survey of M31: Evidence for a MACHO contribution to galactic halos," *Astron. Astrophys.* **443** (2005) 911, `arXiv:astro-ph/0504188 [astro-ph]`.

[177] R. Saito and J. Yokoyama, "Gravitational wave background as a probe of the primordial black hole abundance," *Phys. Rev. Lett.* **102** (2009) 161101, `arXiv:0812.4339 [astro-ph]`. [Erratum: Phys. Rev. Lett.107,069901(2011)].

[178] R. Saito and J. Yokoyama, "Gravitational-wave constraints on the abundance of primordial black holes," 2009.

[179] B. J. Carr, K. Kohri, Y. Sendouda, and J. Yokoyama, "New cosmological constraints on primordial black holes," *Phys. Rev.* **D81** (2010) 104019, `arXiv:0912.5297 [astro-ph.CO]`.

[180] B. Carr, F. Kuhnel, and M. Sandstad, "Primordial Black Holes as Dark Matter," *Phys. Rev.* **D94** no. 8, (2016) 083504, `arXiv:1607.06077 [astro-ph.CO]`.

[181] **LIGO Scientific, Virgo** Collaboration, B. P. Abbott *et al.*, "GWTC-1: A Gravitational-Wave Transient Catalog of Compact Binary Mergers Observed by LIGO and Virgo during the First and Second Observing Runs," *Phys. Rev.* **X9** no. 3, (2019) 031040, `arXiv:1811.12907 [astro-ph.HE]`.

[182] A. Askar, M. Szkudlarek, D. Gondek-Rosińska, M. Giersz, and T. Bulik, "MOCCA-SURVEY Database – I. Coalescing binary black holes originating from globular clusters," *Mon. Not. Roy. Astron. Soc.* **464** no. 1, (2017) L36–L40, `arXiv:1608.02520 [astro-ph.HE]`.

[183] R. Beradze and M. Gogberashvili, "LIGO Signals from the Mirror World," *Mon. Not. Roy. Astron. Soc.* **487** no. 1, (2019) 650–652, `arXiv:1902.05425 [gr-qc]`.

[184] R. Beradze and M. Gogberashvili, "Gravitational Waves from Mirror World," *MDPI Physics* **1** no. 1, (2019) 67–75, `arXiv:1905.02787 [gr-qc]`.

[185] R. Beradze, M. Gogberashvili, and A. S. Sakharov, "Binary Neutron Star Mergers with Missing Electromagnetic Counterparts as Manifestations of Mirror World," `arXiv:1910.04567 [astro-ph.HE]`.

[186] P. S. Cowperthwaite *et al.*, "The Electromagnetic Counterpart of the Binary Neutron Star Merger LIGO/Virgo GW170817. II. UV, Optical, and Near-infrared Light Curves and Comparison to Kilonova Models," *Astrophys. J.* **848** no. 2, (2017) L17, `arXiv:1710.05840 [astro-ph.HE]`.

[187] J. D. Bowman, A. E. E. Rogers, R. A. Monsalve, T. J. Mozdzen, and N. Mahesh, "An absorption profile centred at 78 megahertz in the sky-averaged spectrum," *Nature* **555** no. 7694, (2018) 67–70, `arXiv:1810.05912 [astro-ph.CO]`.

[188] J. B. Muñoz and A. Loeb, "A small amount of mini-charged dark matter could cool the baryons in the early Universe," *Nature* **557** no. 7707, (2018) 684, `arXiv:1802.10094 [astro-ph.CO]`.

[189] A. Fialkov, R. Barkana, and A. Cohen, "Constraining Baryon–Dark Matter Scattering with the Cosmic Dawn 21-cm Signal," *Phys. Rev. Lett.* **121** (2018) 011101, `arXiv:1802.10577 [astro-ph.CO]`.

[190] A. Berlin, D. Hooper, G. Krnjaic, and S. D. McDermott, "Severely Constraining Dark Matter Interpretations of the 21-cm Anomaly," *Phys. Rev. Lett.* **121** no. 1, (2018) 011102, `arXiv:1803.02804 [hep-ph]`.

[191] R. Barkana, N. J. Outmezguine, D. Redigolo, and T. Volansky, "Strong constraints on light dark matter interpretation of the EDGES signal," *Phys. Rev.* **D98** no. 10, (2018) 103005, `arXiv:1803.03091 [hep-ph]`.

[192] H. Liu, N. J. Outmezguine, D. Redigolo, and T. Volansky, "Reviving Millicharged Dark Matter for 21-cm Cosmology," *Phys. Rev.* **D100** no. 12, (2019) 123011, `arXiv:1908.06986 [hep-ph]`.

[193] P. Panci, "21-cm line Anomaly: A brief Status," in *33rd Rencontres de Physique de La Vallée d'Aoste (LaThuile 2019) La Thuile, Aosta, Italy, March 10-16, 2019*. 2019. `arXiv:1907.13384 [astro-ph.CO]`.

[194] D. Aristizabal Sierra and C. S. Fong, "The EDGES signal: An imprint from the mirror world?," *Phys. Lett.* **B784** (2018) 130–136, `arXiv:1805.02685 [hep-ph]`.

[195] O. Mena, S. Palomares-Ruiz, P. Villanueva-Domingo, and S. J. Witte, "Constraining the primordial black hole abundance with 21-cm cosmology," *Phys. Rev.* **D100** no. 4, (2019) 043540, `arXiv:1906.07735 [astro-ph.CO]`.

[196] M. Ricotti, J. P. Ostriker, and K. J. Mack, "Effect of Primordial Black Holes on the Cosmic Microwave Background and Cosmological Parameter Estimates," *Astrophys. J.* **680** (2008) 829, `arXiv:0709.0524 [astro-ph]`.

[197] L. Lopez-Honorez, O. Mena, and P. Villanueva-Domingo, "Dark matter microphysics and 21 cm observations," *Phys. Rev.* **D99** no. 2, (2019) 023522, `arXiv:1811.02716 [astro-ph.CO]`.

[198] A. Katz, J. Kopp, S. Sibiryakov, and W. Xue, "Looking for MACHOs in the Spectra of Fast Radio Bursts," `arXiv:1912.07620 [astro-ph.CO]`.

[199] R. Foot, "Have mirror planets been observed?," *Phys. Lett.* **B471** (1999) 191–194, `arXiv:astro-ph/9908276 [astro-ph]`.

[200] R. Foot, A. Yu. Ignatiev, and R. R. Volkas, "Do 'isolated' planetary mass objects orbit invisible stellar mass companions?," *Astropart. Phys.* **17** (2002) 195–198, `arXiv:astro-ph/0010502 [astro-ph]`.

[201] T. D. Brandt, "Constraints on MACHO Dark Matter from Compact Stellar Systems in Ultra-Faint Dwarf Galaxies," *Astrophys. J.* **824** no. 2, (2016) L31, `arXiv:1605.03665 [astro-ph.GA]`.

[202] D. P. Quinn, M. I. Wilkinson, M. J. Irwin, J. Marshall, A. Koch, and V. Belokurov, *Dark Matter Constraints from Wide Halo Binary Stars*, vol. 435, p. 453. Astronomical Society of the Pacific Conference Series, 2010.

[203] G. Giesen, J. Lesgourgues, B. Audren, and Y. Ali-Haimoud, "CMB photons shedding light on dark matter," *JCAP* **1212** (2012) 008, `arXiv:1209.0247 [astro-ph.CO]`.

[204] T. Abel, P. Anninos, Y. Zhang, and M. L. Norman, "Modeling primordial gas in numerical cosmology," *New Astron.* **2** (1997) 181–207, `arXiv:astro-ph/9608040 [astro-ph]`.